Universidade de Aveiro Departamento de Biologia
2008

LUÍS DANIEL CERQUEIRA MALHEIRO DO VALE

ESTUDO HIDRODINÂMICO DO PORTO DE VIANA DO CASTELO

Universidade de Aveiro Departamento de Biologia
2008

LUÍS DANIEL CERQUEIRA MALHEIRO DO VALE

ESTUDO HIDRODINÂMICO DO PORTO DE VIANA DO CASTELO

Dissertação apresentada à Universidade de Aveiro para cumprimento dos requisitos necessários à obtenção do grau de Mestre em Ciências das Zonas Costeiras, realizada sob a orientação científica do Dr. João Miguel Dias, Professor Auxiliar do Departamento de Física da Universidade de Aveiro

o júri

presidente

Prof. Doutora Filomena Maria Cardoso Pedrosa Ferreira Martins
professora associada do Departamento de Ambiente e Ordenamento da Universidade de Aveiro

Prof. Doutor João Miguel Sequeira Silva Dias
professor auxiliar do Departamento de Física da Universidade de Aveiro

Doutor Nuno Alexandre Firmino Vaz
investigador pós-doutoramento Secção Ambiente e Energia do Instituto Superior Técnico

agradecimentos

Agradeço ao Professor João Miguel Dias pela orientação científica, permanente disponibilidade e ensinamentos, aos meus colegas António Fernandes, Luís Correia e José Alves pelo apoio e à minha mulher e filho, pela paciência e compreensão.

palavras-chave hidrodinâmica, análise harmónica, modelização numérica, estuário, Viana do Castelo,

resumo Foi efectuado um estudo hidrodinâmico do estuário do Lima, na zona portuária. Após uma caracterização meteorológica da área de estudo foi realizada uma análise à ocorrência de um *storm surge*.
O estuário foi caracterizado quanto ao regime de descarga do rio Lima, à estrutura vertical de salinidade e às correntes de maré.
Foi feita análise harmónica da maré e sua caracterização.
O modelo numérico SIMSYS2D foi implementado, calibrado e validado para o estuário do Lima. O modelo foi utilizado para análise da propagação da maré para montante, caracterização da estrutura horizontal das correntes, quantificação e comparação de correntes em estações diferentes, comportamento hidrodinâmico sob diferentes caudais do rio, alterações à hidrodinâmica portuária introduzidas por dragagens e zonas de expansão, cálculo do prisma de maré e transporte Lagrangeano de partículas.

keywords

hidrodynamics, harmonic analysis, numerical modeling, estuary, Viana do Castelo.

abstract

A hydrodynamic study was carried out on the Lima estuary, namely the commercial port area.
After a meteorological assessment of the study area a storm surge event was analyzed.
The estuary was characterized for the Lima river flow, the vertical salinity structure and for the tidal currents.
A harmonic analysis and characterization of the tide was accomplished.
The numerical model SIMSYS2D was successfully implemented, calibrated and validated for the Lima estuary. The model was used to study the tidal propagation upstream, characterization of the horizontal structure of the currents, quantification and comparison of currents for different stations, hydrodynamic behaviour under different river flows, changes introduced to the hydrodynamics due to port expansion and dredging works, tidal prism calculation and Lagrangian transport of particles.

Contents

List of Figures

List of Tables

1. Introduction

1.1. Motivation, Aims and Structure of the Work

A methodical knowledge of the structure of tidal heights and tidal streams is fundamental towards the understanding of issues like dispersion, pollutant transport, sedimentation processes and water quality in coastal zones.

The effects of harbour engineering works on an estuary are diverse and range from the quality of the water, sedimentation processes, dredged materials management, soil contamination, changes to ecological systems, modifying of hydrodynamics and even to socio-economic aspects.

The project or reconstruction of harbours require an analysis of the flow conditions of different layout alternatives in order to minimize impacts to navigation [Giszas, 1984] due to changes in port hydrodynamics. However, on the vast majority of the cases, port expansion is carried out according to existing morphology, with limited available alternatives.

The port of Viana do Castelo is characterized, on its navigation operational part, by limitations imposed by tidal heights for adequate under keel clearance regarding the largest ships that call the port as well as limitations on the available bollard pull of the tugboats assisting the berthing during maximum tidal stream at spring tides.

Usually, these larger ships, which are the most important commercially for the port, are manoeuvred at high water (slack tide) due to their draft and also to take advantage of weaker or null currents. This limitation to a narrow tidal window induces obvious disadvantages to the operators and also for the port.

While the issue of the under keel clearance is easily solved by a knowledge of the height of the tide at any moment taken from the tide tables as well as the existing bathymetry and ship’s draft (and also other hydrodynamic factors inherent to ship’s movement through the water like squat, pitching, heaving, rolling, and others out of the scope of this work), the values of the currents produced by tidal streams until now could only be estimated, deducing by local observations and experience.

Nevertheless, these currents are responsible for the employment of more tugboats or additional total bollard pull, required due to increased safety margins resulting from lacking knowledge of their correct values.

The detailed understanding of port hydrodynamics allows the widening of the tidal windows and, from the navigation point of view, the overall enhancement of maritime safety.

The undergoing port expansion plan represents a challenge to inner navigation because the projected new berths develop perpendicularly to the river alignment, with obvious manoeuvring difficulties.

On the other hand, changes to bathymetry introduced by the dredging works along the new quays and new manoeuvring basins will most certainly establish changes to local hydrodynamics, an important aspect to follow.

Thus, the implementation of a numerical model that describes the system becomes an extreme valuable tool for the study of processes occurring in these complex environments, as well as the anthropogenic adjustments introduced, allowing the forecast of the physical parameters of the system.

This kind of issues can be solved through the use of an accurate and reliable numerical model, able to reproduce transport and

mixing processes occurring as a reaction to different forcing conditions in its boundaries and to anthropogenic interventions [Dias, 2001].

Despite its economical importance, due to the presence of major industrial facilities (wind generator plant and shipyard) as well as commercial port, there are just a few comprehensive works relating to the Lima estuary. These are mainly studies regarding biological, chemical and environmental research.

An earlier in-depth comprehensive study of the Lima estuary, namely the harbour area, was performed back in the 60's decade by LNEC (National Laboratory of Civil Engineering) [1969] with the aim of building a physical model to study the configuration of the new commercial port. Hardly any data from this study can be used given that the port layout at the mouth of the estuary has since then dramatically changed, with the building of new important infrastructures such as berths and breakwaters and the alteration of the river course on its lower reaches.

More recent studies are within the environmental field, namely regarding the 'Coral Bulker' fuel oil spill after grounding at the port entrance and the spatial and temporal biomarker responses in *Mytilus galloprovincialis* [Moreira *et al.*, 2004], the spatial subtidal macrobenthic distribution in relation to abiotic conditions in the Lima estuary [Sousa *et al.*, 2005], the temporal and spatial distributions of larval fish assemblages in the Lima estuary [Ramos *et al.*, 2006].

The mathematical modelling of salt water intrusion in the Lima estuary [Pinho and Vieira, 2007], was performed based on a two-dimensional hydrodynamic and mass transport model. The hydrodynamic model was implemented using the RMA2 software that is based on the finite element method. The mass transport model, RMA4 was applied to simulate depth-average advection-diffusion processes in aquatic environments.

Another use of hydrodynamic numerical modelling applied to the Lima estuary was the study on the definition of the downstream limits of the Portuguese estuaries. This work was carried out by Maretec (Marine and Environmental Technology Research Center)/Instituto Superior Técnico for INAG, Instituto Nacional da Água. The model used was the Mohid 2000 [www.mohid.com] water modelling system, both the hydrodynamic and Lagrangian transport modules.

Two-dimensional models have been in use for more than 30 years, with inherent developments based on a wide range of successful applications. Typically, two-dimensional depth-integrated models represent lateral and longitudinal variations in velocity and constituents concentration for estuaries with non-uniform cross-sections, branching channels and embayments.

This kind of models is based on the assumption of the vertical homogeneity of the water column, thus enabling the introduction of important simplifications in the equations describing the dynamics of the coastal environments and a reduction of the number of the needed equations.

Since a perfect vertically homogeneous environment seldom exists in estuaries, three-dimensional models do represent better the transport associated with baroclinic flows. However, these models are much more complex and unnecessary to solve most of the problems concerning estuarine zones, as long as the water depths, though varying, are shallow compared with their horizontal dimensions. In fact, although there is a natural trend to an evolution towards three-dimensional flow field simulations, these are still within the domain of more specialist applications such as secondary flows. In some instances, these secondary currents may be appreciable and affect such things as salinity intrusion, sediment transport, thermal distribution and water quality. This is why the choice of the adequate type of model to the required application is of paramount importance on the final results.

By comparison, two-dimensional models are now in full maturity stage allowing for its widespread use on a variety of applications, such as the study of the reduction of harbour sedimentation (2D RMAE Model) [Zimmermann *et al.*, 2000], morphodynamic studies (MIKE 21 Model) [Lehfeldt *et al.*, 2002], the study of coastal flooding (GCOM 2D) [McInnes *et al.,* 2002] and the overall study of the hydrodynamics of several estuarine systems.

In this work, a two-dimensional vertically integrated hydrodynamic model developed from the SIMSYS2D model [Leendertse and Gritton, 1971; Leendertse, 1987; Dias, 2001] is applied. This model has been successfully implemented for the study of Ria de Aveiro hydrodynamics [Sousa and Dias, 2007], has been coupled with salt and heat transport models [Dias and Lopes, 2006], used to study suspended particulate matter and residence time [Dias *et al.*, 2007], has been coupled to a particle tracking model [Dias *et al.*, 2001], used to study transport and dispersal of marine toxic microalgae [Cerejo and Dias, 2007] and also effectively employed for the study of the tidal characteristics of Maputo Bay, Mozambique [Canhanga and Dias, 2005] and on the modelling of fish eggs dispersion at the Patos Lagoon, Brazil [Martins *et al.*, 2007].

It is now quite clear that numerical modelling provides results more detailed than with analytical methods, and can be even more precise. As soon as the model is implemented and calibrated, it becomes relatively easy to obtain results for different conditions.

Thus, for the present work, before the use of the model, several tasks were accomplished. A comprehensive study of the estuary was performed with assistance of existing literature. A thorough meteorological characterization of the study area as well as the Lima river discharge regime was the next step. Limited but consistent field data was collected *in situ*, namely sea surface elevation, temperature and salinity at diverse locations within

the study area. These data assisted on the characterization of the tidal regime as well as the vertical structure of the estuary. Data obtained from moored currentmeters was also processed in order to study the estuary currents. A comprehensive tidal analysis was performed. After being successfully calibrated and validated, the model was used for diverse purposes such as tidal propagation studies, hydrodynamics overall characterization, comparison and quantification of currents and river flow regimes for different stations, study of the changes introduced to the hydrodynamics by port expansion and dredging works, establishing of the river flow/tidal prism ratio and also the coupling of a Lagrangian model that enabled the study of the tracking of particles released and emitted at several stations.

Prior to the initiation of this work, the defined aims were fundamentally the study of tidal propagation, characterization of the horizontal structure of tidal streams, study of a storm surge occurrence, implementation of the numerical model, use of the model to study the changes introduced by the port expansion works and the coupling of a Lagrangian model to study the paths of released particles.

1.2. Study Area

Fig. 1. Study area location (Portugal)

Fig. 2. Study area location (Europe)

The port of Viana do Castelo is located on the Northwest coast of Portugal (41º40.5'N 008º50.3'W) lying on the mouth of the Lima River, at about 12 miles South from Minho River and 33 miles North of Leixões port (Fig. 1 and Fig. 2).

Fig. 3. Lima Estuary

It is a small port under international standards, although representing one of the most important infrastructures at a regional level.

The main harbour facilities are located at the left margin (South) of the river and are capable of receiving ships up to 180 meters length overall and 8.0 meters draft. These berths are accessed

through a navigable channel with depths maintained through regular dredging works (Fig. 3).

There is also an important medium size shipyard which has designed, built, converted and repaired different sophisticated and specialised ships throughout the years. This shipyard, which is presently the major Portuguese shipbuilder, is located on an inner basin at the Northeast sector of the harbour, protected by two small breakwaters (“Esporão do Bugio” to the West and “Esporão dos Pilotos” to the East), limiting this area to a 115 meter opening which links the basin to the river.

The old port docks, the future oceanic marina, are accessed via a 14 meter wide channel which used to have two locks that enabled larger ships inside to remain afloat even in low water.

The port waters are protected by two main breakwaters, the outer one developing on a 170º bearing and with 2170 meters (“Molhe Exterior”), and the inner one with about 700 meters on a South/southwesterly orientation (“Molhe do Cabedelo”). These two heavy constructions provide shelter to the berthed vessels under most weather conditions. The estuary is thus connected with the ocean by a 650 meter wide opening (distance between the two breakwaters).

The study area comprises the commercial harbour waters downstream of Eiffel Bridge and also the part of the river upstream until the New Bridge. Although not navigable to ships due to airdraft restrictions imposed by the Eiffel Bridge this upstream branch of the river is formed by a main channel with a medium depth of 4.0 m, several mudflats and salt marshes. There are two secondary channels running North and South of the saltmarshes, although much shallower than the main one.

From the port entrance to the Eiffel Bridge the distance is about 2850 meters, approximately the same in between bridges. The river

width ranges between about 240 meters on the main navigable channel, increasing on the manoeuvring basin up to 500 meters and then varying between 110 and 230 meters wide upstream of Eiffel Bridge.

The study area comprises about 4000 km^2 of wet estuary. The part of the estuary under study has a medium depth of about 5.0 meters and maximum depth of 8.0 meters (inside breakwaters). It is a semidiurnal mesotidal estuary with a tidal range of about 2.5 m for the medium average tide and maximum and minimum tidal ranges of 3.7 m and 1.1 m, respectively. The river discharge regime is highly variable throughout the year and also dependent on the two energy producing dams located upstream. River flow can vary between 4 m^3s^{-1} and more than 200 m^3s^{-1}, with average values of 50 m^3s^{-1}. This freshwater input to the estuary affects its salinity vertical structure and, although considered a partially mixed estuary, the river flow/tidal prism ratio is highly variable, mainly due to the neap/spring tidal cycle.

2. Meteorological Characterization

2.1. Wind

The weather in the continental Portuguese coast is conditioned by permanent factors (cosmic and geographic) as well as temporary factors such as meteorological phenomena and geophysical features. The prevailing meteorological conditions are mostly affected by the permanent factors, namely the latitude, the orography, the Atlantic Ocean influence and the continental influence. The North/South alignment of the West coast is also a factor to be considered.

In the winter there is a predominance of maritime air masses and North and North-Westerly winds associated to the Azores High circulation. Occasionally, due to the Continental High Pressure the wind veers to North-East or East, with cold dry air blowing from the interior. The rain and storms are associated to Low Pressure systems coming from the North Atlantic, with warmer South and South-Westerly winds blowing from the sea.

During the summer, the weather conditions tend to be very stable due to the jointly influence of the North-Eastern trough of the Azores High and the Iberian Peninsula thermal Low Pressure.

The previously mentioned coastal alignment is determinant for the establishing of local breezes, with daily periodicity, originated by the unequal heating and cooling of the surface of the sea and the land. These regional breezes are sometimes stronger than the regular geostrophic winds.

In Viana do Castelo local winds are superimposed upon the larger scale geostrophic wind systems, i.e. the wind direction is influenced by the sum of global and local effects. When larger scale winds are light, local winds dominate the wind patterns.

Another feature present at Viana do Castelo is the existence of a mountain system nearby, thus affecting the overall wind circulation.

Due to the combination of all these particularities there is a local breeze known as “nortada” that blows steadily from the North/North-West during the summer months, mainly in the afternoon, commonly exceeding the 25 knots.

This breeze has its peak one or two hours before sunset, decreasing throughout the first night hours. The wind then veers East and blows from that direction until the first morning hours. The greater the thermal diurnal amplitude, the stronger these breezes become.

Frequency (%) and Average Speed (km/h)																	Calm	Avg Speed (km/h)
	N		NE		E		SE		S		SW		W		NW			
	f	*s*	*f*	*s*	*f*	*s*	*f*	*s*	*f*	*s*	*f*	*s*	*f*	*s*	*f*	*s*		
Jan	18.0	6.7	24.0	5.4	9.3	5.8	5.2	6.8	8.4	14.2	12.1	12.6	8.7	13.0	8.1	9.4	6.0	8.2
Feb	15.6	6.6	19.2	5.6	7.0	5.8	3.7	8.4	11.8	17.1	17.0	15.1	11.7	14.0	10.0	9.6	4.0	9.3
Mar	18.6	8.4	20.3	5.7	7.7	6.3	3.7	7.2	7.2	17.5	14.5	12.3	13.1	11.4	12.1	13.4	2.8	8.9
Apr	15.2	11.1	18.9	8.0	12.1	7.1	5.0	6.1	6.8	14.5	13.3	12.3	12.5	12.0	14.8	15.1	1.3	9.4
May	12.8	11.2	13.1	7.5	9.1	7.7	5.2	4.9	9.5	11.1	17.8	11.3	15.1	10.7	16.7	14.6	0.5	9.5
Jun	11.5	12.1	13.1	7.6	9.7	6.3	5.5	5.8	10.2	9.5	18.5	8.7	14.5	10.4	16.3	13.2	0.8	8.5
Jul	13.4	10.6	12.6	8.2	9.8	6.3	6.0	5.0	9.5	6.6	20.1	8.5	14.4	9.1	13.4	12.7	1.0	8.0
Aug	15.0	10.6	14.0	7.4	9.6	5.5	4.6	4.4	7.5	7.0	16.2	7.4	13.5	10.0	17.3	12.4	2.3	7.7
Sep	13.6	5.8	15.8	5.7	10.5	5.0	4.8	5.2	9.5	10.6	16.8	8.1	14.2	8.9	11.9	9.4	2.8	6.9
Oct	17.9	4.8	18.9	4.4	9.0	5.8	6.2	6.2	10.4	13.9	13.4	10.4	10.0	10.5	11.2	9.2	3.1	6.9
Nov	16.4	4.9	25.3	4.8	11.5	6.0	6.3	8.0	9.7	12.2	11.3	9.6	5.6	9.1	6.7	8.7	7.1	6.7
Dec	13.6	6.1	23.8	5.1	11.0	5.3	4.9	7.6	13.1	16.4	13.3	15.2	8.0	13.7	7.6	9.0	4.8	8.2
Yearly	15.1	8.1	18.2	6.0	9.7	6.1	5.1	6.2	9.5	12.6	15.4	10.8	11.8	10.9	12.2	11.9	3.0	8.2

Table 1. Wind frequency and speed at Viana do Castelo (1961/90)
Source, Portuguese Meteorological Institute

The table provided by the Portuguese Meteorological Institute (Table 1) is not particularly easily read, rendering it inadequate for a good visual analysis for any given month. In order to overcome this, it was decided to create wind roses for every month. These are presented below.

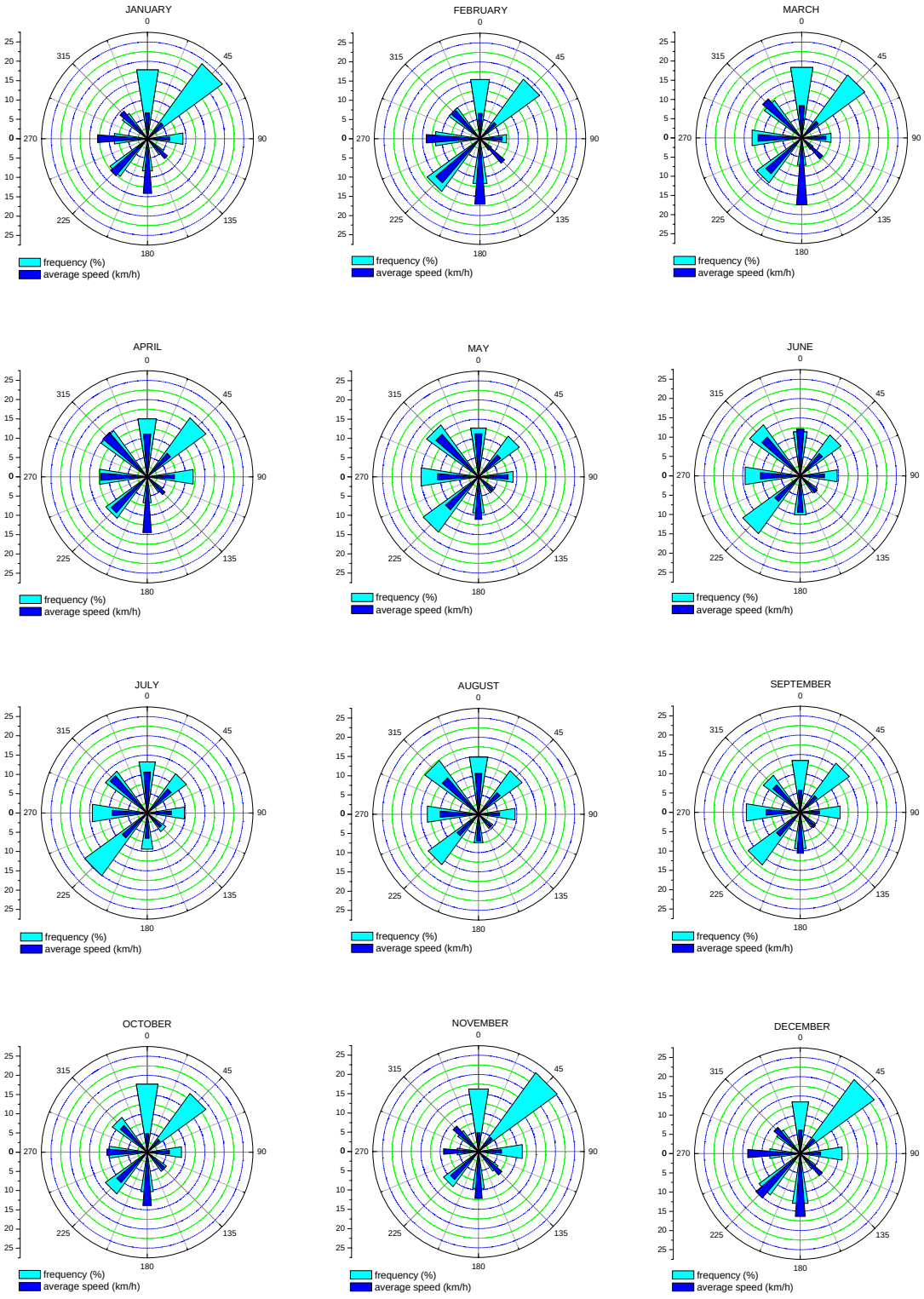

Fig. 4. Wind Roses, January through December (the length of the segments is to be read on the scale, both in frequency and average speed)

It is quite clear that in the winter months the South/Southwest winds are much stronger although less frequent and the summer is characterized by the previous mentioned strong North/North-westerly winds (Fig. 4).

These wind roses allow for an easier and direct reading of the frequency and average wind speed for a certain month.

The frequency of calmness days (Fig. 5) is also an interesting issue since contrary to what would be expected, the highest values are recorded on the winter months. This has its cause on the prevailing local wind regime on the summer months (“Nortada”) that superimpose on the larger scale geostrophic winds, maintaining an almost constant Northerly breeze.

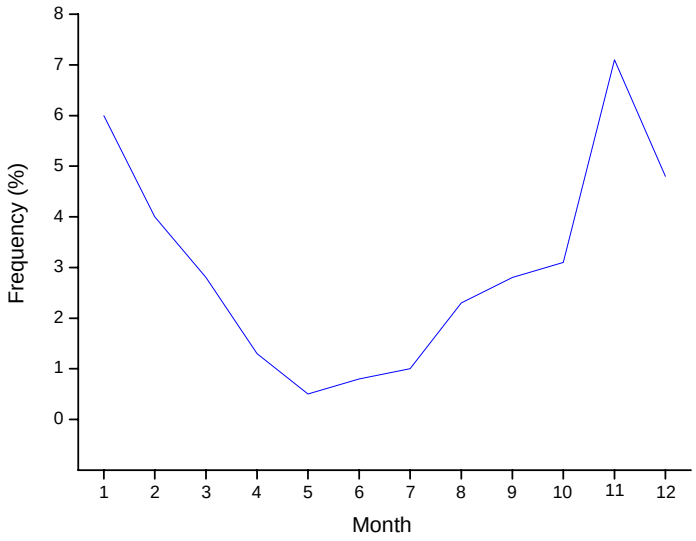

Fig. 5. Frequency of calmness days

2.2. Atmospheric Pressure

The monthly average values of atmospheric pressure on the Portuguese coast are comprised between 1016 and 1020 hPa (Instituto de Meteorologia). The highest values (higher than 1030 hPa) take place at the winter, associated to the development of a continental High Pressure. The lowest values are characteristic of deep Low Pressures also occurring at the winter but with less persistence, although pressure can drop to less than 980 hPa (Fig. 6).

There is a semidiurnal pressure variation described as barometric tide, with a range of about 1 hPa. The highest values are attained at 1000 and 2200 UTC and the lowest at 0400 and 1600 UTC (Instituto de Meteorologia).

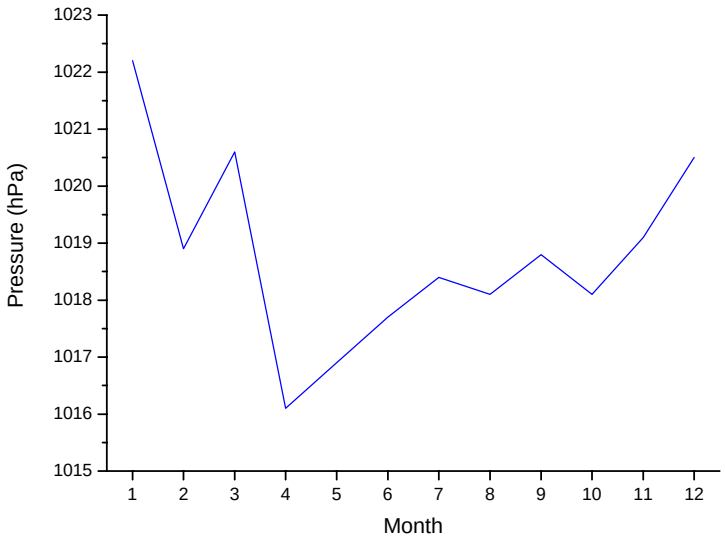

Fig. 6. Average pressure at sea level (1970/90)

2.3. Study of a Storm Surge Occurrence

The issue of the atmospheric pressure combined with the wind circulation is of the utmost importance since these two phenomena combined introduce additional complication in tidal prediction, by changing the height of a particular tide, and/or the time at which it occurs.

In fact, a 10 meter (1000 cm) column of water corresponds to one atmosphere of pressure (1000 mbar = 1000 hPa), so 1 cm of water corresponds to 1 hPa. Thus, a reduction in pressure of 20 hPa would result in a sea level rise of 20 cm. This phenomenon is known as the inverted barometer effect.

The inverted barometer effect is the theoretical response of the ocean to changing atmospheric pressure. When pressure falls, sea level rises, and when pressure rises, sea level falls.

In this way, the combined effect of strong winds and low atmospheric pressure can lead to a temporary increase in sea level above the expected tidal level, termed positive storm surges, which enhances the risk of flooding. On the other hand, abnormally low sea level, termed negative storm surges, may occur during periods of high atmospheric pressure combined with strong offshore winds, with important consequences to port navigation. Within the scope of this work only the positive storm surge will be analysed and will be referred to as storm surge.

Strong winds associated with low pressure systems moving from the West to the East are the primary generating mechanism for the positive storm surges on the Portuguese coast, which, if coincident with substantial astronomic tides, can produce exceptionally high sea surface levels.

Essentially, the storm surge phenomenon is mainly important along the coastline, has an inherent local character and is highly

influenced by small-scale coastline geometry and bottom topography. A storm surge usually propagates along the coast as a Kelvin wave and although affecting large areas, a single surge event will have different local impacts depending on the local topography and bathymetry [Debernard *et al.*, 2002].

For the purpose of this work, instead of searching for storm surge evidence in the tidal gauge records, a different approach was taken. Given the availability of meteorological data from Viana Pilot Station, namely barograph and daily weather observation records, it was decided that it would be interesting to search for a particular date, or period, where the meteorological data would point to the likelihood of a storm surge occurrence and then check the tidal records to confirm it.
Two factors would have to be present, an obvious fall of the atmospheric pressure within a relative small period of time, associated to strong winds from the West quadrant.

Following a methodical examination of the records one period stood out. The chosen dates were the last two days of October 2003, when a deep fall of the barometer was recorded (from 1018 hPa to 991 hPa in just 10 hours) and the port was closed to navigation due to 50 knots Southwesterly winds and 7 meter breaking waves at port entrance (Fig. 7).

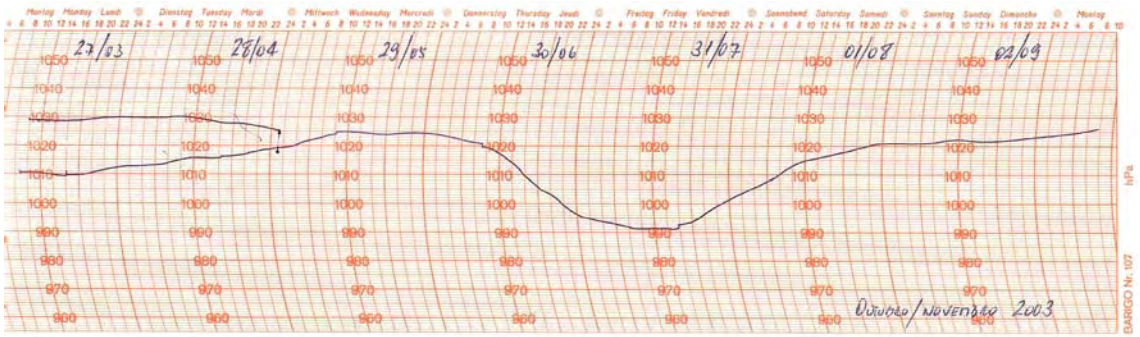

Fig. 7. Barograph records for the 30th and 31st October 2003

Because the atmosphere and the ocean form one system and, if either is to be understood properly, must be considered together,

it was decided to analyse carefully the atmospheric circulation during the above mentioned period.

From the study of the surface analysis chart at 0600 UTC of the 30th October (Fig. 8) it is quite clear the development of a low pressure system with its centre (971 hPa) located West of the British Isles.

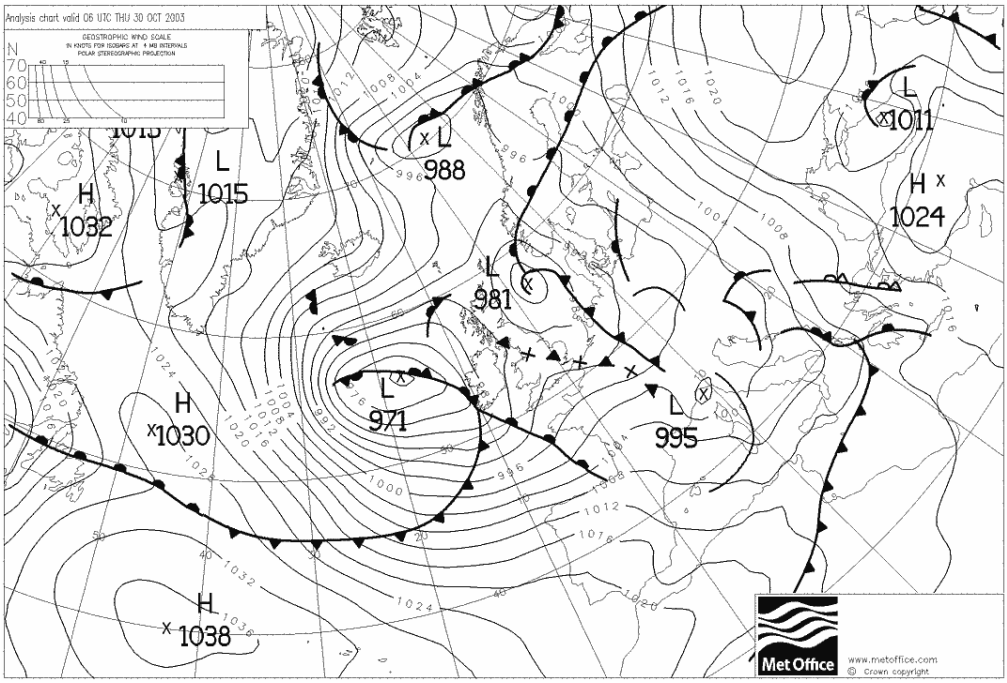

Fig. 8. Analysis chart 0600 UTC, 30th October 2003. © Crown copyright 2003 Published by the Met Office

Just 24 hours later (Fig. 9) the low pressure system centre has moved to the Bay of Biscay and deepened to 964 hPa. The north-westerly part of the Iberian Peninsula is now under the effect of West and Southwesterly strong winds, as can be shown by the relative closeness of the isobaric lines.

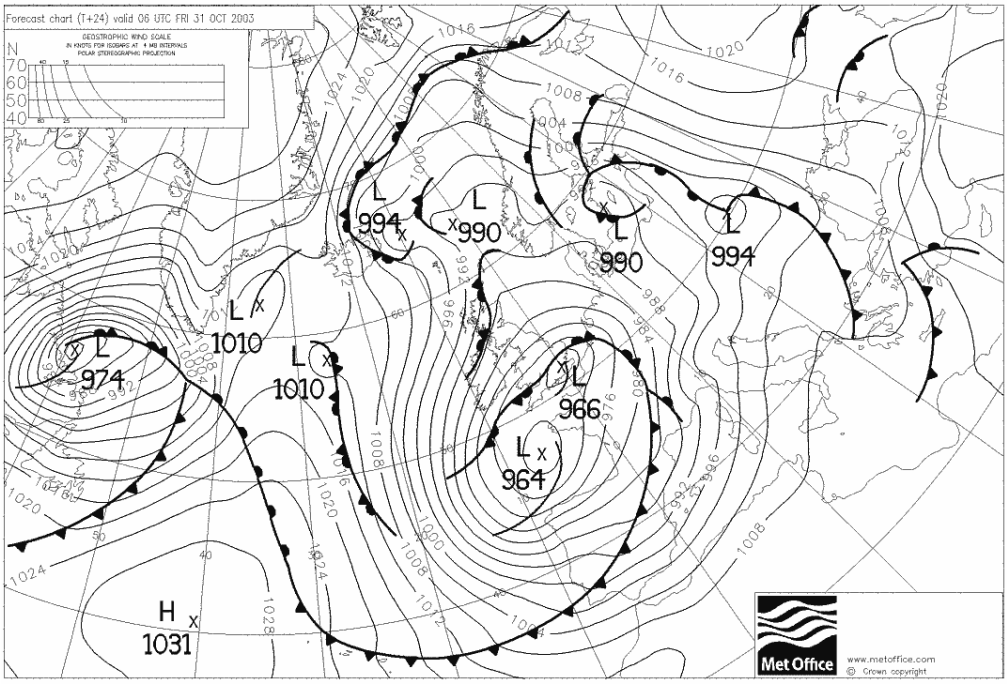

Fig. 9. Analysis chart 0600 UTC, 31st October 2003. © Crown copyright 2003 Published by the Met Office

Upon completion of the analysis of the causes of the severe weather registered, the records of the tidal gauge were checked for a possible storm surge occurrence during that period.

After plotting the tidal gauge data, one week before and one week after the passage of the atmospheric low pressure system, it became evident that a significant storm surge had occurred, with sea level reaching about 0.70 meters above predicted tidal level for 31st of October 2003. Since this occurrence coincided with an average tide between spring tides and neap tides and the maximum differences were recorded close to low water, the local effects went unnoticed.

Nevertheless, the tidal gauge record is quite revealing of the magnitude of the surge, as can be seen below, displaying the typical distortion of the tidal sinusoidal (Fig. 10).

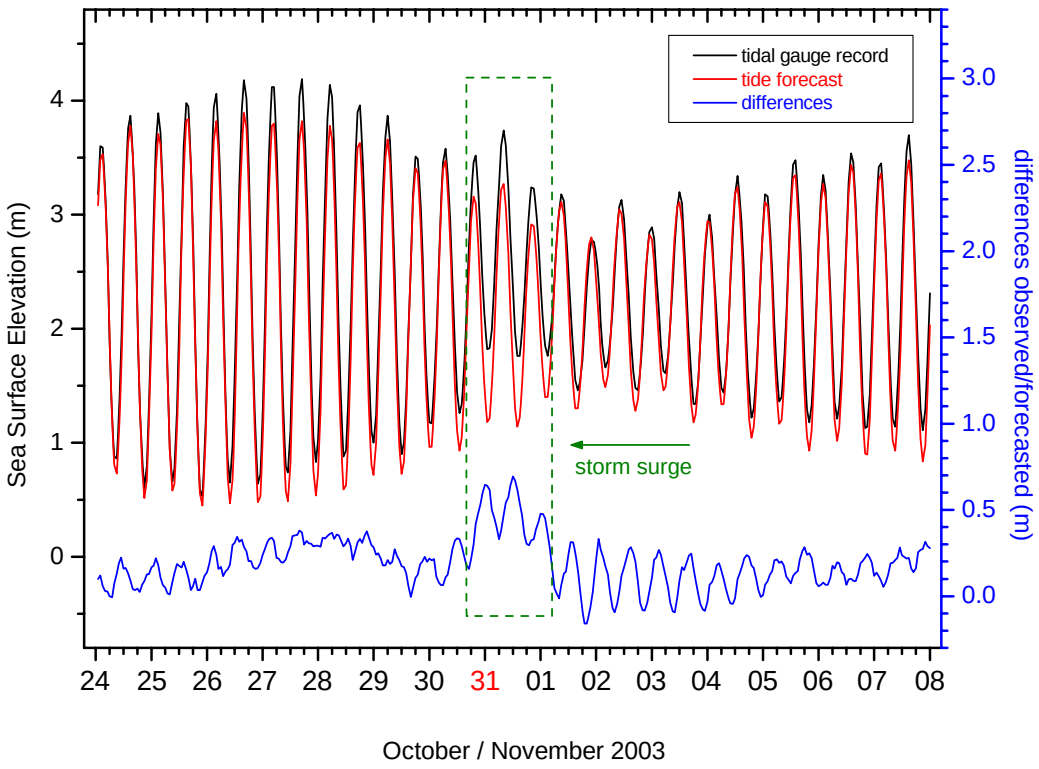

Fig. 10. Tidal gauge record plotted against tidal prediction and the observed differences.

The systematic differences between observed and forecasted tidal levels shown on the plot are due to the varying Mean Sea Level, and this subject is further developed on this work at the tidal analysis section.

There is a marked increase in the differences on the first hours of the 31st, corresponding to the lowest values of barometric pressure attained as well as the strongest wind period.

The first hours of the 31st are in fact the most interesting ones, thus, a finer focus on this period was decided, plotting the recorded sea level, the forecasted tidal level and their differences against the barometric pressure for the same period (Fig. 11).

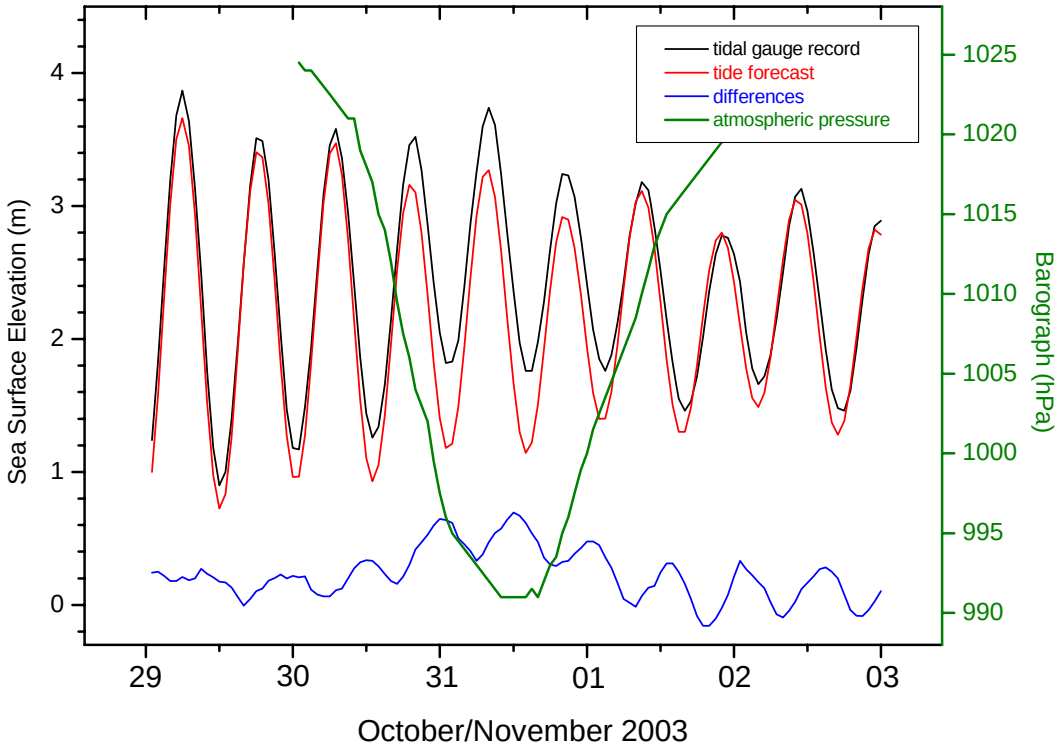

Fig. 11. Sea level recorded, tidal forecast, their differences and the barometric pressure.

From Figure 11, is quite evident the dramatic drop on the atmospheric pressure since the first hours of the 30th, reaching the lowest values by mid 31st. Interesting to note that the increase in the expected sea level started when the wind was at its maximum speed, during the passage of the front.

At this stage it was found useful to apply a filter and separate the lower frequencies of the meteorological effects from the higher frequencies of the astronomic tide (Fig. 12). The filter was applied with a 2.78 X 10^{-4} Hz sampling frequency, a 9.3 X 10^{-6} Hz valley to separate low pass and high pass and a 2.78 X 10^{-4} Hz upper frequency limit for high pass.

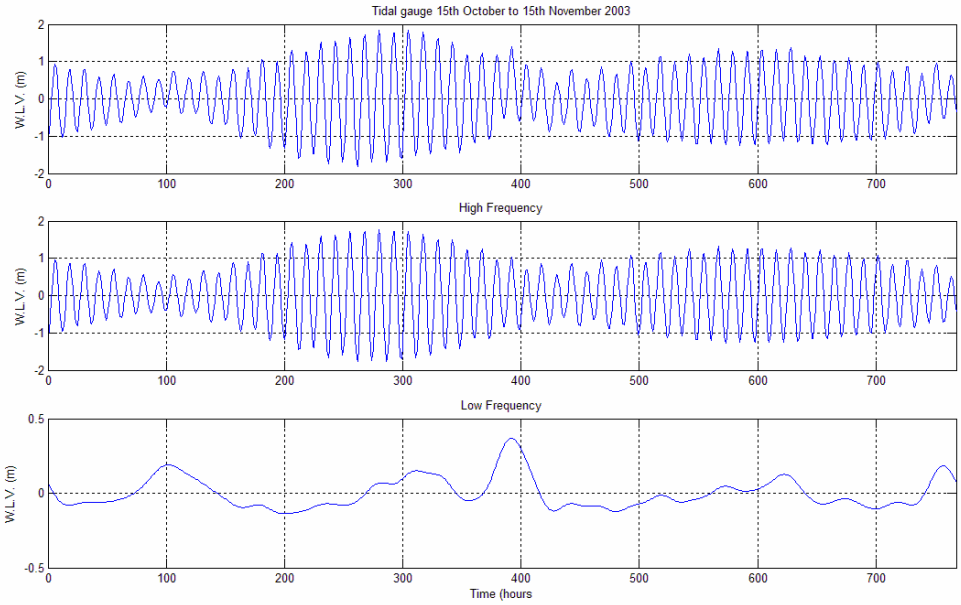

Fig. 12. Meteorological effects filtering.

From Fig. 12 it is quite clear the relevance of the meteorological phenomena during the analyzed period. On the first plot where the total tide is displayed, several distortions to the semidiurnal sinusoidal are clearly visible. These become more visible after being removed from the total tide plot, with the astronomic tide shown on the second plot and the filtered meteorological effects on the bottom one.

It is important to bear in mind that an alteration (increase) of the extreme coastal storm surge events is a potential consequence of climate change, which, from an impacts point of view, will be of more concern than the slow inundation of coastal areas by century scale changes in mean sea level [Lowe *et al.*, 2001].

3. Estuary Hydrological Characterization

3.1. Lima River Discharge

Fresh water flow from a river into an estuary varies from short-term responses to local storms and energy production from dams, to long-term seasonal wet and dry cycles. In some estuaries the volume of freshwater is sufficient to maintain a density difference over large distances before being completely mixed into seawater [Martin and McCutcheon, 1999].

Within the scope of this study the main factors contributing to changes of the river flow being discharged into the port area are the direct rainfall on the open water surface, the runoff of rainfall over the surrounding drainage basins and the hydroelectric plants of Alto Lindoso and Touvedo, located on the River Lima, close to the Spanish border.

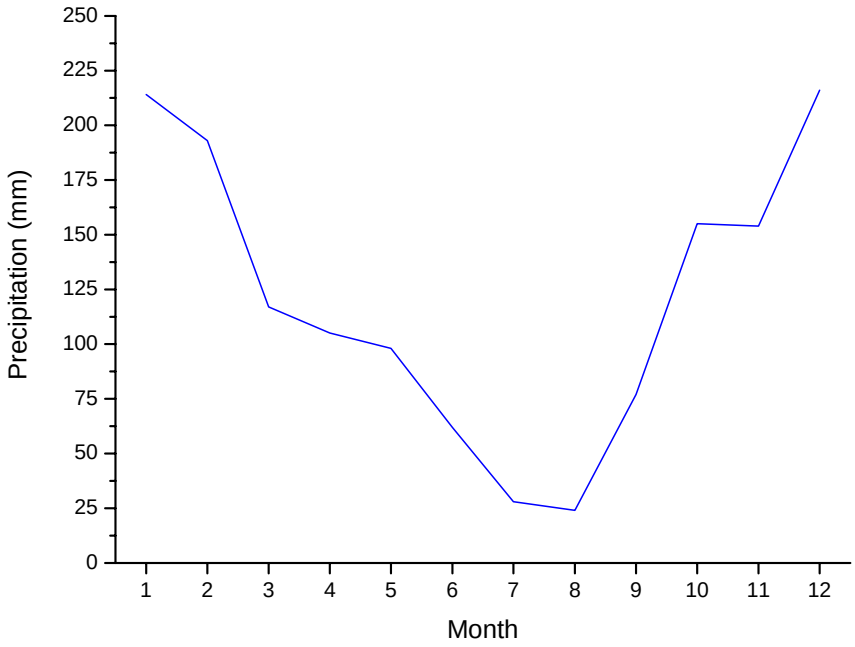

Fig. 13. Average values for total precipitation (1970/90)
Source: Portuguese Meteorological Institute

Regarding the precipitation (Fig. 13), the values for the Lima catchment are the highest in Portugal, with minimum averages at July and August and maximums at January and December. At Viana do Castelo the annual total mean value is 1444 mm. Averagely, there are about 52 days annually with precipitation values above 10 mm [Instituto de Meteorologia]. It is clear that precipitation, as a function of time and space, is highly variable, making it extremely difficult to estimate the inherent variations to the river runoff. This difficult task is enhanced by the fact that some rain water flows over the soil surface as surface runoff and other water infiltrates through the soil surface and flows beneath the surface to the stream. This groundwater contribution to the stream flow cannot fluctuate rapidly because of its very low flow velocity [Park *et al.*, 2004]

As for the 1992 built hydroelectric plants of Alto Lindoso and Touvedo (Fig. 14), these facilities have a great impact on the river flow, particularly the latter.

The Touvedo dam, located about 17 km downstream of Alto Lindoso, has the task of modulating this dam's high turbinated throughput (about 250 m^3s^{-1}) by temporarily retaining the water and redelivering it to the river under 100 m^3s^{-1}, thus avoiding large and sudden variations to the river flow.

Fig. 14. Location of Alto Lindoso and Touvedo dams

This use of water for hydropower production, modifying the river normal flow regime, is extremely important since increased freshwater inflow can change the character of an estuary from well-mixed to partially mixed or stratified. Decreased inflow can have the opposite effect with a concomitant increased upstream intrusion of seawater [Martin and McCutcheon, 1999].

These dams also introduce an increased difficulty in estimating the river flow for modelling purposes. Different values have been cited in the literature. MARETEC - Marine and Environmental Technology Centre and INAG – National Water Institute [www.maretec.mohid.com] carried out a study back on 2001 whose main goal was to define the downstream limits of the Portuguese Estuaries, using the water modelling system MOHID. For this project a mean annual flow of 62 m^3s^{-1} was chosen although for typical summer conditions a flow of 3.4 m^3s^{-1} was used.

For the environmental stream flow computation downstream of Touvedo dam [Lopes *et al.*, 2001] different values were used, namely: 4 m^3s^{-1}, 20 m^3s^{-1}, 50 m^3s^{-1} and 100 m^3s^{-1}, the first value being the minimum guaranteed ecological discharge and the last the maximum turbine capacity of the dam. The two other values are intermediate situations.

On the study of the salt water intrusion in the Lima Estuary [Pinho and Vieira, 2007] four different scenarios were simulated for the river discharge, namely 9 m^3s^{-1} (the mentioned guaranteed mean discharge during the dry season), 54 m^3s^{-1} (the annual mean discharge), 31.5 m^3s^{-1} (intermediate situation) and 300 m^3s^{-1} corresponding to a typical value for hydropower generation periods (although these authors consider the jointly capacity of 250 m^3s^{-1} of both dams).

The available data from INAG – National Water Institute (flow time series from 1980 to 1990, *before* the construction of the two dams)

shows average annual values of 47 m^3s^{-1} and annual peak flows ranging between 231 m^3s^{-1} and 876 m^3s^{-1}.

Given that the precise determination of the river discharge is out of the scope of this study and also taking into consideration that the river runoff is consequence of several factors, some of them unpredictable and indeterminate, it was decided, based on some empirical knowledge of the study site, to use four different values for different scenarios as an input to the model:

4 m^3s^{-1}, which is actually the legal/ecological guaranteed minimum discharge downstream of Touvedo dam.
50 m^3s^{-1}, an average annual value taking into consideration the available data and previous studies.
100 m^3s^{-1}, the maximum turbinated flow at Touvedo dam.
200 m^3s^{-1}, corresponding to extreme peak flood situations.

These river flow conditions are summarized on Table 2 below;

River flow (m^3s^{-1})	**Scenario**
4	minimum discharge
50	average annual value
100	maximum turbinated flow
200	peak flood

Table 2. River flow scenarios.

3.2. Estuary Vertical Structure

Although a comprehensive salinity stratification assessment of the estuary is out of the scope of this work, certain assumptions regarding salinity issues were made at the hydrodynamic model implementation stage, namely the vertically well mixed condition.

The vertically mixed estuary in its pure form is rarely found in nature, although many can approach the vertically mixed state when the ratio fresh water input/tidal volume is low at spring tides or during periods of very low river flow.

Given that there was a lack of information regarding the vertical salinity structure of the study area it was decided to collect field data at several locations, at low water and at high water.

The instrument used, a MINI STD model SD204, is equipped with permanent sensors for conductivity, temperature and pressure. For salinity measurements the conductivity sensor is used. The sensor is of an inductive type consisting of a primary and secondary coil centred around a quartz liner tube. The liner is used to obtain a defined water volume. The primary coil induces an electromagnetic field which drives ions through the water inside the liner in proportion with the water conductivity. The ionic flow is then measured by the secondary coil. The measured conductivity, temperature and pressure data are used to calculate salinity in accordance with equations recommended by UNESCO [MINI STD Operating Manual].

The field campaign was performed the 18th July of 2007, during the late morning Low Water and the afternoon High Water with the instrument set for a one second sampling interval. Several transects were followed with equally spaced sampling points. The transect positions are presented below (Fig. 15).

Fig. 15. Transect positions for salinity and temperature sampling

A pilot boat was employed as the survey boat (Fig. 16), with the positioning at the sampling points being assured by previously entered GPS waypoints between channel navigation buoys, as well as visual marks. A weight was attached to the STD and the device was lowered at a speed of about 1 ms^{-1}. The tidal range was 2.4 meters, with 3.3 m at HW and 0.9 m at LW, which may be considered an average tide.

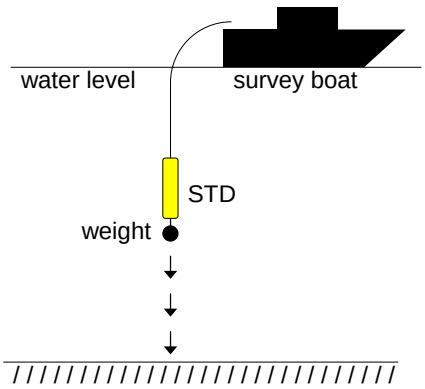

Fig. 16. Sampling procedure scheme.

The transects positions were chosen taking into account not only the necessity to sample at different distances from the estuary mouth (Table 3) but also taking advantage of the presence of navigation buoys, which assisted in the perpendicular alignment of

the boat to the channel axis during the sampling procedure. This resulted in the following transects:

Transect	Alignment	Distance from mouth
1	Nav Buoy #11	2 250 m
2	Nav Buoy #10 - #9	1 450 m
3	Nav Buoy #6 - #5	950 m
4	Nav Buoy #3 - #4	650 m

Table 3. Salinity and Temperature transects

Since the distance between the sampling points within each transect provided a reasonable resolution, it was decided to create salinity and temperature cross-sections using an interpolation technique for the graphical plot. A triangulation with linear interpolation method which uses the optimal Delaunay triangulation was chosen. The algorithm creates triangles by drawing lines between data points. The original points are connected in such a way that no triangle edges are intersected by other triangles. The result is a patchwork of triangular faces over the extent of the grid. This method is an exact interpolator. Each triangle defines a plane over the grid nodes lying within the triangle, with the tilt and elevation of the triangle determined by the three original data points defining the triangle. All grid nodes within a given triangle are defined by the triangular surface. Because the original data is used to define the triangles, the data is honoured very closely [Guibas and Stolfi, 1985].

Nevertheless, along with each section, a graphical profile of a sampling point taken in the axis of the channel is shown, for each transect.

TRANSECT 1 (Fig. 17)

Fig. 17. Sampling stations for Transect 1

Results for Low Water condition, showing sampling stations and depths of records (Fig. 18 and 19):

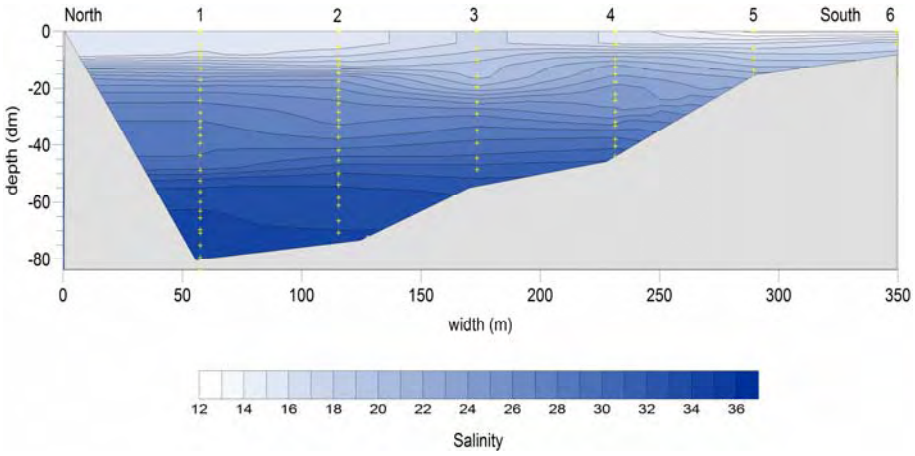

Fig. 18. Salinity section at Low Water (T1)

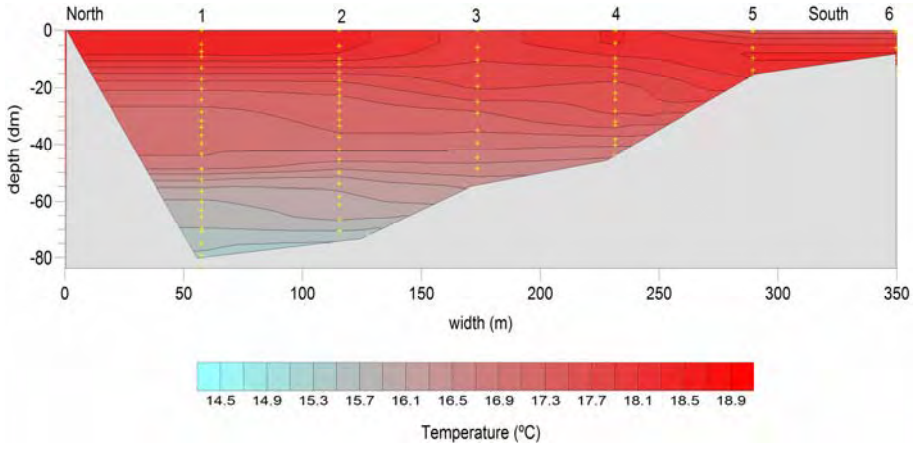

Fig. 19. Temperature section at Low Water (T1)

Results for High Water, showing sampling stations and depths of records (Fig. 20 and 21):

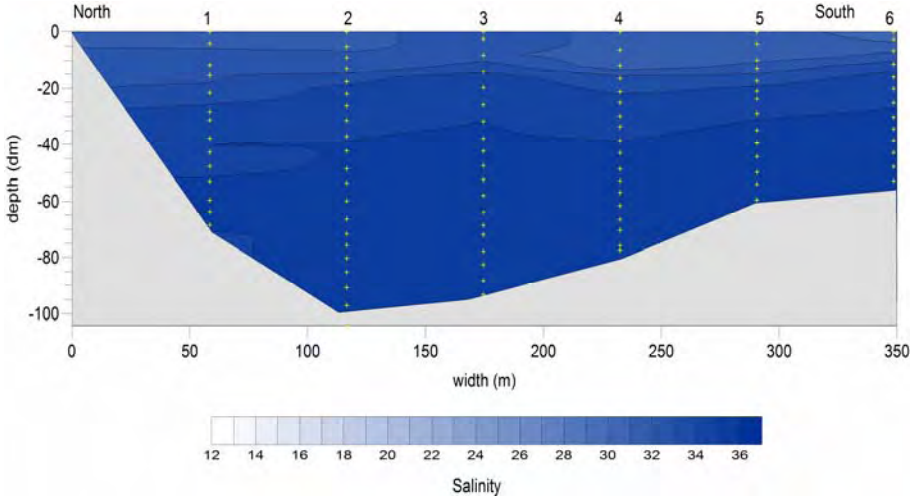

Fig. 20. Salinity section at High Water (T1)

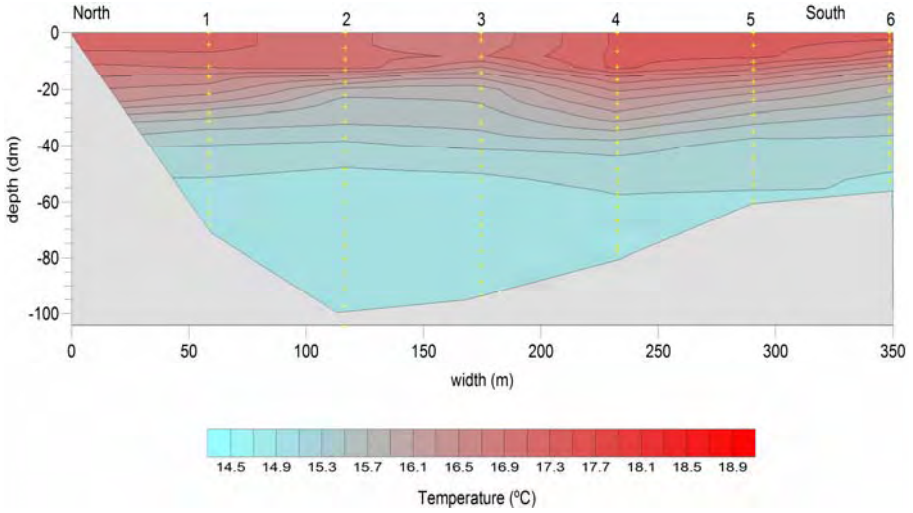

Fig. 21. Temperature section at High Water (T1)

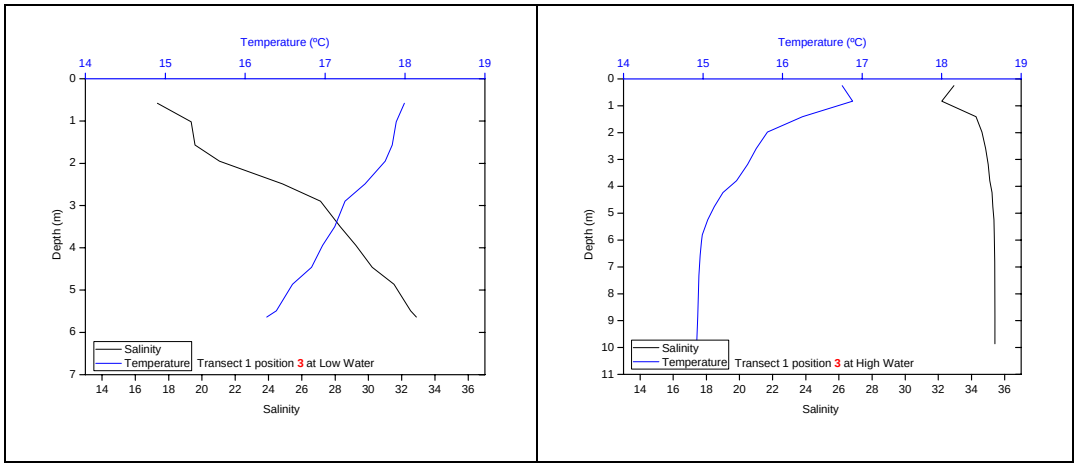

Fig. 22. Salinity and temperature vertical profiles at LW and HW for T1, position 3.

TRANSECT 2 (Fig. 23)

Fig. 23. Sampling stations for Transect 2

Results for Low Water condition, showing sampling stations and depths of records (Fig. 24 and 25):

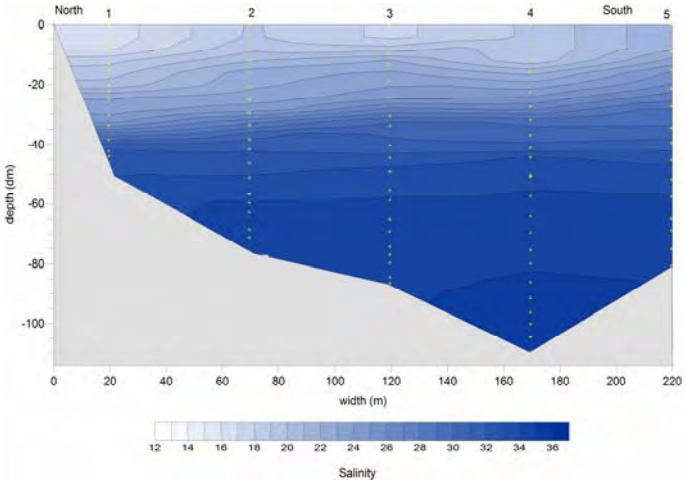

Fig. 24. Salinity section at Low Water, T2

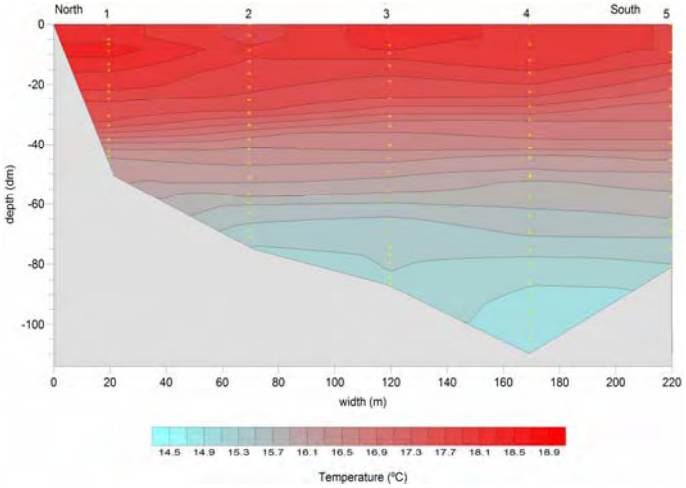

Fig. 25. Temperature section at Low Water, T2

Results for High Water condition, showing sampling stations and depths of records (Fig. 26 and 27):

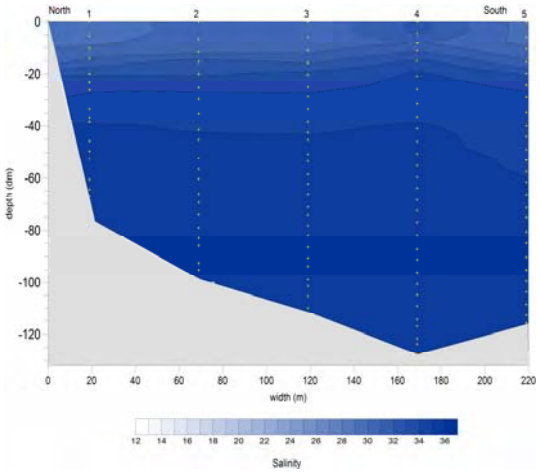

Fig. 26. Salinity section at High Water, T2

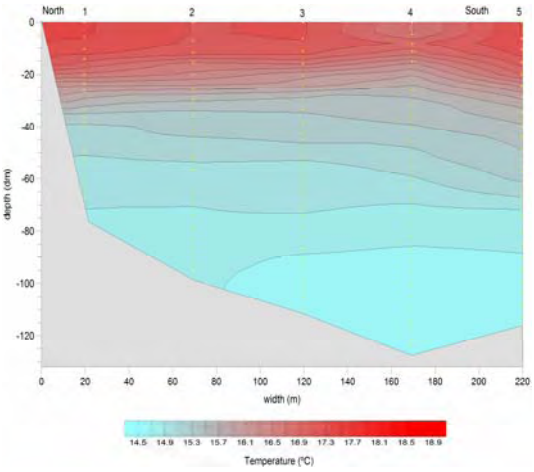

Fig. 27. Temperature section at High Water, T2

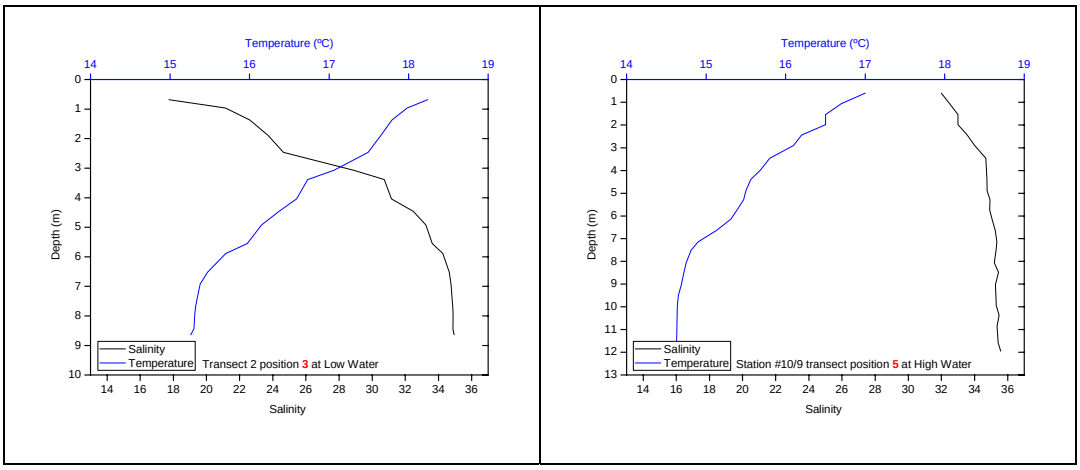

Fig. 28. Salinity and temperature vertical profiles at LW and HW for T2, position 3.

TRANSECT 3 (Fig. 29)

Fig. 29. Sampling stations for Transect 3

Results for Low Water condition, showing sampling stations and depths of records (Fig. 30 and 31):

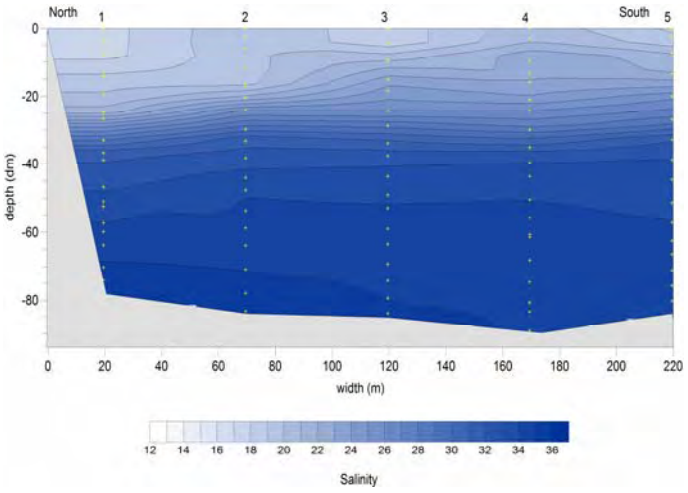

Fig. 30. Salinity section at Low Water, T3

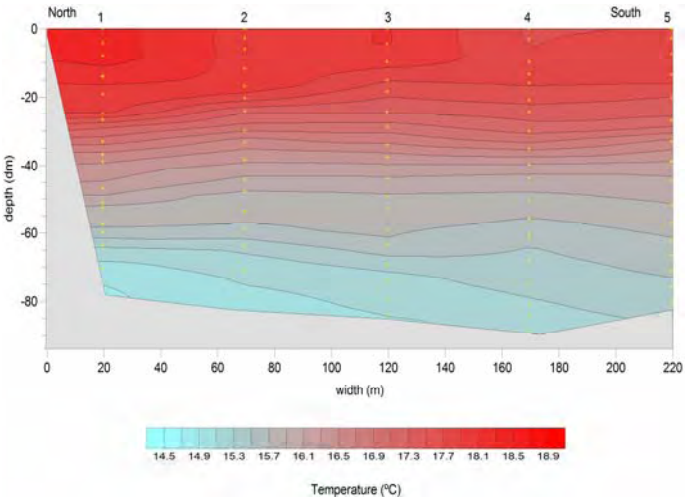

Fig. 31. Temperature section at Low Water, T3

Results for High Water condition, showing sampling stations and depths of records (Fig. 32 and 33):

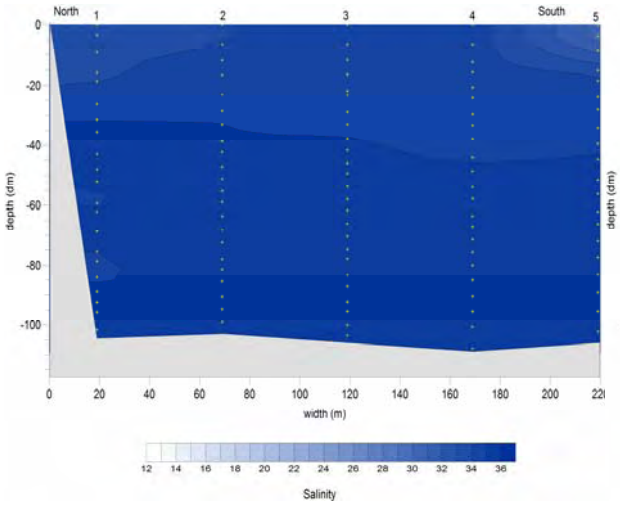

Fig. 32. Salinity section at High Water, T3

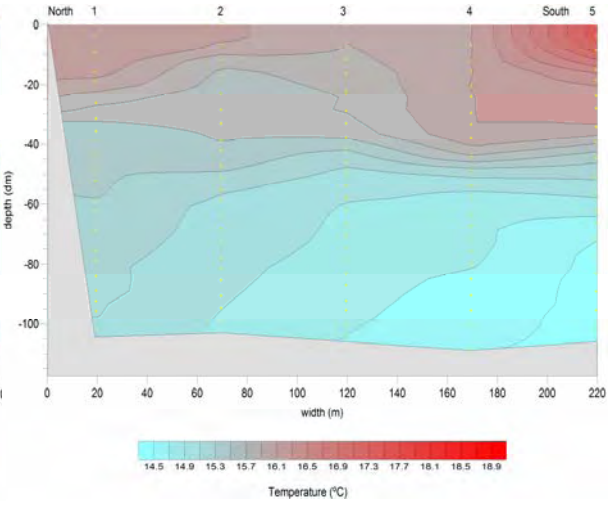

Fig. 33. Temperature section at High Water, T3

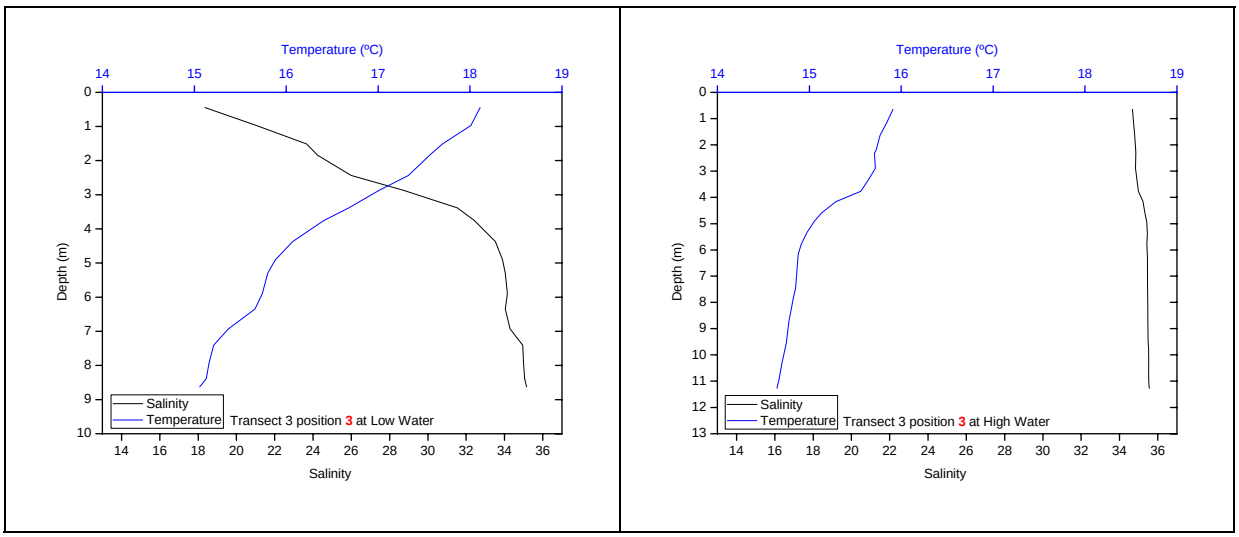

Fig. 34. Salinity and temperature vertical profiles at LW and HW for T3, position 3.

TRANSECT 4 (Fig. 35)

Fig. 35. Sampling stations for Transect 4

Results for Low Water condition, showing sampling stations and depths of records (Fig. 36 and 37):

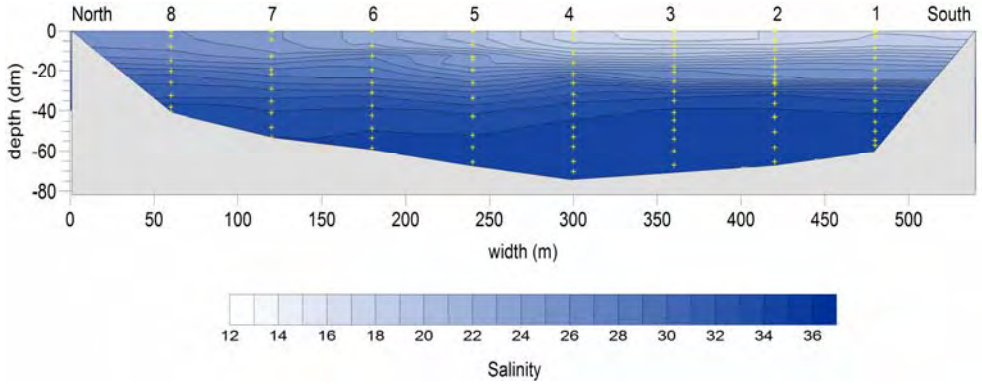

Fig. 36. Salinity section at Low Water, T4

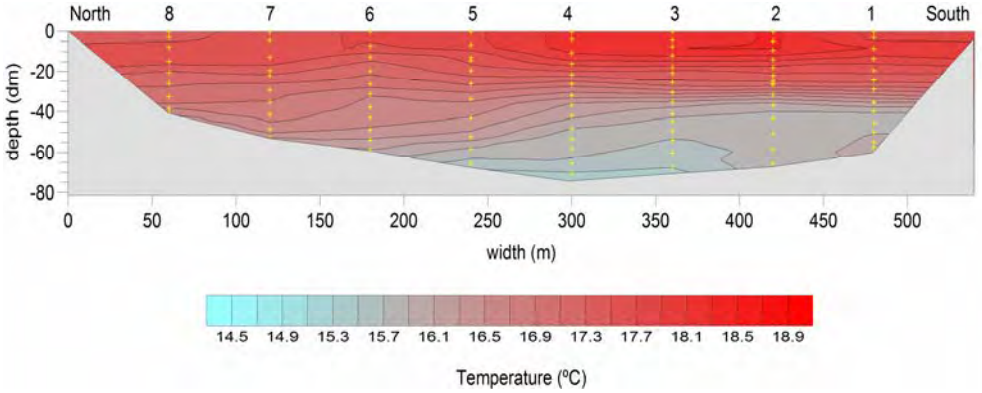

Fig. 37. Temperature section at Low Water, T4

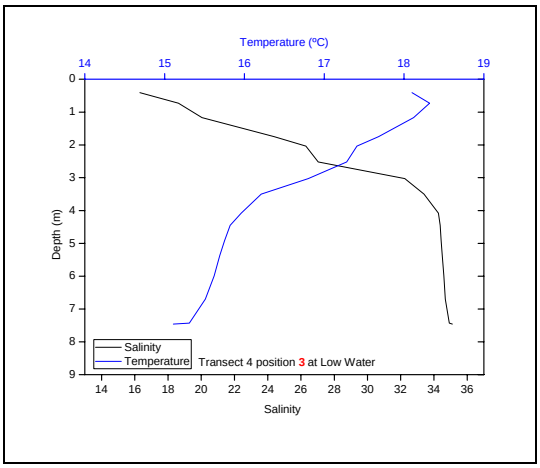

Fig. 38. Salinity and temperature vertical profiles at LW for T4, position 3.

No readings at High Water were taken for transect #3/4 since the proximity of port entrance and the measurements at HW for the other transects suggest a well mixed and homogeneous condition from sea level to the bottom.

From the plotted cross-sectional structures as well as the vertical profiles (Figs. 22, 28, 34 and 38) it is clear that vertically well mixed conditions only occur close to high water, with the flooding tide acting as the driving agent for turbulence mixing.

Also, taking into account that sampling took place in the dry season, the river flow shows a bigger influence than was firstly anticipated. In fact a slight stratification occurs on the upper layer of the water column with salinity ranging between ~20 and ~30 on the first three meters.

Since stratification is dependent on the river flow and tidal mixing capacity, the estuary classification will be changing according to the prevailing circumstances such as low river runoff, high turbinated dam flows, neap tides or spring tides conditions. In this case the estuary may be considered vertically well mixed or partially mixed, depending on the circumstances. This changes in the salinity vertical structure of the estuary can

occur even at relatively short time scales as it quite clear from the salinity data collected from two stations where RCM9 MkII currentmeters were deployed (see Tidal Currents section). The processed data resulted in the following plots (Fig. 39 and Fig. 40):

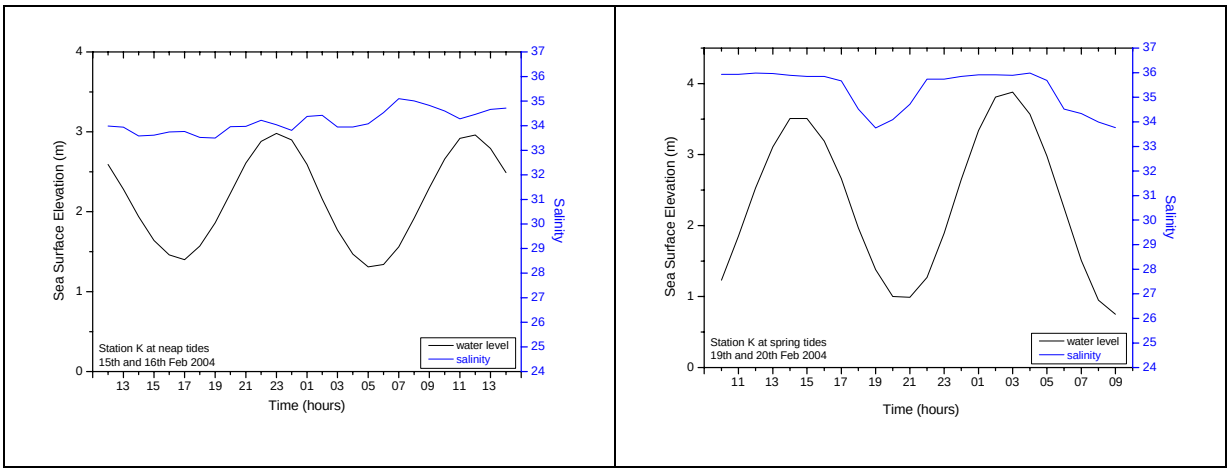

Fig. 39. Salinity and sea surface elevation for station K.

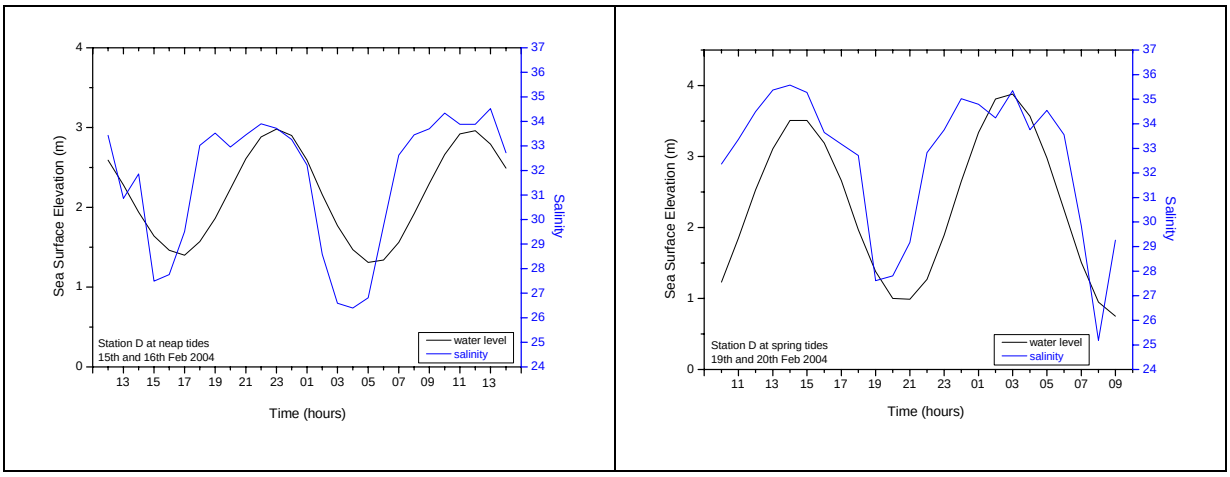

Fig. 40. Salinity and sea surface elevation for station D.

As expected, the obtained plots show a small variation on the salinity close to the estuary mouth (station K), where the oceanic influence is higher, while at station D, upstream of the port area, there is a noticeable fresh water influence on the salinity,

predominantly at low water (at station K the device was moored at a depth of 4.0 m and at station D at a depth of 2.7 m). Nevertheless the lowest salinity values observed are within the 25/27 range.

Even though these results may suggest to a certain amount the probable existence of baroclinic transport, these will be negligible for the scope of this study given the estuarine dynamics, strongly influenced by the tidal regime.

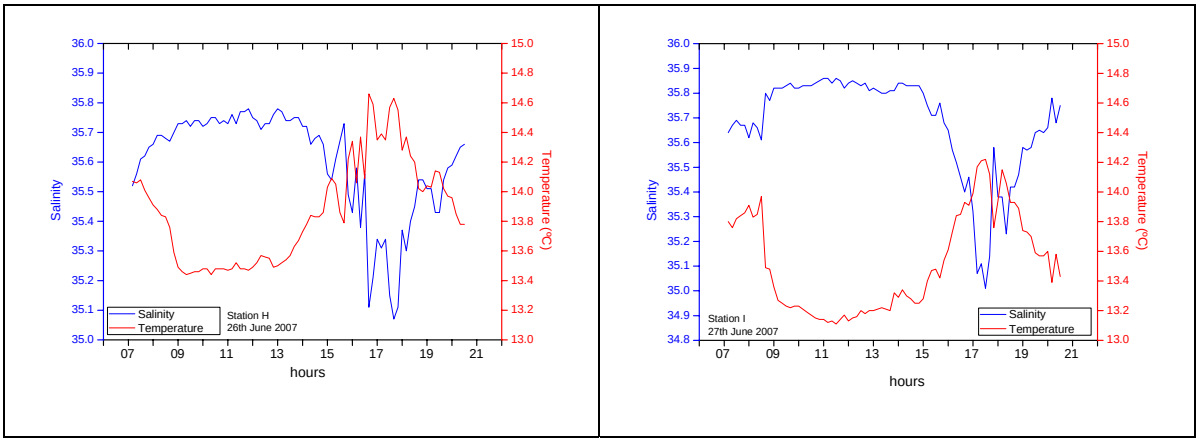

Fig. 41. Salinity and temperature for stations H and I

Within the frame of this work, on the 26th and 27th of June 2007 a measurement instrument was deployed close to navigation buoys #11 (Station H) and #9 (Station I), respectively, for a complete tidal cycle each day (Fig. 41). The purpose of this data collecting was primarily to obtain additional sea surface elevation time series for model calibration. Since the instrument, a MINI STD model SD204, is equipped with permanent sensors for conductivity, temperature and pressure, temperature and salinity data was also processed.

In the plots (Fig. 41) it is evident a certain homogeneity at the bottom, for both stations. The instrument was deployed at about 2.0 m from the bottom and, during the complete tidal cycle,

salinity varies between 35.0 and 35.8 with the lowest values observed close to low water time (18h16m UTC and 19h04m UTC for the 26th and 27th, respectively). These differences may be considered negligible.

3.3. Tidal Currents

The Portuguese Hydrographic Institute (IH) moored currentmeters at two stations located at the entrance of the port (South of fairway buoy 4) – Station K (41º40.8’N, 008º50.4’W), and downstream of the Eiffel Bridge (close to the marina entrance) – Station D (41º41.3’N, 008º49.2’W) (Fig. 42).

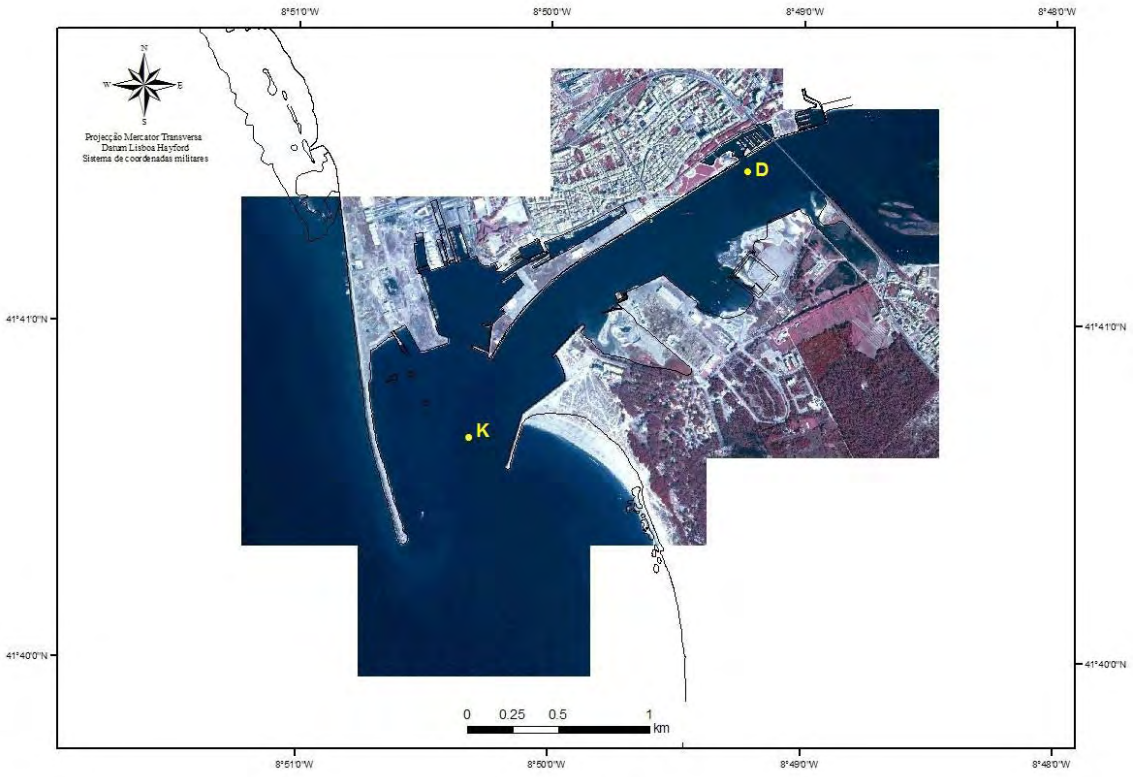

Fig. 42. Currentmeters location

The currentmeters (RCM9 MkII, Aanderaa Instruments) were moored at a depth of 4.0 meters for station K and 2.7 meters for station D and recorded the current direction and velocity for about 26 hours, at neap tides conditions and spring tides conditions.

The instruments were set to recording intervals of 10 minutes for salinity, temperature, turbidity and current velocity and direction. For the purpose of this work only salinity, temperature and current data were analysed.

The RCM9 MkII utilizes a Doppler Current Sensor 3920 for current measurements. This sensor makes use of the Doppler Shift principle as the basis for its velocity readings, by transmitting acoustic pulses of 2 MHz into the water in sequence. The current direction is found by taking the measurements along two orthogonal axes, *x* and *y*, which are referred to magnetic North by means of an internal Hall-effect compass. A microprocessor computes vector averaged speed and direction over the last sampling interval.

The Doppler sensor has a resolution of 0.3 cm/s and absolute and relative accuracies of ±0.15 cm/s and ±1% of reading, respectively, and a standard deviation of 0.5 cm/s. The Direction sensor has a resolution of 0.35º and an accuracy of ±5º for 0-15º tilt and ±7.5º for 15-35º tilt [Aanderaa Instruments]

The selected period for neap tides (15th and 16th February 2004) shows a predicted tidal range between 1.43[*1.47*] and 1.69[*1.70*] meters and HW values (between 2.70[*2.85*] and 2.81[*3.03*]) close to the MHWN level which is 2.60 meters for this port. The LW values (between 1.18[*1.31*] and 1.30[*1.40*]) are also in agreement with the MLHN level for this port (1.30), thus this period can be considered a typical neap tide condition.(The values between rectangular brackets show the observed values recorded by the tidal gauge i.e., the astronomical and meteorological tide).

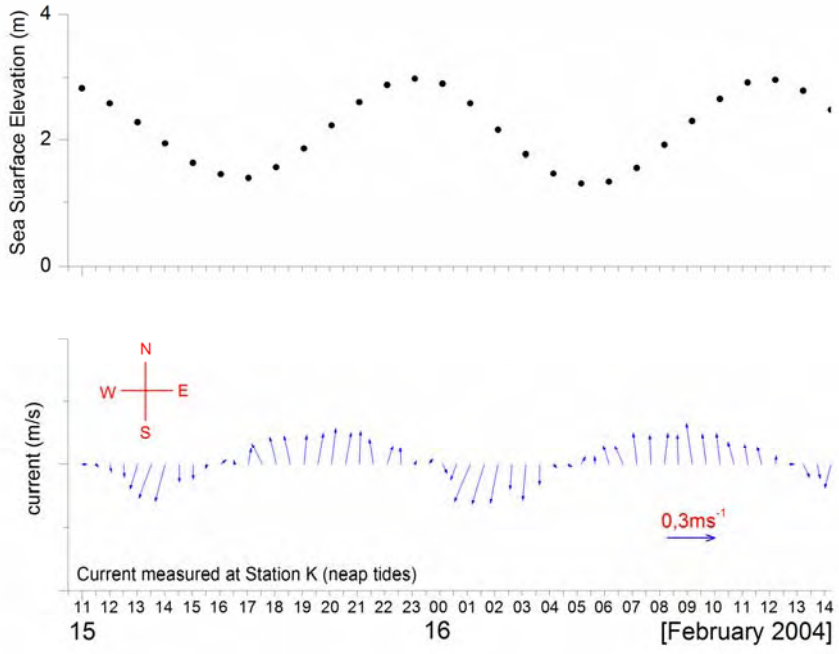

Fig. 43. Recorded current velocity and direction at station K, neap tides.

At station K (Fig. 43), maximum recorded values for current velocity were 0.36 ms^{-1} at ebb tide and 0.34 ms^{-1} while flooding. These values were recorded 2h40m after HW and 3h30m after LW, respectively.

The current direction is in agreement with the port entrance configuration, with the flooding tide generating a North current and the ebbing tide a South-Southwesterly current.

At station D (Fig. 44), maximum recorded values for current velocity were 0.69 ms^{-1} while ebbing, 4h10m after HW, and 0.41 ms^{-1} at 3h30m after LW. Here, the maximum ebbing current is almost twice the value than when flooding.

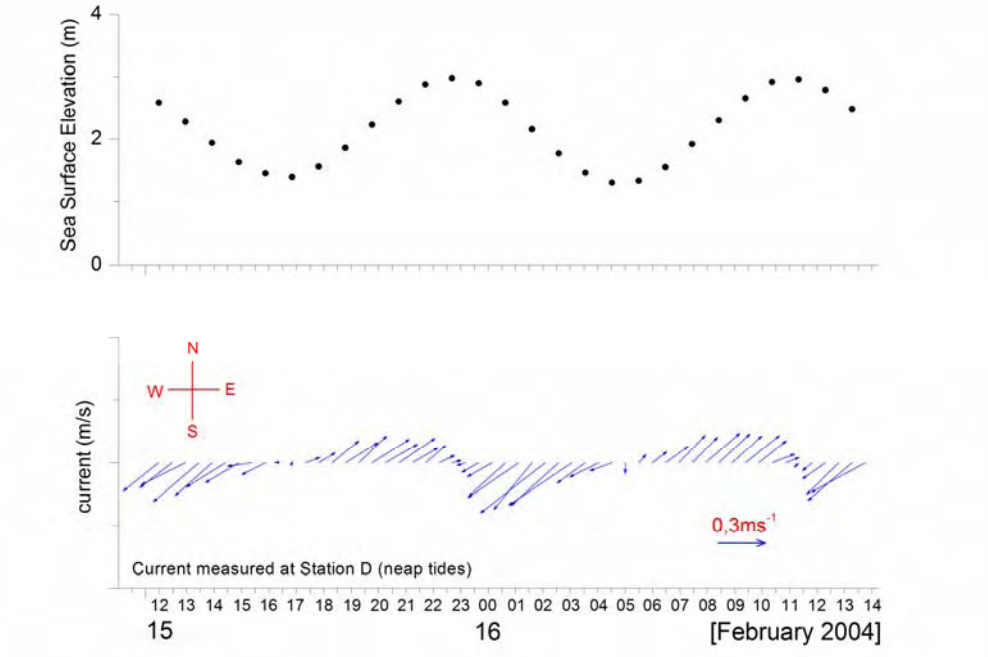

Fig. 44. Recorded current velocity and direction at station D, neap tides.

For the spring tides period, the 19th and 20th February 2004 were chosen. The predicted tidal range for these days is between 2.50[*2.65*] and 3.13[*3.21*] meters, corresponding to HW levels between 3.51[*3.30*] and 3.88[*3.62*] and LW levels between 0.75[*0.41*] and 0.99[*0.65*]. These values are in agreement with MHWS and MLWS levels of 3.40 and 0.60 meters respectively, therefore the tides chosen can be considered typical spring tides for this port. It is important to note however that extreme spring tides on this area reach 3.80 meters of range, under the proper astronomic arrangement.

During the above mentioned period, at station K (Fig. 45), maximum recorded values for current velocity were 0.82 ms^{-1} at falling tide (3 hours after HW) and 0.52 ms^{-1} at rising tide, about 3h30m after LW.

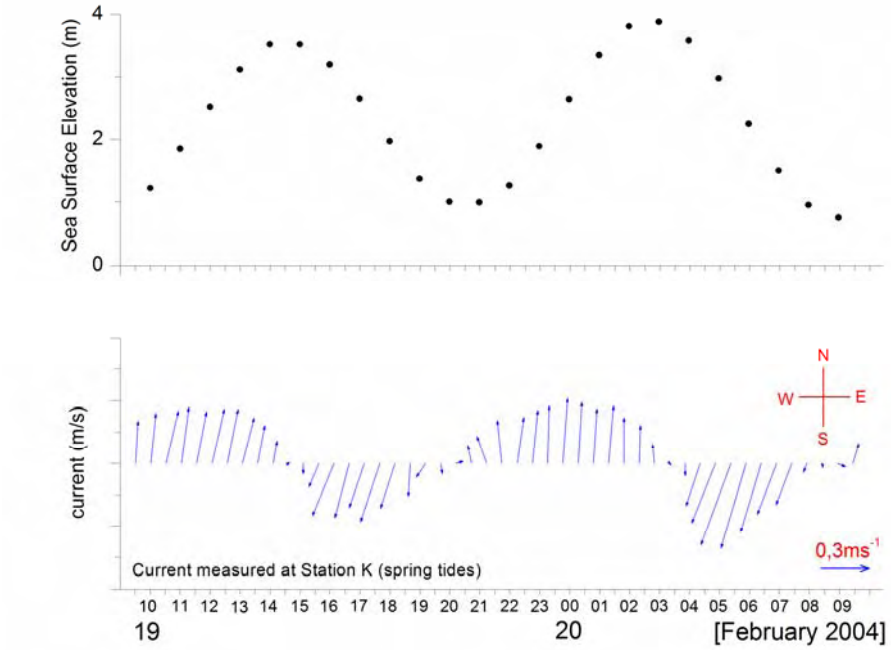

Fig. 45. Recorded current velocity and direction at station K, spring tides.

At station D (Fig. 46), the ebb tide attained current values of 1.04 ms^{-1}, 3h30m after HW. Maximum current velocity under flooding conditions was reached about 4 hours after LW, with a value of 0.65 ms^{-1}.

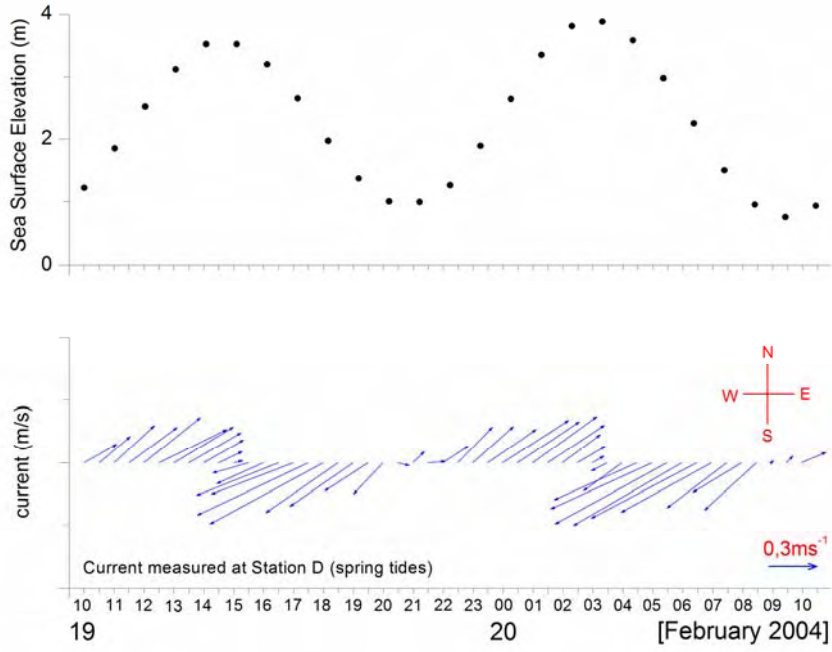

Fig. 46. Recorded current velocity and direction at station D, spring tides.

The presence of the Eiffel Bridge and the nearby bathymetry and topography introduces variations on the current. In fact, the narrowing of the river on that location changes the width dimension of the water parcel flow, which will be elongated. As the amount of water flowing into a space must equal the amount of water flowing out of it per time unit, the rate of flow, i.e., the current velocity, will become faster.

This current increase on this location was also observed on salt water intrusion modelling studies for the Lima Estuary [Pinho and Vieira, 2007]

This behaviour partially explains the much higher maximum current values observed at station D (Table 4).

Station K				Station D			
neap		spring		neap		spring	
ebb	flood	ebb	flood	ebb	flood	ebb	flood
0.36	0.34	0.82	0.52	0.69	0.41	1.04	0.65
RCM depth 4.0m				RCM depth 2.7m			

Table 4. Summary of maximum recorded tidal currents (ms^{-1})

These measured currents are obviously affected by the river discharge, since there is an adding effect of the river flow to the ebbing tide and a decrease on the flood tide velocity since the river is flowing on the opposite direction.

3.4. Tidal Analysis

The most complete and reliable data set available for this study is a one year long time series of water heights recorded at the Viana do Castelo tidal gauge, referring to 2005.

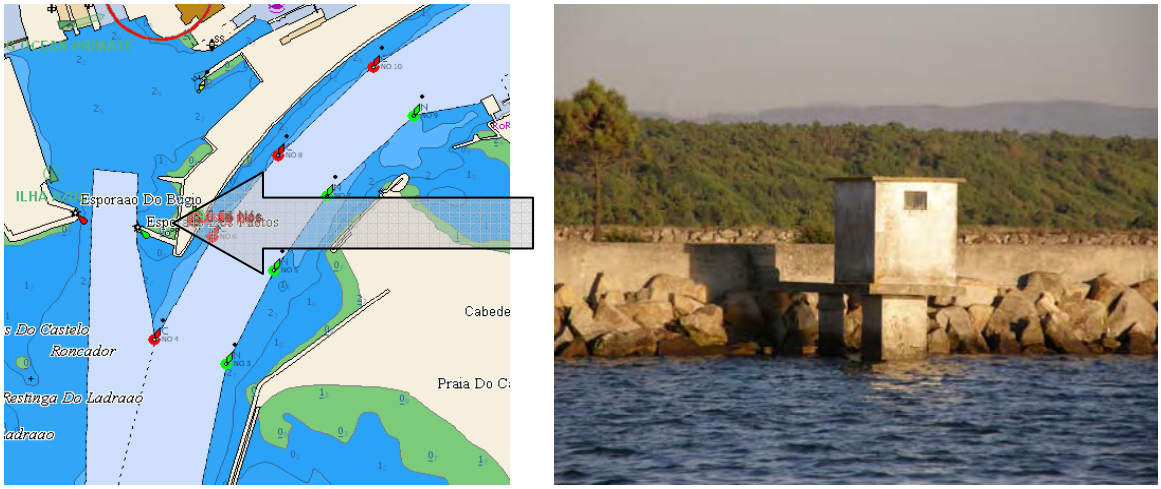

Fig. 47. Tidal gauge location.

This tidal gauge, kept by Instituto Hidrográfico (Portuguese Hydrographic Institute) is located at Latitude 41° 41.17’ N Longitude 008° 50.35’ W, on the northern side of the “Esporão dos Pilotos” breakwater (Fig. 47). This tidal gauge consists of a stilling well, designed to admit only low-frequency oscillations in the water level inside, thus enabling to avoid shorter period waves like seiches and boat wakes. This is particularly important since the tidal gauge is installed on a semi-enclosed bay with heavy fishing boat traffic nearby.

The tidal data, consisting of 8760 records for free surface elevation (representing 365 days of hourly measurements), was analyzed using T_Tide package [Pawlowicz *et al.*, 2002].
The results obtained allow for a detailed analysis of the six primary tidal constituents, in this case, M_2, S_2, N_2, K_2, K_1 and O_1, whose amplitudes and phases are as follows (Table 5):

Name	Tidal Species	Amplitude (m)	Phase (º)	*Period* (h)*
M_2	Principal Lunar	1.0448	77.16	*12.4206*
S_2	Principal Solar	0.3650	105.75	*12.0000*
N_2	Lunar Elliptic	0.2238	59.08	*12.6584*
K_2	Lunisolar	0.1027	101.95	*11.9673*
K_1	Lunisolar	0.0712	61.67	*23.9344*
O_1	Principal Lunar	0.0622	320.84	*25.8194*

* Period of constituents [Stewart, 2005]
Clear constituents - semidiurnal
Shaded constituents - diurnal

Table 5. Primary tidal constituents.

From the above values of harmonic constituents it is clearly seen the predominance of the semidiurnal amplitudes, namely the M_2 constituent which is the most important for the port of Viana do Castelo. In fact its amplitude is about three times the next higher value, the Principal Solar S_2, which, however, has a slightly greater influence than the ellipticity of the moon orbit, as given by N_2 (Fig.48). The small diurnal amplitudes result in relatively small diurnal inequalities of consecutive HW and LW (Fig. 49).

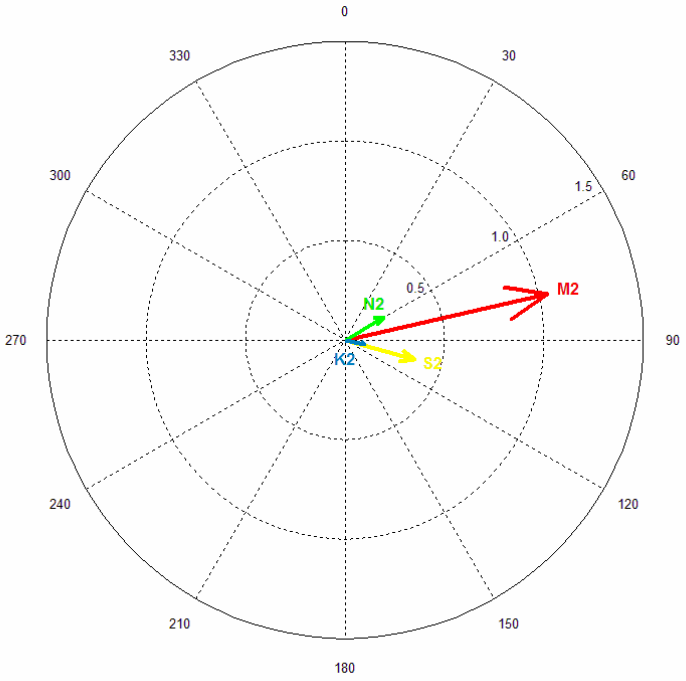

Fig. 48. Graphical plot of semidiurnal harmonic constituents showing the relative importance of M_2.

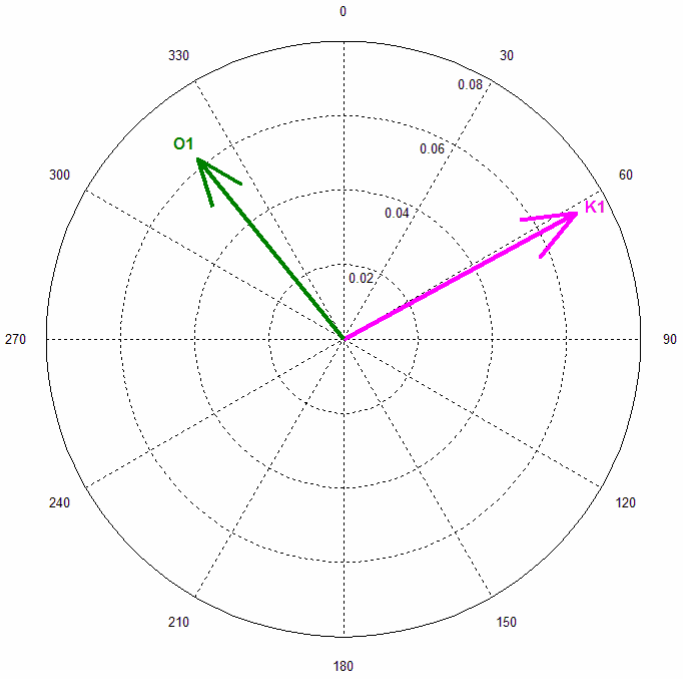

Fig. 49. Graphical plot showing the diurnal constituents which, by comparison with the previous plot, have much smaller amplitudes (the plots have different scales).

The relative importance of the shallow water constituents and the fortnightly constituents was also examined:

Name	Shallow Water	Amplitude (m)	Phase (º)
M_4	Shallow water overtide of principal lunar constituent	0.0075	215.75
M_6	Shallow water overtides of principal lunar constituent	0.0018	151.57
MK_3	Shallow water terdiurnal	0.0011	318.50
S_4	Shallow water overtides of principal solar constituent	0.0008	15.67
MN_4	Shallow water quarter diurnal constituent	0.0035	169.54
MS_4	Shallow water quarter diurnal constituent	0.0038	303.09
M_8	Shallow water eighth diurnal constituent	0.0002	217.35
Name	Fortnightly	Amplitude (m)	Phase (º)
MSF	Lunisolar synodic fortnightly constituent	0.0184	90.44
MF	Lunisolar fortnightly constituent	0.0141	232.98

Table 6. Shallow water and fortnightly constituents.

From Table 6 it is noticeable the low relative importance of the shallow water constituents as it would be expected, since the tidal gauge although standing on a shallow water location, is close to the port entrance thus hindering the bottom friction effect. In contrast, the fortnightly constituents though relatively small compared to diurnal and semidiurnal constituents, have an amplitude of about twice the amplitude of the largest shallow water constituent.

It is important to stress that the harmonic constituents are not a function of time and so are typical for each harbour, constituting, in this way, the fundamental basis for the characterization of the tide in a given place, as well as being the main responsible for good quality predictions [Martins *et al.*, 2004].

The semidiurnal characterization of the tide is also evident from the tidal form number, F, defined as [Pugh, 1987]:

$$F = \frac{K_1 + O_1}{M_2 + S_2}$$

With K_1, O_1, M_2 and S_2 being the amplitudes in meters of the corresponding constituents. $F < 0.25$ results in semidiurnal tides while $F > 3.0$ results in diurnal tides.

For $0.25 < F < 1.5$ the tides are mixed, mainly semidiurnal while for $1.5 < F < 3.0$ the tides are mixed, mainly diurnal. Taking into account the values obtained in Table 5 for Viana do Castelo (tidal gauge location):

$F = (0.0712+0.0622)/(1.0448+0.3650)$

$F = 0.09$

Describing, by this way, semidiurnal tide.

The spectral analysis performed to a one year long sea surface elevation time series (Fig. 50) clearly shows two peaks that correspond to the semidiurnal constituents frequencies (larger) and diurnal frequencies (smaller).

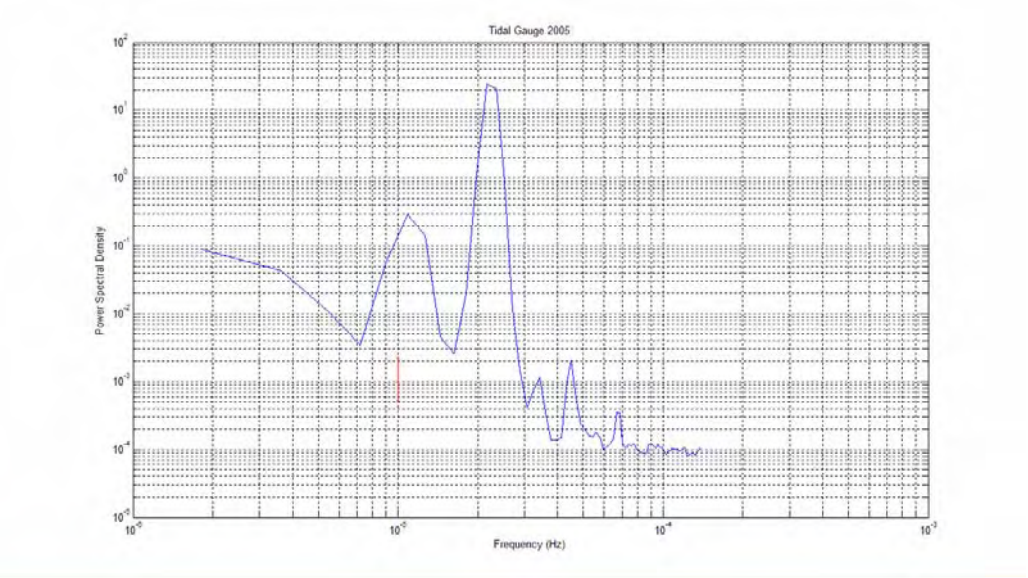

Fig. 50. Spectral analysis to a one year SSE time series for the tidal gauge

In Fig. 51 the sea surface elevation time series for the first 15 days of March 2005 is represented. The analysis of this figure reveals a strong fortnightly tidal modulation, showing the importance of the neap tide/spring tide cycle in the tidal dynamics of the port of Viana do Castelo. A chart datum level of 2.16 m, obtained from the harmonic analysis performed, was used throughout this study.

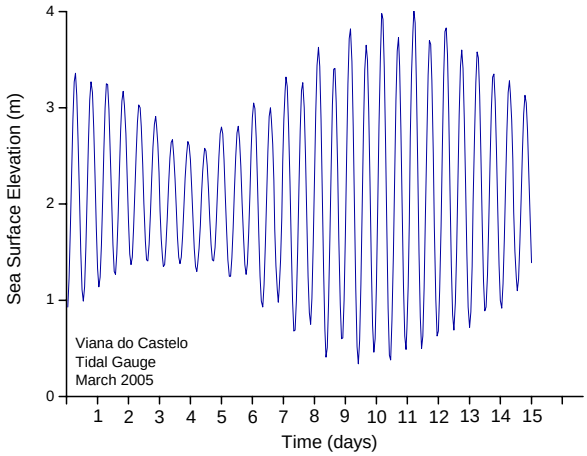

Fig. 51. Tidal sinusoidal for Viana do Castelo

It is also noticeable a higher than normal spring tide in March as well as in September (not shown). These are referred to as equinoctial tides, when the declinations of Moon and Sun are both zero, meaning that the semidiurnal luni-solar tide-raising force will be at its maximum.

Nevertheless the extreme values recorded (4.01 m at HW on 12th of March) are above the HAT (Highest Astronomical Tide) described for this port by Instituto Hidrográfico (3.90 m), which may indicate the occurrence of lower than normal atmospheric pressure or other unusual meteorological event.

These differences between predicted and recorded levels are also inherent to the determination of the Mean Sea Level. One of the causes for these systematic differences is the fact that the tide forecasts published by the Portuguese Hydrographic Institute are referred to the chart datum level ("Zero Hidrográfico"), in the vicinity of the Lowest Astronomical Tide, although the legal reference level is the "NMA – Nível Médio Adoptado" or Adopted Mean Level, which corresponds to the mean sea level at Cascais as determined by over 50 years of tidal data centred in 1910 (1883-1938). This level was transposed for all the country by the Geographic Portuguese Institute and still constitutes the legal base for all positive or negative heights [Martins *et al.*, 2007]. Due to this, and also to the global observed sea level rise through thermal expansion of sea water and widespread loss of land ice [IPCC, 2001] the height values of the tidal forecasts published by the Portuguese Hydrographic Institute are generally lower than the observed real values.

4. Numerical Modelling Study of the Lima Estuary

4.1. The Hydrodynamic Model

There is a significant increase worldwide in the use of numerical methods as a tool for simulating tide related processes as well as pollutant transport. The ever increasing computational capabilities allow for its widespread use in hydraulic and environmental engineering.

Taking into account the characteristics of the study area (partially mixed estuary) and the processes to be studied (tidal/long wave propagation) a vertically integrated bi-dimensional hydrodynamic numerical model (SIMSYS2D) [Leendertse and Gritton, 1971; Leendertse, 1987; Dias, 2001] was considered adequate.

The two types of numerical models that are most commonly used to solve the two-dimensional depth-integrated (2DH) shallow water equations are the finite difference method and the finite element method.

Although the finite element method has the advantage of handling more efficiently complex land boundaries through the ability of representing complex geometry using an unstructured mesh (grid) [French *et al.*, 2000], the finite difference method is very effective in dealing with the non-linear advective terms in the shallow water equations [Lin, 1996] which may cause serious stability problems, although having the disadvantage of treating the boundary conditions in an approximate way since the curvilinear layout of the land boundaries will be treated in a rectilinear way.

The SIMSYS2D model solves the vertically averaged equations of long wave motion discretized through the application of the finite

difference method over a rectilinear grid using a space-staggered scheme.

On this model, an Alternating Direction Implicit (ADI) method is used to solve these equations.

The effects of freshwater river flow, tides, wind, rotation of the earth and bottom friction are simulated. It is applicable to bodies of water whose depths, though varying, are shallow compared with their horizontal dimensions [Leendertse, 1987].

Thus, the second order partial differential equations for depth averaged fluid flow (shallow water equations) can be derived from the full three dimensional Navier-Stokes equations if the hydrostatic assumption (vertical acceleration and velocity are assumed to be small in simulating long waves) and the Boussinesq assumption (density differences are negligible) are made.

After the simplifications and assumptions, the system consists in one equation for the mass continuity and two horizontal momentum equations that are vertically averaged by integrating from the bottom to the surface:

$$\frac{\partial \zeta}{\partial t} + \frac{\partial [(h+\zeta)U]}{\partial x} + \frac{\partial [(h+\zeta)V]}{\partial y} = 0 \qquad (1)$$

$$\frac{\partial U}{\partial t} + U\frac{\partial U}{\partial x} + V\frac{\partial U}{\partial y} = fV - g\frac{\partial \zeta}{\partial x} - \frac{\tau_x^b}{(h+\zeta)\rho} + A_h \nabla^2 U \qquad (2)$$

$$\frac{\partial V}{\partial t} + U\frac{\partial V}{\partial x} + V\frac{\partial V}{\partial y} = -fU - g\frac{\partial \zeta}{\partial y} - \frac{\tau_y^b}{(h+\zeta)\rho} + A_h \nabla^2 V \qquad (3)$$

Where U is the depth integrated velocity component in the x (eastward) direction, V is the depth integrated velocity

components in the y (northward) direction, ζ is the surface water elevation, h is the water depth, t is the time, f is the Coriolis parameter, g is the acceleration of gravity, ρ is the water density, A_h is the cinematic constant turbulent horizontal viscosity and τ^b is the magnitude of the shear stress on the bottom.

The bottom stress is assumed proportional to the square of the horizontal velocity [Leendertse and Gritton, 1971]:

$$\tau_x^b = \rho_0 g \frac{U(U^2+V^2)^{\frac{1}{2}}}{C^2} \quad \text{and} \quad \tau_y^b = \rho_0 g \frac{V(U^2+V^2)^{\frac{1}{2}}}{C^2} \qquad (4)$$

Where C is the Chézy coefficient. This coefficient depends on the bottom roughness and composition and on the height of the water column.

The Chézy coefficient was determined from the Manning roughness coefficient, n [Chow, 1959]:

$$C = \frac{\sqrt[6]{h+\zeta}}{n} \qquad (5)$$

The system of equations was discretized using a finite difference method and is solved by implicit finite difference techniques, with the variables defined on a space-staggered rectangular grid [Leendertse and Gritton, 1971]. A “fractioned-step” technique combined with an Alternating Direction Implicit (ADI) algorithm is used in the solution of the difference equations to avoid the necessity for iteration.

In order to ensure second order accuracy the variables were defined as follows: the water levels ζ (“**+**” on the grid) are

computed at integer values of the grid, the Chézy values are computed at the same locations, whereas the depths values h ("**O**" on the grid) are given at half-integer values of the grid, the velocity components are situated between the locations of the water levels (the u velocity components ("**-**" on the grid) are computed at half-integer values of x (j) and integer values of y (k), and the velocities v ("**|**" on the grid) are computed at half-integer values of y (k) and integer values of x (j) (Fig. 52).

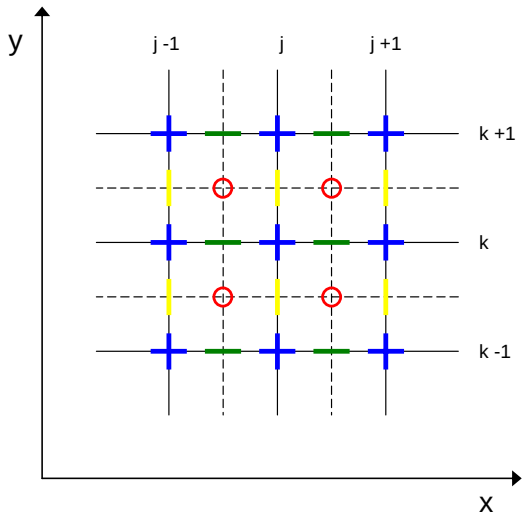

Fig. 52. Location of variables on the grid [Leendertse, 1987].

The ADI algorithm implies that at each time step a solution is first made in the x-momentum equations followed by a similar solution in the y-direction. The application of the implicit finite scheme results in a tridiagonal system of equations for each grid line in the model. The solution is obtained by inverting the tridiagonal matrix using the Double Sweep algorithms, a very fast and accurate form of Gauss elimination. The implicit scheme is used in such a way that stability problems do not occur provided that the input data is physically reasonable, so that the time step used in the computations is limited only by accuracy requirements.

With appropriate boundary and initial conditions, this system of equations constitutes a well-posed initial boundary value problem whose solution describes the depth-averaged circulation in a tidal basin. For barotropic models driven by tidal forcing the boundary conditions from experimental data include both the reflected and the incident waves, therefore and by its simplicity, extrapolation formulas are adopted at the open boundaries in this model [Dias and Sousa, 2007].

4.2. Construction of the Bathymetry

The data for the construction of the numerical bathymetry inside the port area was collected from hydrographic surveys carried out by Hidrodata, the company contracted by port authority to perform periodic surveys inside the port and on the approaches.

The following surveys were used:

Hydrographic Survey 0255-ARN-1002, October 2002.
(Main port area)
Hydrographic Survey 0286-ARN-0503A, May 2003.
(Approaches to port entrance)
Hydrographic Survey 0330-ARN-1203/A, December 2003.
(Area between bridges)

These surveys have the coordinates referred to the Army Geographic Institute, Lisbon datum, with depths related to Chart Datum (approximately the lowest level due to astronomical effects and excluding meteorological effects) and offer an excellent resolution of about 5 (five) meters.

Since the bathymetric data available provided a good resolution it was decided to use it to define the land/water interface, thus digitalization was not considered.

The initial model grid inside the port was achieved by use of a Fortran program [Dias, 2001] which defines the required water depth at the grid points, based on an algorithm which principle is to guarantee conservation of water volume at each cell, thus assuring the same value in the numerical and real bathymetry. The determination of the water volume at each cell was accomplished using a Monte Carlo cubature method [Dias, 2001].

On the outer area of the port, depths were obtained from Portuguese Hydrographic Institute Nautical Chart nº 26401 (INT

1870) again with soundings in meters above Chart Datum. The limits for the study area were defined to the West by the meridian 008º51.8’W, to the North by parallel 41º41.5’N and to the South by parallel 41º39.3’N. The Eastern limits (outside the port) were defined by the shoreline.

From this chart, soundings were taken as geographic coordinates (Lat/Lon) referred to European Datum 1950 and then converted to rectangular military coordinates (Lisbon Datum).
Since nautical charts are to be used for navigation purposes the soundings are irregularly spaced, averaging, on this case, between 100m and 200m. Thus it was necessary to use an interpolation method to produce the required grid. The Kriging method was chosen due to its inherent reliability for the mentioned area.

Kriging is a geostatistical gridding method that produces bathymetry from irregularly spaced data [Cressie, 1990]. In this work, Kriging was used to express the trends suggested in the irregularly spaced input soundings and to deliver an interpolated 40m by 40m grid by estimating the values of the points at the grid nodes.

After completion of this interpolation technique the results were visually compared to the isobathymetric lines on the nautical chart, resulting on a good match and providing a realistic bathymetric structure.
Given that an accurate bathymetric representation is one of the most important and fundamental requirements in successful modelling [Cheng *et al*., 1991], it was clear from the beginning that time and effort applied on the bathymetric representation would prove extremely useful at later stages of the work. The initial file consisted of 112385 sounding points, a large value for a relative small area under study.

In fact, the construction of the final bathymetry, given the data processing and interpolation techniques used (Monte Carlo inside

the port area and Kriging on the outside), the coordinates conversion task and the final subtle refinements to the grid, proved to be one of the most demanding and time-consuming works within the scope of this study.

The model grid must be sufficiently refined to resolve the essential features of the depth and the geometry variations [Dias *et al.*, 2006]. Because a port area was under study, a cell dimension of 20m was firstly considered adequate to try to understand hydrodynamic phenomena in relative small areas and also taking into consideration that a finer resolution would significantly increase the computation time.

Nevertheless, on the first test runs of the model it was clear that such a fine resolution was creating program instabilities derived from the small cell dimensions, even though a broad set of time steps were tried out. Thus it was decided to adopt a 40m by 40m cell dimension that, with no important loss of definition, would make the model much more reliable and, at the same time, significantly decrease the computation time.

This resulted in 160 cells in the x-direction (eastward) and 100 cells in the y-direction (northward), corresponding to 6400 m and 4000 m respectively.

Although the area of interest of this study is mainly the commercial harbour, care was taken to place the boundaries as far as practicable, so that when studying changes in the physical system, the results remain as independent as possible of those defined at the boundaries, *i.e.*, sea surface elevation at the West boundary and river flow at the East boundary.

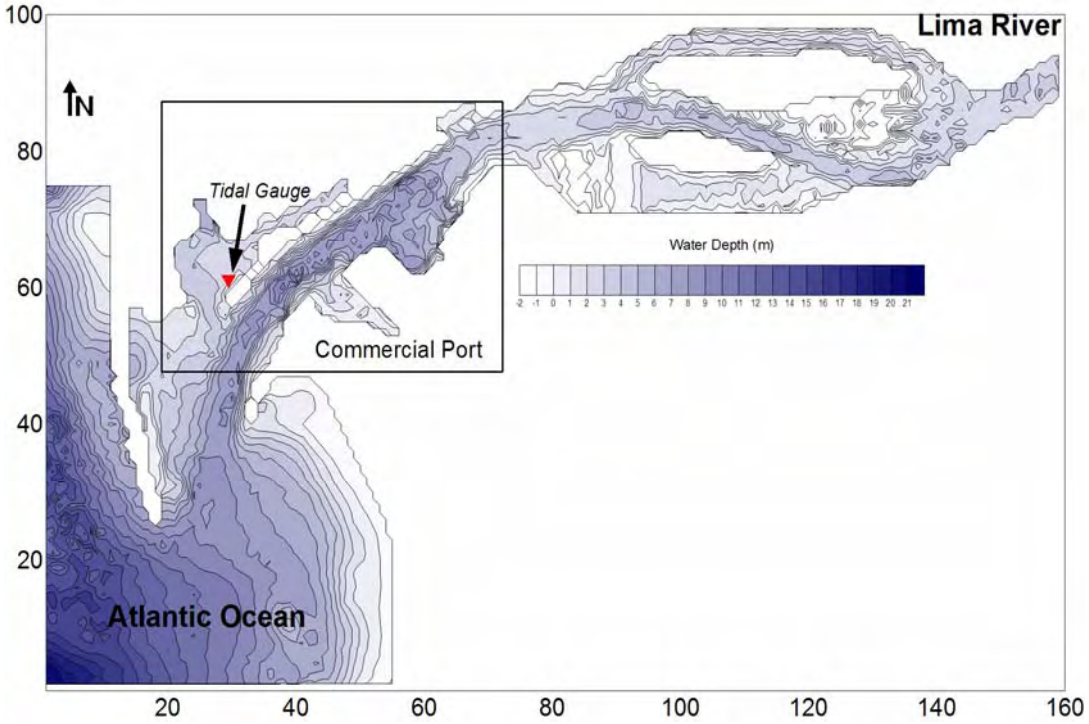

Fig. 53. Initial model grid.

Fig. 54. Overlapping of model grid with aerial view.

4.3. Model Parameterization

The model was implemented taking into account a rectangular grid with 160 X 100 cells in the *x* and *y* direction respectively, each square cell measuring 40 meters on the side.

The West open boundary was open between cells 2 and 75 (column 1) and forced with 34 days tidal elevations, comprising 3 days for the spin up period and a one month tidal time series (March 2005) with elevations for each minute, supplied by the Ocean Modelling Group, Aveiro University, by the use of XTIDE software with data from tidal modelling using ROMS, Regional Ocean Modelling System, forced by TPXO, OSU TOPEX/Poseidon Global Inverse Solution [Marta-Almeida and Dubert, 2006]. This set of data incorporates only the astronomic tide.

Since the West open boundary was placed offshore, the use of tidal data that takes into account the details of the adjustment of the tidal wave in the shelf region of the Western Iberian Peninsula was considered adequate.

The East open boundary was open between cells 88 and 94 (column 160) and forced with a constant river flow of 50 m^3s^{-1} which corresponds to a velocity horizontal component of 0.07 ms^{-1} considering the 280 metres width of the river at the boundary and an average depth of 2.5 m

Along the solid boundaries a null normal velocity was imposed and a free slip condition was assumed while the initial conditions were horizontal level and null velocity in all the grid points.

At this stage, minor subtle corrections to the computer generated grid were introduced manually, namely the appropriate alignment of the commercial port berths and the introduction of a “land” cell in the middle of the channel to replicate the effect of the seven pillars of the Eiffel bridge.

Values of 1026 kg/m^3 and 9.81 m/s^2 were established for the water density and gravitational acceleration, respectively, while 20 s were chosen for the computational time step and 20 m^2s^{-1} for the horizontal viscosity coefficient. On the first test runs it was found that horizontal viscosity had a minor influence on the model behavior.

Given the small area under study and the estuary alignment relating to the prevailing winds (perpendicular) it was considered not to include wind stress in the simulations, as this would artificially influence the model results since at Viana do Castelo rarely the wind blows steadily and continuously from the same quadrant.

4.4. Hydrodynamic Model Calibration

Before being considered adequate for the intended purpose, the hydrodynamic model must be calibrated and validated. Ideally, models should be created based on a profound knowledge of all the field data of the system to be reproduced, allowing for an accurate parameterization of all the values during model implementation. This is hardly ever achieved due to lack of proper number of field observations, shortness of available time series or large number of parameters to be considered. The approximations and parameterizations used for the synthesis of the model will inevitably lead to discrepancies and deviations of the model results from nature [Sousa and Dias, 2007]. This is why model calibration becomes essential, by assuring a *certain* degree of fit between model results and field observations. Therefore, calibration focuses on the comparison between model results and field observations [STOWA/RIZA, 1999].

Although there are no standard procedures for model calibration, typically, the calibration is accomplished by qualitative comparison of short time series of water level or velocity produced by the numerical model with field data for the same location and period of time [Cheng *et al.,* 1991].

Within the scope of this work it was decided to carry out a qualitative calibration by adjusting the model and directly comparing simulated and observed sea surface elevation for stations B, H and I (tidal gauge, navigation buoy #11 and navigation buoy #9, respectively, referred to in Table 8). For station B, a 31 days sea surface elevation time series was considered (March 2005) and for stations H and I a complete tidal cycle was analyzed (26th and 27th June 2007).

A quantitative assessment with the intention of evaluating the model performance was also completed, using RMAE, RMS and Skill methods for the longer time series and RMS and Skill for the

shorter ones. Harmonic analysis was also set for a 31 days time series (March 2005) from both modeled and observed values in order to quantify differences.

It is a known fact that, in most estuarine systems, sea level observations reveal tidal energy damping, due to friction, as the tidal wave propagates upstream [Hsu *et al.*, 1999]. One typical example of this behavior can be found in Ria de Aveiro, Portugal [Dias, 2001] and [Dias and Fernandes, 2006]. The magnitude of the bottom friction coefficient determines changes in the tidal wave propagation within the lagoon [Vaz *et al.*, 2007] and its value depends for the most part on water depth, bottom sediments, vegetative cover and flow conditions.

The Manning's roughness, or bottom friction coefficient, is therefore the most commonly used parameter to be adjusted in the Manning-Chézy formulation for the bottom stress (equations 4 and 5) in the calibration process of the hydrodynamic model. In this work, other model parameters such as the horizontal viscosity coefficient or the time step were adjusted during initialization of the model and first test runs.

In order to achieve the best possible fit between model results and observed sea level records, different values of Manning's *n* coefficient were tried, taking into account the available previous studies for Ria de Aveiro, Portugal [Dias and Lopes, 2006], Atchafalaya River Delta, Louisiana, EUA, [Donnell *et al.*, 1991] and Patos Lagoon, Brazil [Martins *et al.*, 2007]. In all these studies, the Manning's coefficient *n* was varied as a function of water depth, as a supplement to the Manning-Chézy formulation.

Several simulations were performed with diverse values of *n*, although with no outstanding differences on the model results. Nevertheless, the best possible adjustment to the tidal gauge records and data gathered from stations I and H was attained with

n values ranging between 0.015 and 0.020, depending on the water depth (Table 7).

Depth (m)	Manning's *n* value ($s/m^{1/3}$)
<3	0.020
3-10	0.018
>10	0.015

Table 7. Manning's n coefficient for a given depth.

No particular method was followed in this process but to judge the discrepancies on each simulation and then re-run the model as many times as necessary, finishing when the best possible fit between model results and observations was achieved.

The necessity of gathering field data, other than the tidal gauge records, arose from the sense that using a single station for calibration would entail the risk of the model not being considered fit for reproducing the tidal phenomena throughout the domain. It was thus decided to collect sea level field data time series for two more stations, even if, due to logistic difficulties, short in period. The process is described below.

Within the frame of this work, on the 26th and 27th of June 2007 a measurement instrument was deployed close to navigation buoys #11 (Station H) and #9 (Station I), respectively, for a complete tidal cycle each day (Fig. 55).

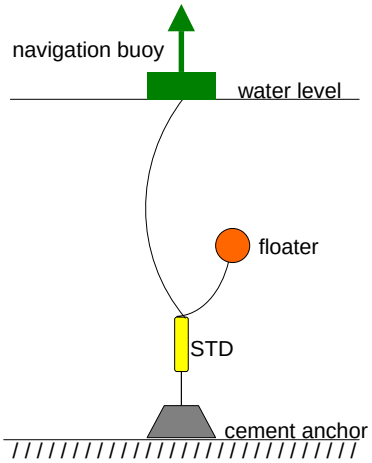

Fig. 55. STD mooring arrangement.

The instrument, a MINI STD model SD204, is equipped with permanent sensors for conductivity, temperature and pressure. The purpose of its use was the determination of the sea surface elevation by making use of the pressure sensor. This sensor, of a piezoresistive type, is based on a Keller PA9 absolute pressure sensor element. It measures the absolute pressure *i.e.* the atmospheric pressure plus the water pressure with a resolution of 0.05m and an accuracy of +/- 0.10m [MINI STD Operating Manual]. The atmospheric pressure is deducted from the total value since the first reading is taken outside the water.

The STD was set for a 10 minute sampling interval and positioned in the water column with a mooring arrangement consisting of a cement anchor on the river bottom, a line attached to the mooring bar shackles and a float enabling a vertical positioning of the device about 2 meters above the bottom due to the float's buoyancy. The recovery line was attached to the navigation buoys.

Fig 56. Location of calibration stations.

On the 26th the STD was placed in position 41º41.42'N 008º49.39'W (Station H) at 06h50m (UTC) with the first reading recorded at 06h58m (about 68 minutes after the morning Low Water). The device was recovered at 20h30m with the last significant reading recorded

at 20h18m (about 122 minutes after the afternoon Low Water). The processed data is shown in Fig.57.

The meteorological conditions during the sampling were fair with clear skies, an average pressure of 1023 hPa and a 25 knots North-Northwesterly wind.

The obtained values have no reference to the chart datum since the device measures the water column above it, by way of the respective pressure.

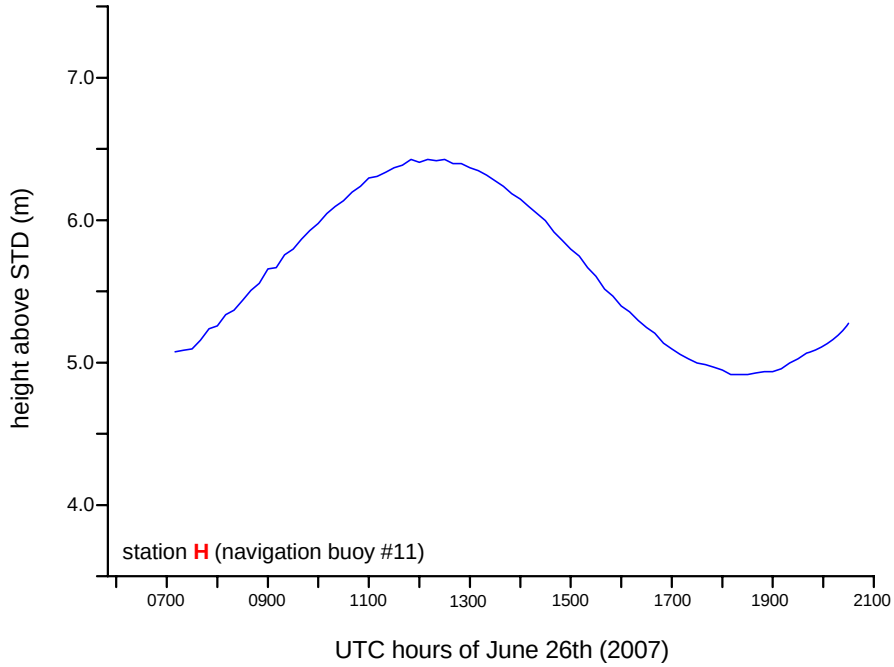

Fig. 57. Station H, STD readings.

On the 27th the STD was placed in position 41º41.17'N 008º49.94'W (Station I) at 06h44m (UTC) with the first reading recorded at 06h53m (about 16 minutes after the morning Low Water). The device was recovered at 20h20m with the last significant reading recorded at 20h13m (about 69 minutes after the afternoon Low Water). The processed data is shown in Fig. 58.

The meteorological conditions during the sampling were fair with clear skies and an average pressure of 1022 hPa. The wind increased to about 30 knots North-Northwesterly, mainly during the afternoon.

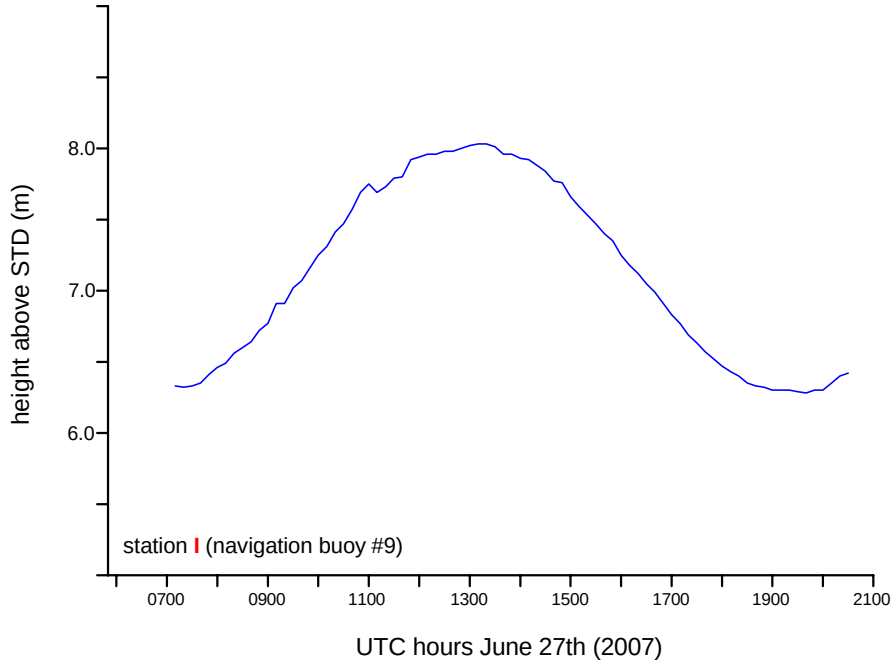

Fig. 58. Station I, STD readings.

Although limited to about one tidal cycle each day, these readings were used to enhance the overall quality of the calibration process.

Thus, for calibration purposes, it was decided to run the model, forcing with a one month tidal time series with elevations for each minute, supplied by the Ocean Modelling Group, Aveiro University, by the use of XTIDE software with data from tidal modelling using ROMS, Regional Ocean Modelling System, forced by TPXO, OSU TOPEX/Poseidon Global Inverse Solution [Marta-Almeida and Dubert, 2006] for the 30 days of June 2007 as the ocean boundary condition and a steady river flow of 50 m^3s^{-1} at the East open boundary. Several simulations were performed adjusting the values of the bottom friction coefficients for a best fit between

model results and observed values. Since the time period was different for stations H/I and B, it was necessary to run the model in parallel for both conditions until the best results were achieved for all three stations, resulting in the Manning's *n* values described on Table 7.

For stations H and I two virtual stations were introduced to the model in the positions matching the ones where the STD was deployed (Table 8 and Fig. 56):

Station		Coordinates				Z_0
ID	Location	x	y	LAT(N)	LON(W)	
B	tidal gauge	31	62	41º41.2'	008º50.4'	1.50
H	navigation buoy #11	43	62	41º41.42'	008º49.39'	7.12
I	navigation buoy #9	61	74	41º41.17'	008º49.94'	6.60

Table 8. Coordinates of 3 stations used for calibration

Since the STD readings are related to the water pressure *i.e.,* the weight of the water column above the device positioning, there is no reference datum to relate to. The data must be adjusted in order to be comparable to the model data output.

In this case, the differences between pre-processed STD readings and related model output data were averaged and the resulting value subtracted to the initial readings (Figs. 59 and 60). This procedure has inherent uncertainties but was considered adequate to establish the reliability of the model results to the referenced stations.

The obtained results are presented below:

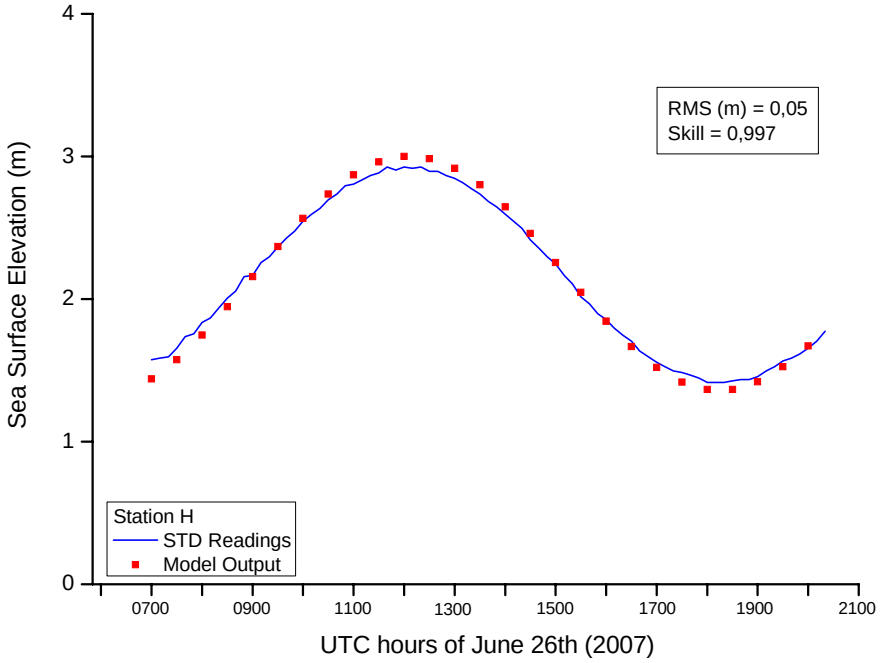

Fig 59. Comparison between STD readings and model output after calibration for station H

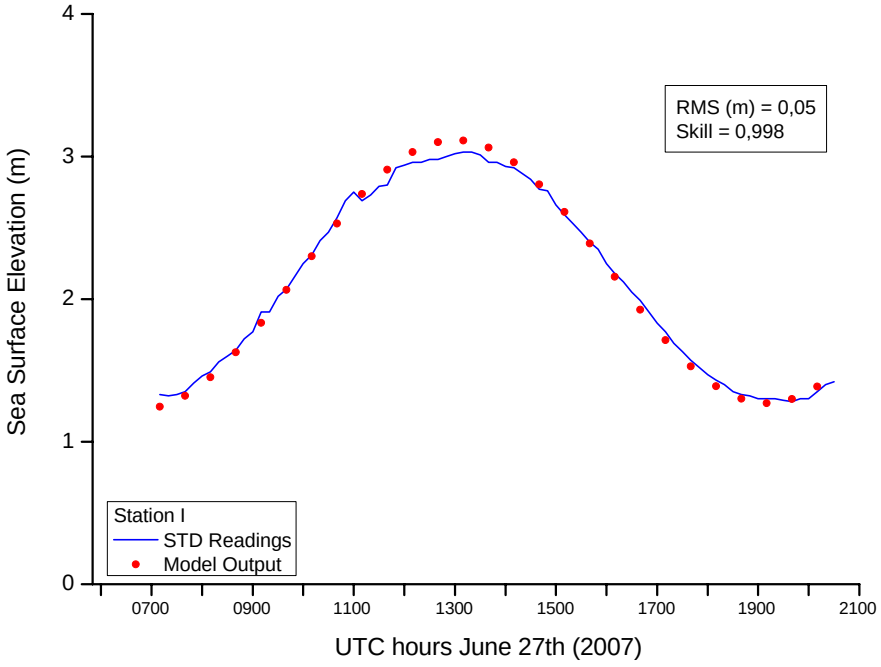

Fig 60. Comparison between STD readings and model output after calibration for station I

Both plots show a good agreement between modeled and observed sea level elevation, although the short period of time of the field data must be taken into account.

For station B (tidal gauge), during the calibration process, the model was run using a one month water level time series, although for better visualization, shorter periods of time were used, as can be found in Fig.62 and Fig.63, where the best fit is shown.

The model was forced with the ROMS tidal data for 34 days, comprising 31 days of March 2005 and 3 days allowed for the spin up period.

All model parameters remained the same during the calibration process, except the time period of the input tide, which is different for the tidal gauge data and the collected field data for stations H and I.

Data from station B (tidal gauge) was filtered for low and high frequencies in order to separate the meteorological effects from the astronomic tide (Fig. 61), with the filtering parameters defined before, on the storm surge analysis.

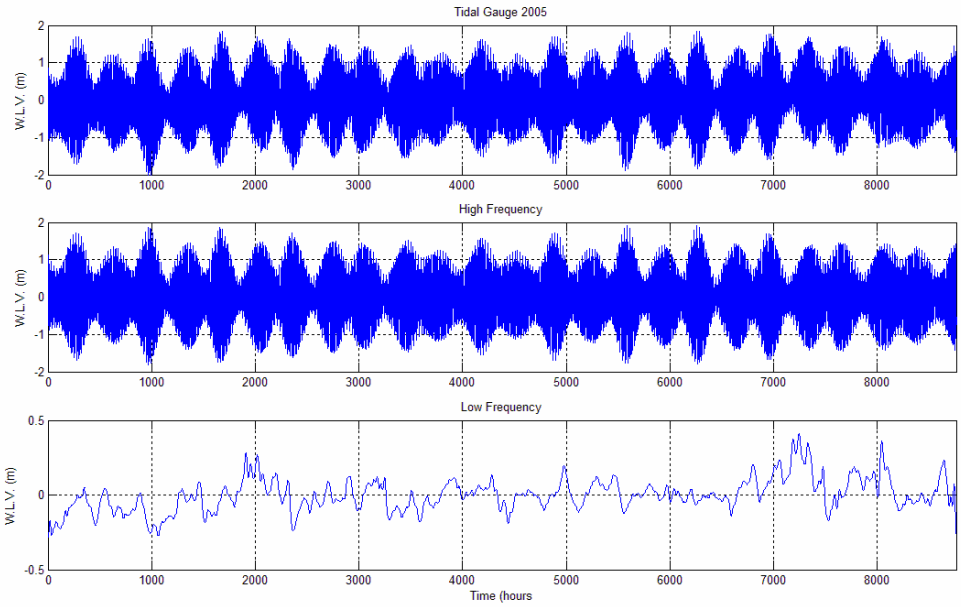

Fig. 61. Total tide, astronomic tide only and meteorological effects removed.

The comparison of model results and filtered data from station B (tidal gauge) is shown in Fig. 62 and Fig. 63.

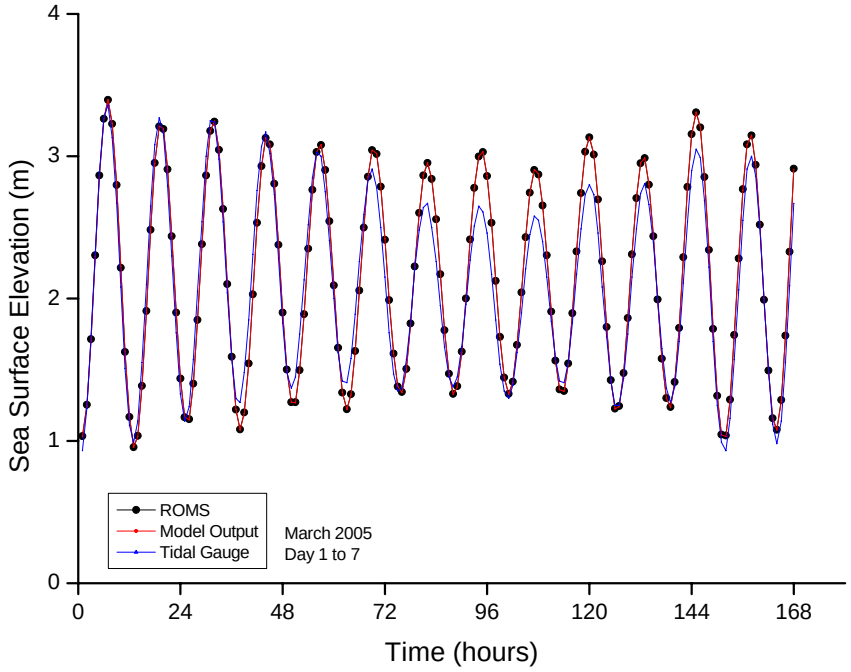

Fig. 62. Comparison between tidal gauge records and model output (station B), for 7 days.

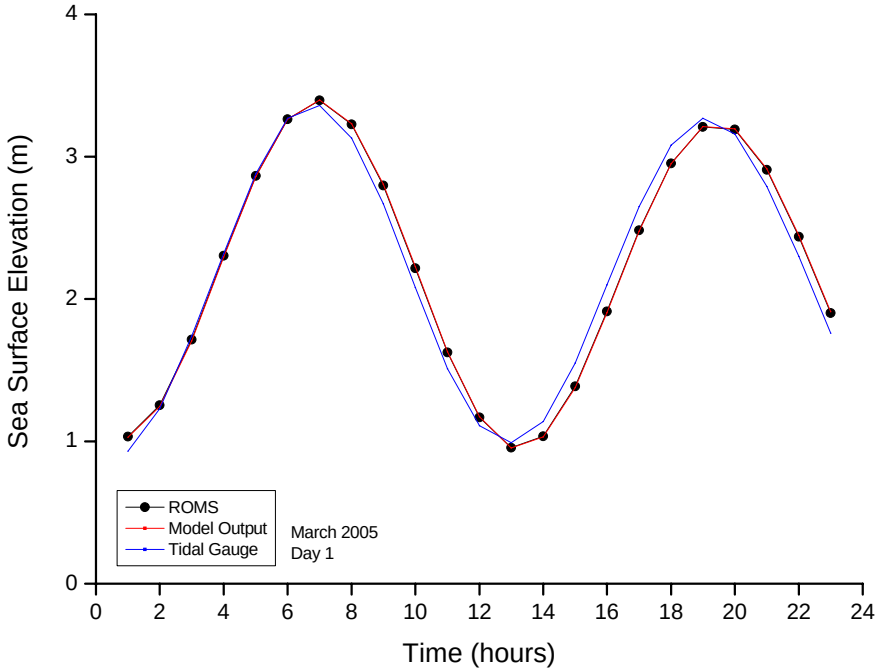

Fig. 63. Comparison between tidal gauge records and model output (station B), for 24 hours.

After the qualitative comparison between model results and observations, a quantitative approach was found necessary to evaluate the model performance for all stations considered. Recent studies from different authors suggest the use of different methods or the simultaneous use of different methods. Hydrodynamic modelling of Patos Lagoon [Fernandes *et al.*, 2002] was evaluated through the use of the Relative Mean Absolute Error (RMAE), Ria de Aveiro modelling studies [Dias and Lopes, 2006] used the Root Mean Square (RMS), while predictive Skill was used to assess the numerical modelling of the Hudson River Estuary [Warner *et al.*,2005]. More recently, numerical model results were evaluated using all the three previously mentioned methods [Sousa and Dias, 2007] and [Martins *et al.*, 2007].

In the present work, the quantitative agreement between model and observations is evaluated through the determination of these three parameters, RMAE, RMS and Skill, although for stations H and I the use of RMAE was not considered adequate because of the averaging process of the STD readings.

The RMAE, Root Mean Absolute Error, was defined as [Walstra *et al.*, 2001]:

$$RMAE = \frac{\left\| \zeta mod \right| - \left| \zeta obs \right\|}{\left| \zeta mod \right|} \qquad (6)$$

where ζmod and ζobs are the averages of the predicted and observed sea surface elevations, respectively. The qualification for RMAE ranges suggested by Walstra is presented in Table 9 below:

Qualification	RMAE
Excellent	<0.2
Good	0.2-0.4
Reasonable	0.4-0.7
Poor	0.7-1.0
Bad	>1.0

Table 9. RMAE ranges qualification

The calculated value of RMAE for tidal gauge station, 0.012 m, qualifies as excellent in the above mentioned RMAE ranges. One full month of simulation/observations was taken into account.

The RMS, Root Mean Square, of the difference between the observed and predicted sea surface elevation is defined as:

$$RMS = \left\{ \frac{1}{N_0} \sum_{i=1}^{N_0} [\zeta_{obs}(t_i) - \zeta_{mod}(t_i)]^2 \right\}^{\frac{1}{2}} \qquad (7)$$

and it is the square root of the mean of the square of the differences between observed and simulated values, where $\zeta_{obs}(t)$ is the observed and $\zeta_{\mathrm{mod}}(t)$ the simulated sea surface elevation and N is the number of measurements in the time series. The computed value of RMS for one month time series was found to be 0.147 m for station B, 0.055 m for station H and 0.053 m for station I.

Predictive Skill is based on quantitative agreement between model and observations [Warner *et al.*, 2005] and is defined:

$$Skill = 1 - \frac{\sum |\zeta_{mod} - \zeta_{obs}|^2}{\sum \left(|\zeta_{mod} - \overline{\zeta_{obs}}| + |\zeta_{obs} - \overline{\zeta_{obs}}| \right)^2} \qquad (8)$$

where ζ is the variable being compared with a time mean $\overline{\zeta}$ (in this case, sea surface elevation). Perfect agreement between model results and observations will yield a skill of one and complete disagreement yields a skill of zero. The computed value of skill for the tidal gauge station was found to be 0.992 while stations H and I showed values of 0.997 and 0.998 respectively.

Table 10 presents the summary of the computed values:

Station	Location	RMAE (m)	RMS (m)	SKILL
B	Tidal Gauge	0.012	0.147	0.992
H	Buoy #11	-	0.055	0.997
I	Buoy #9	-	0.053	0.998

Table 10. Summary of RMAE, RMS and SKILL for stations B, H and I

It is worth analysing the results from the quantitative assessment performed. According to the results presented in Table 10, the model reproduction may be considered very good, for the referred stations, with a RMAE of 0.012 m for station B and a RMS varying between 0.053 m and 0.147 m. The former value is qualified as “excellent” within the ranges proposed by Walstra (<0.2), while the latter can be considered a reasonable/good value, intrinsic to the uncertainties of the tidal gauge records. In fact the RMS value of 0.147 m corresponds to about 4% of the maximum tidal range for the considered time series and 6% of the mean local tidal range. The calculated values of Skill ranging between 0.992 and 0.998 are apparently good since a perfect agreement would entail a Skill of 1.

Even though the calculated values of Skill show a good agreement between observed and model results it was considered useful to compare these values to other author’s calibration efforts, for the same dynamic processes.

A methodical study was carried out making use of the recent available literature from authors using Skill to quantify hydrodynamic modelling results, resulting in the values presented on Table 11 below.

Author	Skill	Model	Study Área
Warner *et al.*	0.850 – 0.950	ROMS	Hudson River Estuary
McLaughlin *et al.*	0.783 – 0.999	BELLAMY	Great Bay Estuarine System
	0.600 – 0.998	ADAM	
Sousa and Dias	0.921 – 1.000	SIMSYS2D	Ria de Aveiro
Martins *et al.*	0.988 – 0.998	SIMSYS2D	Patos Lagoon

Table 11. Other author's skill assessment

Considering the Skill values presented in Table 11, it is quite clear that a Skill range between 0.992 and 0.998 calculated on this work is within the range of acceptable result values for quantifying model performance as good.

A harmonic analysis assessment was considered suitable as a complementary quantification method of the model accuracy. This method has been used with the previous mentioned purpose in several studies [Sousa and Dias, 2007], [Vaz *et al.*, 2007].

The ROMS tidal data, consisting of 744 records for free surface elevation (representing 31 days of hourly measurements, March 2005) and the corresponding 31 days time series for the model output and tidal gauge records were all analyzed using T_Tide package [Pawlowicz *et al.*, 2002].

The results obtained allow for a detailed analysis of the differences between the five primary tidal constituents, in this case, M_2, S_2, N_2, K_1 and O_1, whose amplitudes and phases are as follows:

		1		2		2-1		3		2-3	
		model forcing		model results		differences		tidal gauge		differences	
		amp (m)	*pha (º)*	*amp (m)*	*pha (º)*	*amp (m)*	*pha (º)*	*amp (m)*	*pha (º)*	*amp (m)*	*pha (º)*
semidiurnal	M_2	1.0680	74.34	1.0708	74.75	0.0028	0.41	1.0549	75.25	0.0159	-0.50
	S_2	0.4109	111.98	0.4120	112.42	0.0011	0.44	0.4998	111.09	-0.0878	1.33
	N_2	0.2150	55.11	0.2155	55.52	0.0005	0.41	0.2192	46.49	-0.0037	9.03
diurnal	K_1	0.0908	79.90	0.0909	80.12	0.0001	0.22	0.0487	63.89	0.0422	16.23
	O_1	0.0554	316.32	0.0555	316.48	0.0001	0.16	0.0641	318.48	-0.0086	-2.00

Table 12. Comparison of harmonic constituents between tidal gauge and model output.

From the obtained model results (see Table 12), it is clear a good match with the model forcing tide and the model results, both in amplitude and phase.

The differences in the amplitude of the diurnal constituents between model forcing tide and model output can be considered negligible while phase differences are under 0.5º for all considered constituents.

The differences between tidal gauge records constituents and the model output also show a good agreement in amplitude and phase. For the M_2 constituent, by far the most important, amplitude difference is 0.016 m while phase diverges 0.50º. For the principal solar constituent, S_2, the amplitude and phase differences are 0.088 m and 1.33º, respectively.

These results are best evaluated if a graphical comparison is performed. With this in mind, plots were prepared and are presented below:

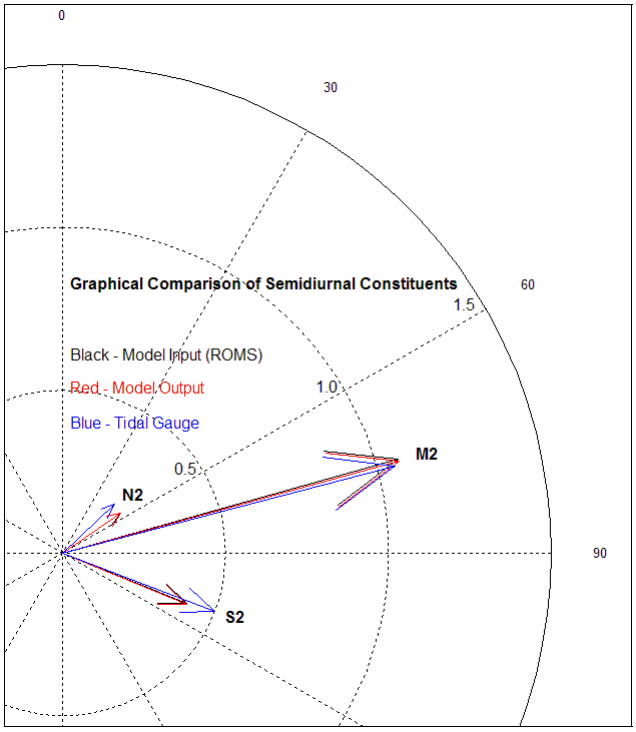

Fig. 64. Graphical comparisob of semidiurnal constituents.

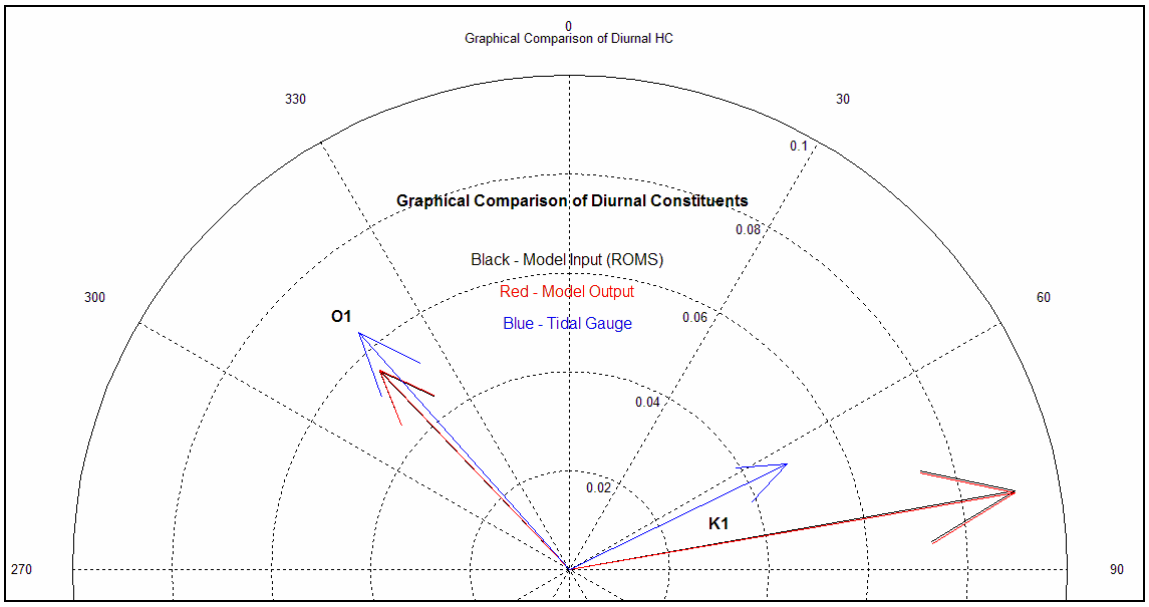

Fig. 65. Graphical comparisob of diurnal constituents.

The graphical comparison enhances the almost coincident harmonic constants from both forcing and modelled tide, as well as a reasonable good match with the tidal gauge harmonic constituents. Although the harmonic constituents are not a function of time and so are typical for each harbour, constituting the fundamental basis for the characterization of the tide in a given place [Martins *et al.,* 2004], it must be stressed that morphologic changes introduced to the estuary by siltation, erosion, dredging activities and port layout development will lead to changes in the tide characteristics. Due to this fact, when harmonic analysis is performed with the aim of calibrating or validating the hydrodynamic model (or for tidal prediction) it must be ensured that recent data is available, or, at least, the data must be subsequent to any major change to the system bathymetry and morphology.

In this work, although very recent long sea surface elevation time series were available (2004 and 2005), the data pertained to the same location, the tidal gauge, hindering the calibration process by harmonic analysis for other stations located on the upper reaches of the study area.

Given the relatively small area under study, where major changes to tidal propagation are not to be expected within the model domain, and considering the adjustment of the modelled tide to the tidal gauge sinusoidal, as well as the good results of the quantitative assessment performed using RMAE, RMS, Skill and the harmonic analysis, it may be considered that the tidal processes occurring at Viana do Castelo harbour are well represented by the hydrodynamic model.

4.5. Hydrodynamic Model Validation

The model validation is defined as a procedure consisting in comparing the model output with available field or laboratory data to prove the model efficiency [Dias and Lopes, 2006].

One of the principles to be met in the validation procedure is that the data must be independent from the set used for calibration. During this work a different set of sea level time series was made available, and although pertaining to one of the stations used for calibration, a different period was considered for validation.

Also, given that data from a Doppler RCM 9 mkII Aanderaa currentmeter was available for two stations, the validation effort was extended to ascertain whether the hydrodynamic model was capable of a good representation of current velocities. This approach was taken with the prior knowledge that the comparing values would entail significant differences between model results and field data, since the former are related to the mean value over the vertical (depth integrated velocities) and over a horizontal spatial domain corresponding to the grid size ($1600m^2$ in this case), while the latter corresponded to data collected at a single point, in this case the position of the moored currentmeter.

Thus, the validation procedure was performed with a sea surface elevation time series for one station and depth integrated *u* and *v* current components for two other stations.

For station B (tidal gauge), during the validation process, the model was re-run using a one month water level time series, although for better visualization, shorter periods of time were used, as can be found in Fig.66 and Fig.67, where the best fit is shown. The model was run using a synthesized sea surface elevation time series considering three days for the spin up period (from 29th January at 00h00m until 29th February 2004)

All model parameters remained the same as for the calibration process. Obviously the model forcing at the West boundary was done with tidal data for February 2004, for all stations, since the currentmeters data pertained to 15th, 16th, 19th and 20th of the mentioned month.

The comparison of model results and data from station B (tidal gauge) is shown in Fig. 66 and Fig. 67.

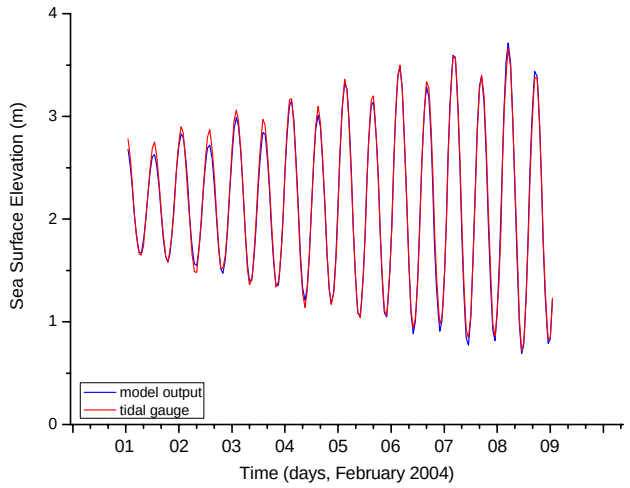

Fig. 66. Observed and modelled tidal sinusoidal for station B (8 days)

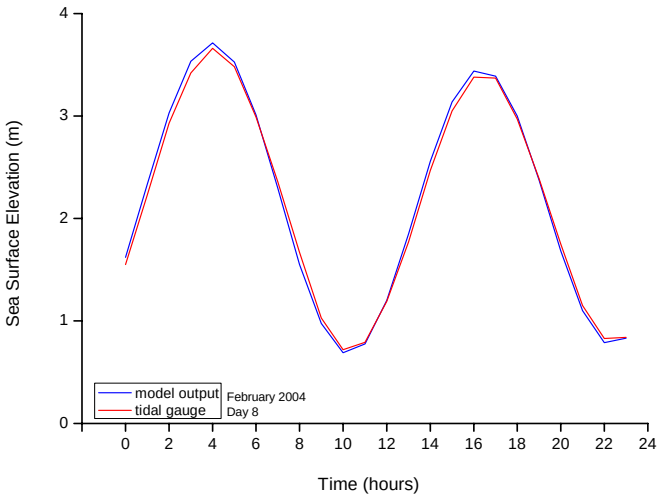

Fig. 67. Observed and modelled tidal sinusoidal for station B (24 hours)

Although visually it is quite clear a good match between observed and modelled sea surface elevations for station B, a quantitative assessment was deemed indispensable to complement this comparison. RMAE, RMS and SKILL were again computed taking into account a full month of data. The obtained values corroborate the good results, with RMAE value of 0.008, which falls into the excellent qualification, according to Walstra parameters (Table 9), the RMS value of 0.056 which corresponds to 1.75 % of the maximum tidal range for the considered period and a Skill value of 0.998, with 1.0 corresponding to the perfect match.

The other field data available for validation relates to the February 2004 campaign by the IH (Instituto Hidrográfico), when two currentmeters were deployed in neap tides (15^{th} and 16^{th}) and spring tides conditions (19^{th} and 20^{th}), mooring the devices at the port entrance and marina entrance for about 26 hours. This data was used previously in this work to characterize the tidal streams at Viana do Castelo, using the instrument's speed and direction output.

For the validation procedure, *u* (West-East) and *v* (South-North) current components were used, both from the currentmeter and the model output, for comparing purposes.

The model was again set to run, forced with ROMS tidal data for the whole February month (2004), with all other parameters remaining the same, including the 50 m^3s^{-1} river flow and the 3 days spin-up period.

Two virtual stations were placed in the model domain, matching the currentmeter deployment positions (Fig. 42 and Table 13).

Station		Coordinates				Depth
ID	Location	x	y	LAT(N)	LON(W)	
K	port entrance	26	45	41º40.8'N	008º50.4'W	4.0
D	marina entrance	66	81	41º41.3'N	008º49.2'W	2.7

Table 13 Coordinates of currentmeters used for validation

Results for station K at neap tides (15th and 16th):

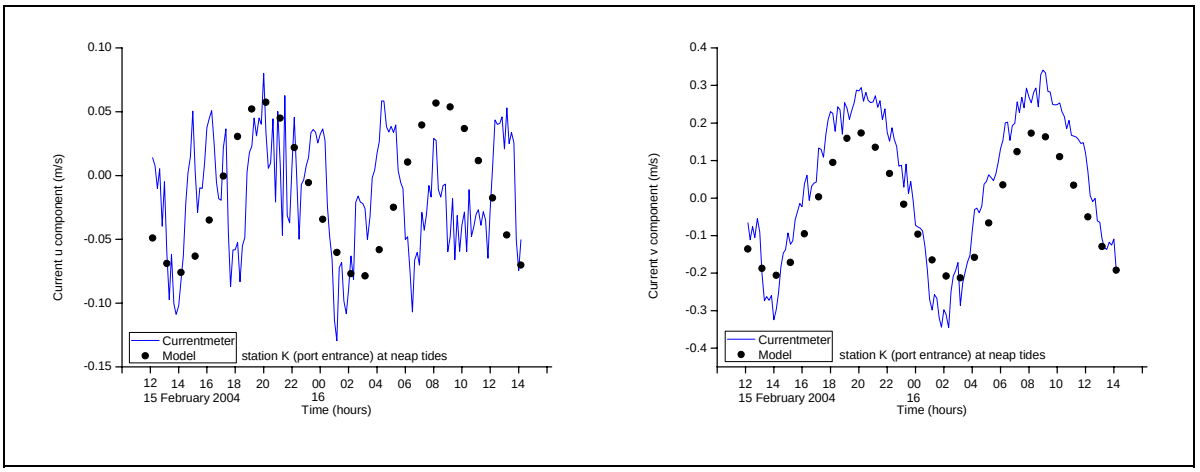

Fig. 68. Observed and modelled *u* and *v* current components for station K during neap tides

Results for station K at spring tides (19th and 20th):

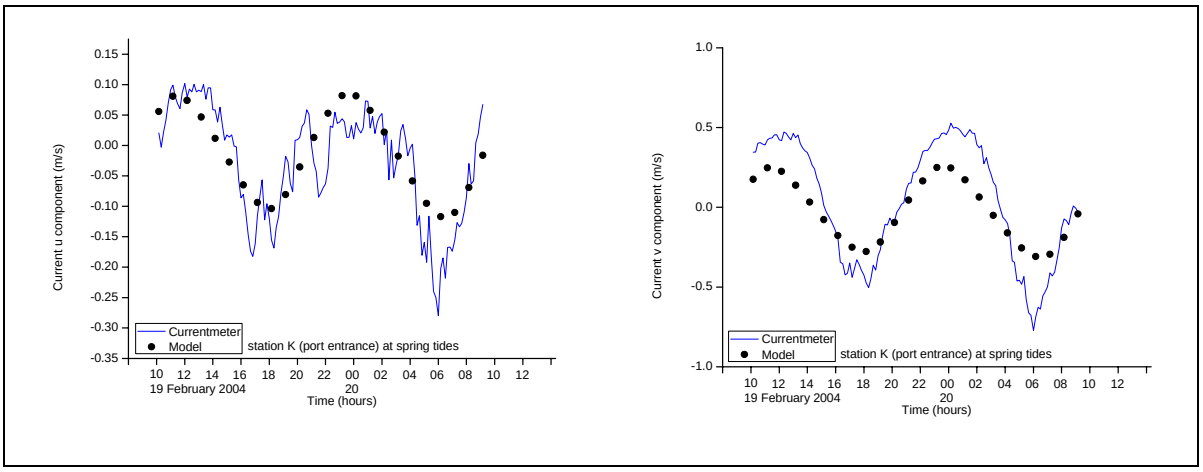

Fig. 69. Observed and modelled *u* and *v* current components for station K during spring tides

From the obtained plots (Fig. 68 and Fig. 69) it is evident a much better fit between modelled results and observed values for the *v* component, both in neap and spring tide conditions. This is probably due to the fact that at this location (port entrance) the main tidal flow occurs in a South-North direction when flooding and North-South direction when ebbing, following the breakwaters and main channel alignment. The magnitude of the *u* component is

much smaller than the *v* component and the flow movements on the *u* direction are thus somewhat erratic with the model not being capable of a satisfactory reproduction, namely for neap tides, when the flow is weaker. The location of station K in the bend of the channel, where a bifurcation takes place contributes to this imprecision of model results for the *u* component.

Results for station D at neap tides (15th and 16th):

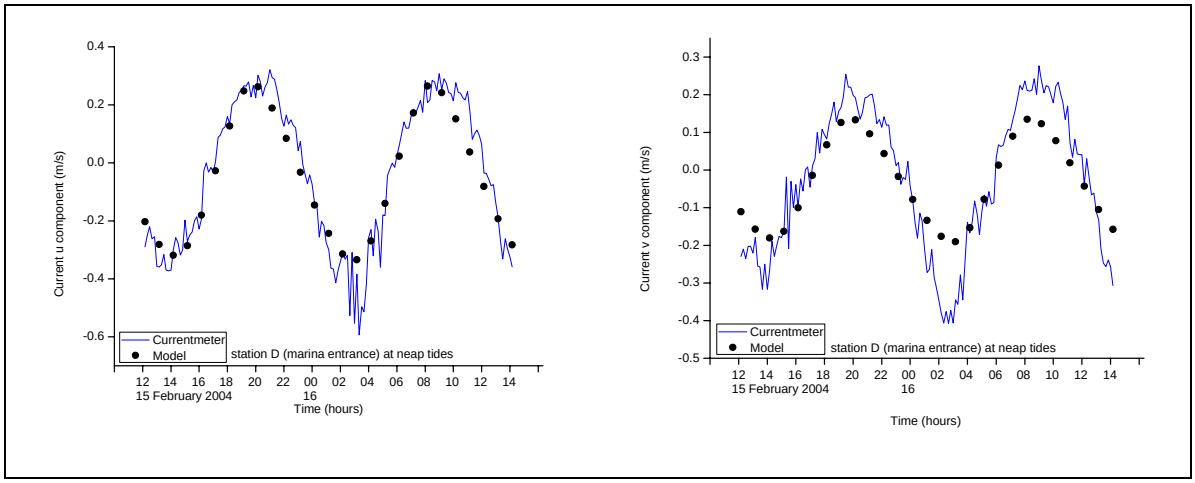

Fig. 70. Observed and modelled *u* and *v* current components for station D during neap tides

Results for station D at spring tides (19th and 20th):

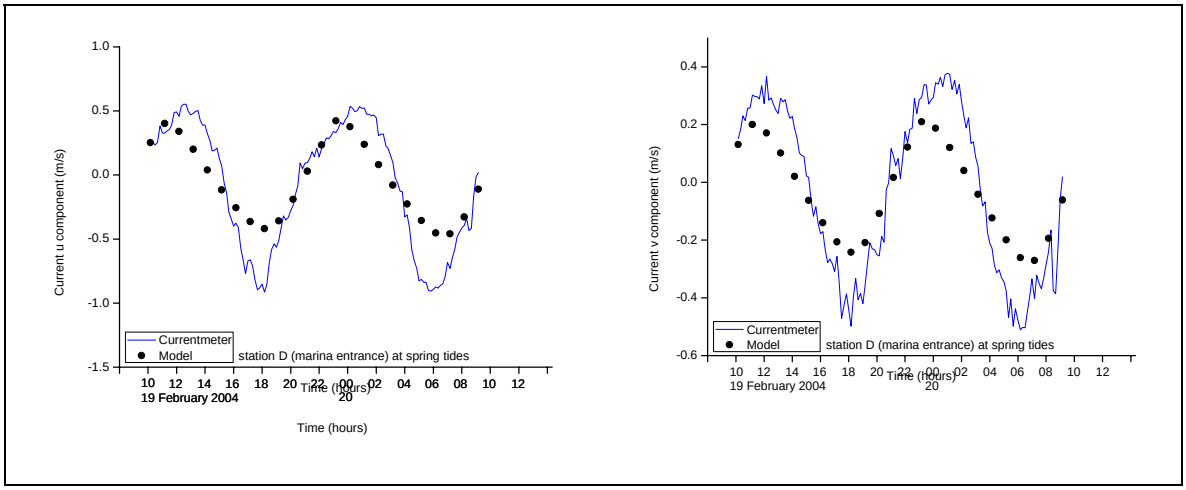

Fig. 71. Observed and modelled *u* and *v* current components for station D during spring tides

For station D (marina entrance) the results are much more satisfactory as can be seen from the plotted current components (Fig. 70 and Fig. 71). The magnitudes of *u* and *v* components are much similar. This is because the main tidal flow follows the river alignment on a Southwest-Northeast direction when flooding and the opposite direction when ebbing.

It is also noticeable a slight divergence between model results and recorded values on the negative side of the *u* component (ebbing tide) that suggests that the river flow input to the model must be adjusted (increased) for this condition. In this domain the river flow is always unclear since, as previously stated in this work, it is highly dependent on the dam's energy production and no reliable river flow data is available.

The overall better fit of the model results to the recorded values for station D is also inherent to the fact that this location is much shallower than the port entrance, thus making the depth integrated velocities more similar to the spot measured velocities of the currentmeter.

In order to have an overall understanding of the scale of the errors between modelled depth integrated currents and observed spot measured currents, a complete RMS evaluation was performed for both stations, for neap and spring tides conditions (Table 14):

station	date	tide	RMS		% amplitude
K	15th and 16th Feb 2004	neaps	*comp u*	0.056	26.7
			comp v	0.106	15.4
K	19th and 20th Feb 2004	spring	*comp u*	0.051	13.3
			comp v	0.198	15.2
D	15th and 16th Feb 2004	neaps	*comp u*	0.062	6.8
			comp v	0.087	12.7
D	19th and 20th Feb 2004	spring	*comp u*	0.231	15.7
			comp v	0.146	16.4

Table 14. RMS assessment for K and D stations.

The obtained results when compared to the maximum amplitude of the current can be considered satisfactory, considering that the comparison is between depth integrated current over an area the size of the cell and spot measured current at a single point. In fact removing the extreme values of 26.7 % and 6.8 % of the current amplitude all other results are within 12.7% / 16.4%.

After the validation procedure the model reproduction of the system was considered satisfactory and adequate to simulate the hydrodynamic processes occurring within Viana do Castelo port area, given the aims of this work.

Nevertheless, there are some limitations that must be considered when using the model. Those limitations explain the deviations between the model results and field observations.

Firstly, there are conceptual errors arising from inaccuracies at the model definition stage, such as the bathymetry resolution being limited by a grid cell dimension of 40m X 40m, the assumptions and simplifications in the definition of the equations system, the distortion of the land boundaries produced by the grid, the uncertainty of the river flow data, the ocean boundary being forced with a model synthesized tide and the slight stratification observed with certain combinations of tides and river flow.

Also significant at the calibration and validation stage was the lack of longer sea level elevation and current time series for different stations within the model domain.

In spite all of the above, the hydrodynamic model becomes more and more reliable with its use and validation for different conditions and different applications. Confidence in the model can only be increased by experimenting with that model, *i.e.,* by carrying all kinds of validation tests [STOWA/RIZA, 1999]. At the end of the process, the model becomes an important tool for studying the hydrodynamics of the study area.

5. Use of the hydrodynamic model for simulations

Once the model has been calibrated, validated and thoroughly tested and there is an increased confidence on its operation the next logical step is to use it for different applications.

Although not anticipated at the early stages of this study, the model was used for much more purposes than the ones previously defined, *i.e.*, tidal propagation and Lagrangian transport of particles.

A list of the model applications on this work is summarized on Table 15.

Simulated scenarios	
1	Tidal propagation for several stations within the estuary including the upper reaches
2	Graphical plots of the study area hydrodynamics for different tidal and river flow regimes
3	Quantification and comparison of currents for different selected stations
4	Behaviour of the hydrodynamics with different river flow input
5	Hydrodynamics changes introduced by dredging and port expansion works
6	Calculation of the river flow/tidal prism ratio for different conditions
7	Lagrangian transport of particles (release of single particle and continuous spot emission)
8	Propagation of Harmonic Constituents within the estuary

Table 15. Simulated scenarios with the model.

5.1. Tidal propagation

In order to ascertain the tidal propagation upstream the estuary, seven virtual stations (Table 16) were introduced in the model grid (Fig. 72). The data gathered from these stations represents the model output for sea surface elevation time series.

Station		Coordinates				
ID	Location	x	y	LAT(N)	LON(W)	Z_0
A	port entrance	25	35	41º40.6'	008º50.5'	8.20
B	tidal gauge	31	62	41º41.2'	008º50.4'	1.50
C	south expansion area	51	56	41º41.05'	008º49.7'	1.06
D	marina entrance	67	82	41º41'.6	008º49.3'	4.14
E	east boundary	139	87	41º41.6'	008º47.15'	1.00
F	south channel	102	74	41º41.4'	008º48.35'	1.02
G	north channel	113	96	41º41.7'	008º47.7'	2.34

Table 16. Virtual stations for tide propagation study.

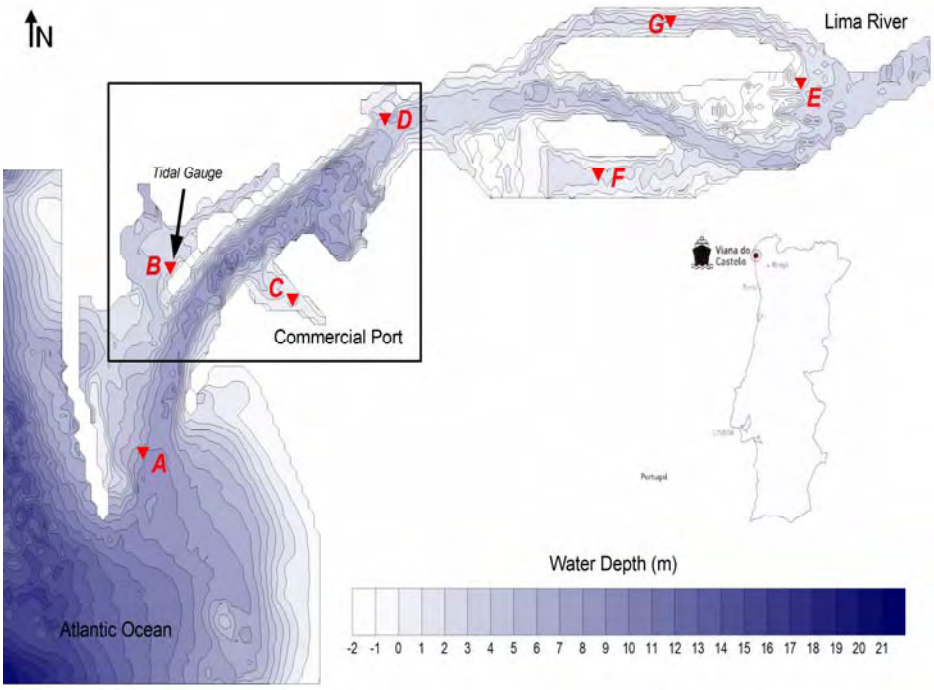

Fig. 72. Model grid showing virtual stations location.

The model was run for a full month (March 2005) with a river flow of 50 m^3s^{-1} and sea surface elevation data gathered from all virtual stations, with the purpose of ascertain if there was any distortion of the tidal sinusoidal on the upper reaches of the estuary.

It is important to note, however, that the model was considered calibrated and validated only to the port area (*i.e.* downstream of the Eiffel Bridge, up to station D), where tidal and current data was available. The upper estuary section was included in the model grid in order to achieve the most reliable hydrodynamic condition upstream the port area.

Nevertheless, since the model grid contains a valid bathymetry to this area, it was considered pertinent to check how the tidal wave propagation up to the East boundary was being reproduced by the model.

The obtained results (Fig. 73, bottom plot) reveal that there are only minor differences between the station closer to the West boundary, where the tide is being forced (station A), and the farthest stations, namely stations F, G and E. This results on superimposed sinusoidal lines. On the upper plot (Fig. 73), the differences on sea surface elevation between those stations were plotted on a different scale and the vertical grid lines were kept visible allowing for a better interpretation. The plot shows that maximum differences are attained at mid-tide, whether ebbing or flooding, while differences close to zero are observed near HW and LW times.

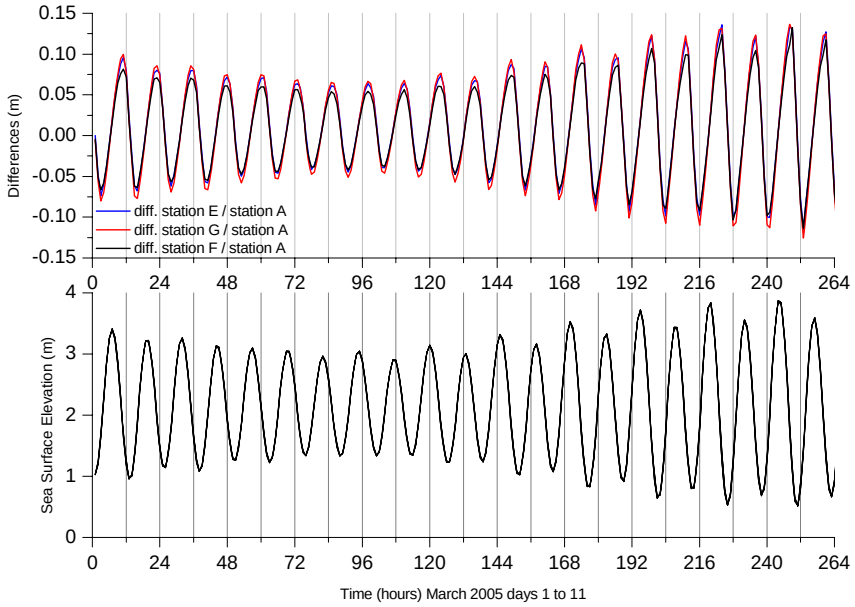

Fig. 73. Tidal sinusoidal comparison for stations A, F, G and E.

A closer look to the differences between these stations sea surface elevations (Fig. 74) reveal a slight phase shift responsible for instant differences up to 12 cm at spring tides conditions and up to 8 cm at neap tides.

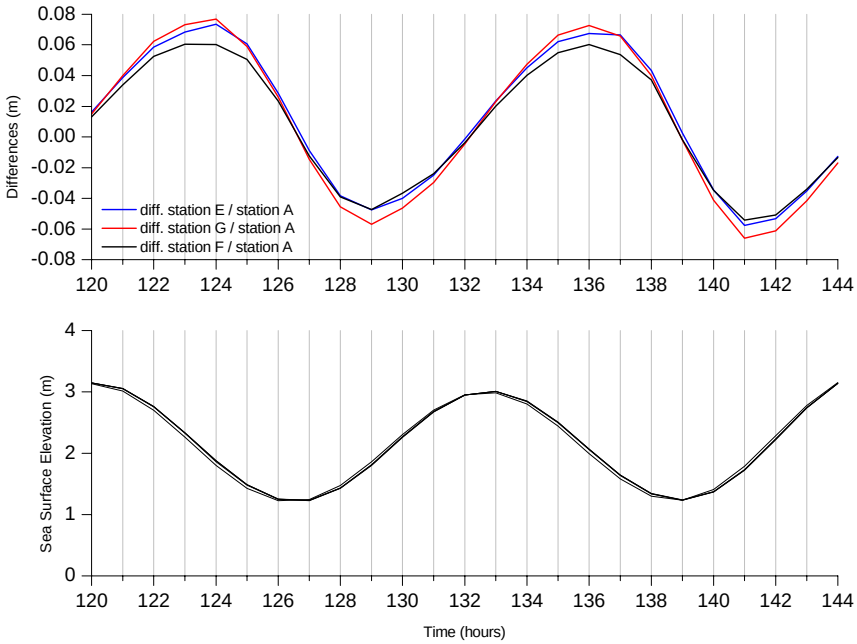

Fig. 74. Tidal sinusoidal comparison for stations A, F, G and E (closer).

The higher differences are observed not at the farthest station but at station G, at the North channel. These differences are higher at the ebbing stage and are probably due to channel constriction and bathymetry layout. This feature would have to be confirmed locally with the collection of simultaneous sea surface elevation field data.

It is worth mention that there are field studies by LNEC (Laboratório Nacional de Engenharia Civil) with the purpose of building a physical model to the study of harbour configuration, which shows tidal attenuation starting from about 1000 m from the (then) estuary mouth [LNEC, 1969]. This data is not usable on this work since the port entrance, harbour configuration and estuary bathymetry have been dramatically changed during the 80’s decade new port construction on the left margin.

5.2. Study area hydrodynamics

One of the main capabilities of the numerical model is to provide raw data that after being carefully processed, through a graphical interface, allow for an overall view of the hydrodynamic processes taking place within the study area.

Within the scope of this study it was decided to produce graphical plots of currents for different tide conditions, namely neap tides, average tides and spring tides. The selected periods are from March 2005 and the model was run for a 50 m^3s^{-1} river flow and 6 minutes temporal resolution.

The results are presented with indication of the plot instant in the tidal sinusoidal.

Graphical plots for neap tide condition (19th March 2005):

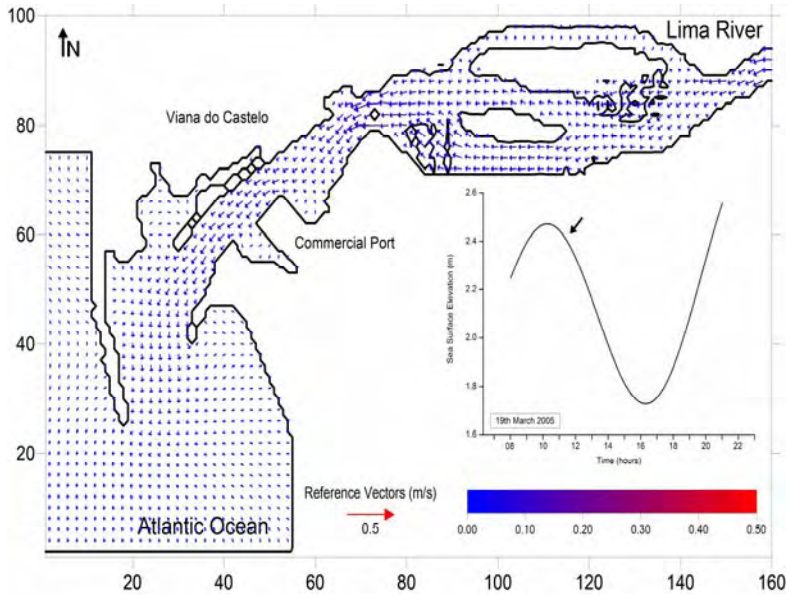

Fig 75. Currents plot for neap tides, 1 hour after HW

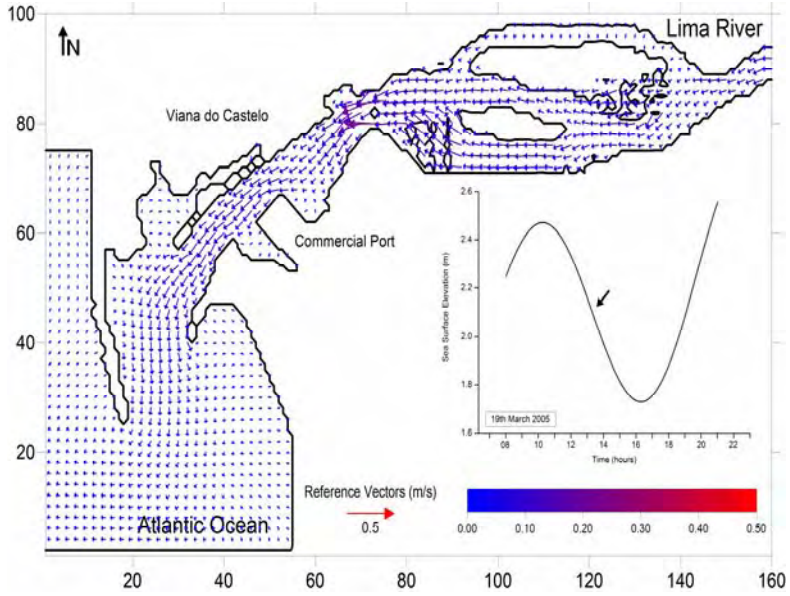

Fig 76. Currents plot for neap tides, 3 hours after HW

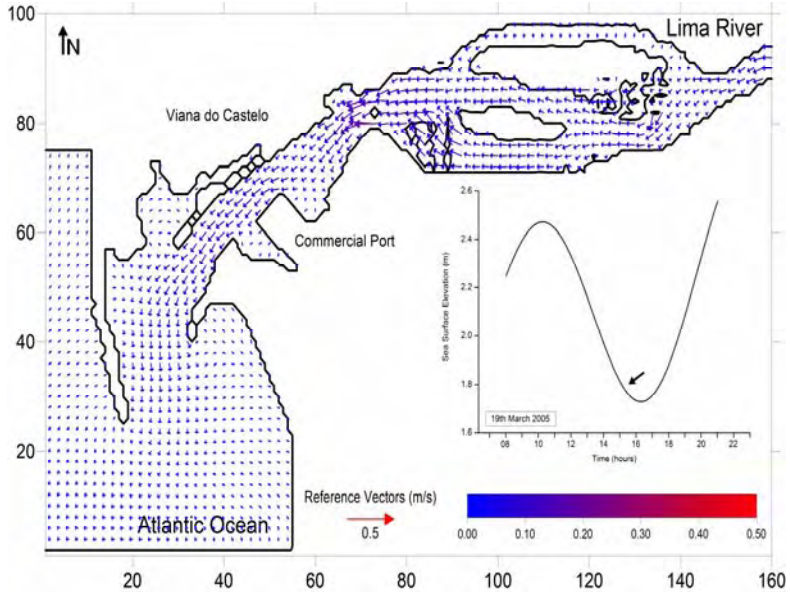

Fig 77. Currents plot for neap tides, 5 hours after HW

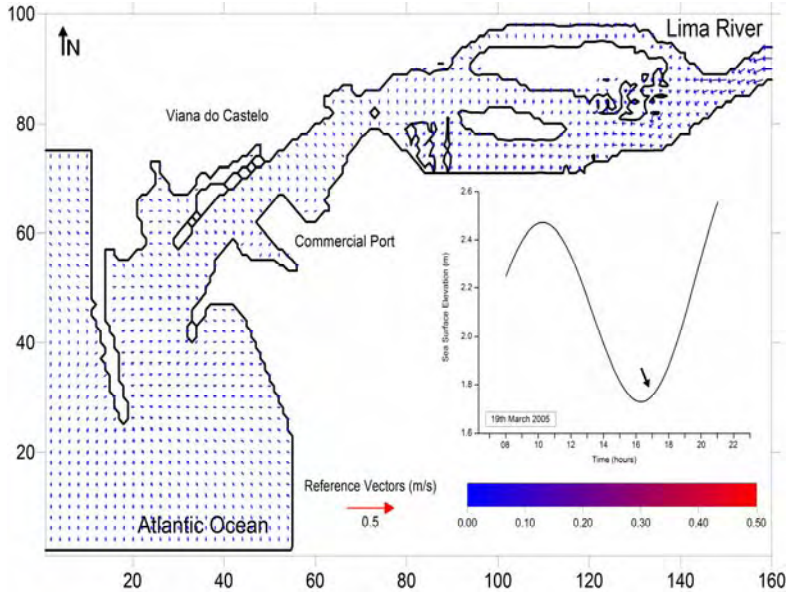

Fig 78. Currents plot for neap tides, 1 hour after LW

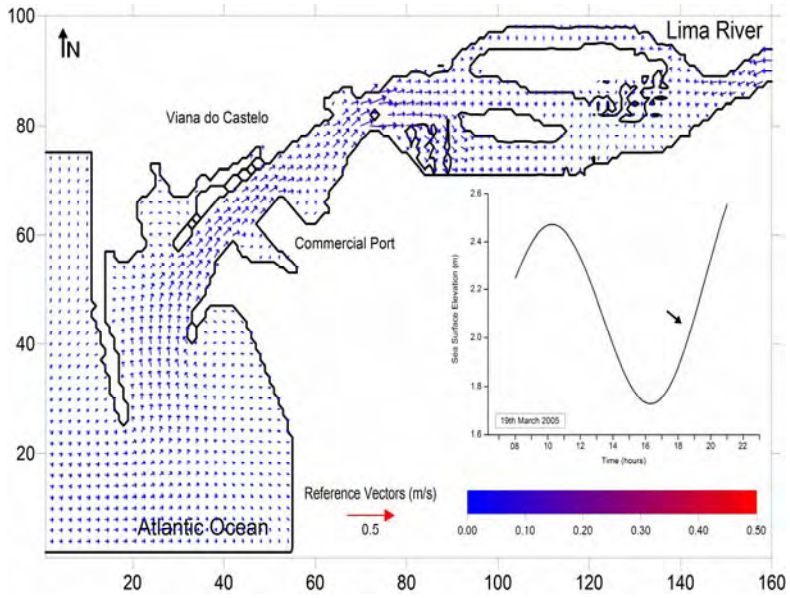

Fig 79. Currents plot for neap tides, 3 hours after LW

Graphical plots for average tide condition (2nd March 2005):

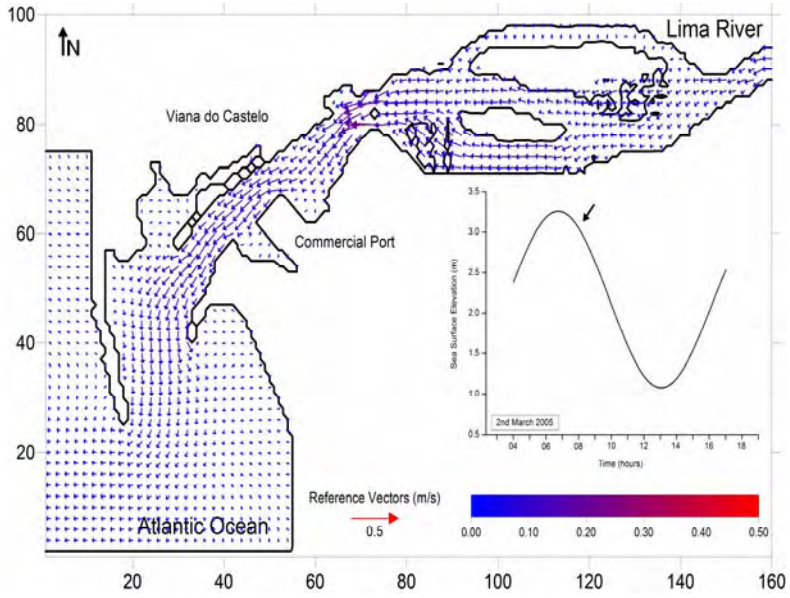

Fig 80. Currents plot for average tides, 1 hour after HW

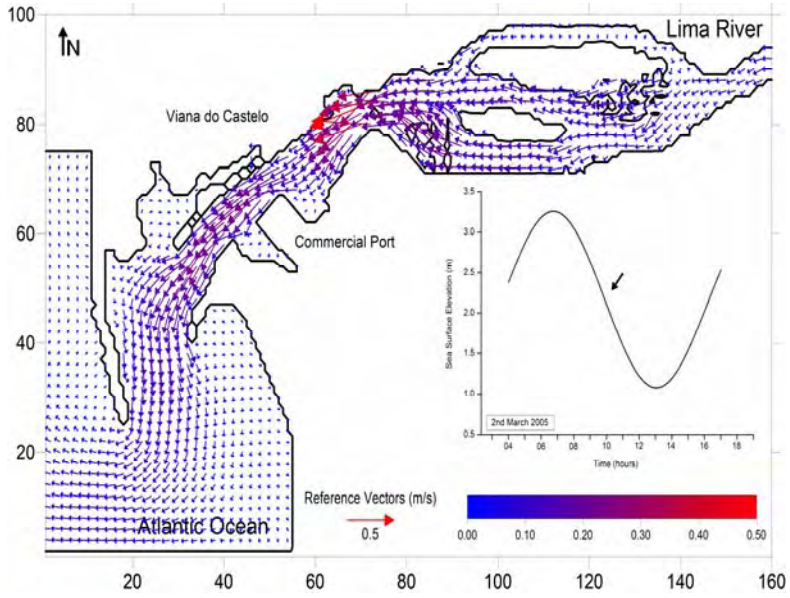

Fig 81. Currents plot for average tides, 3 hours after HW

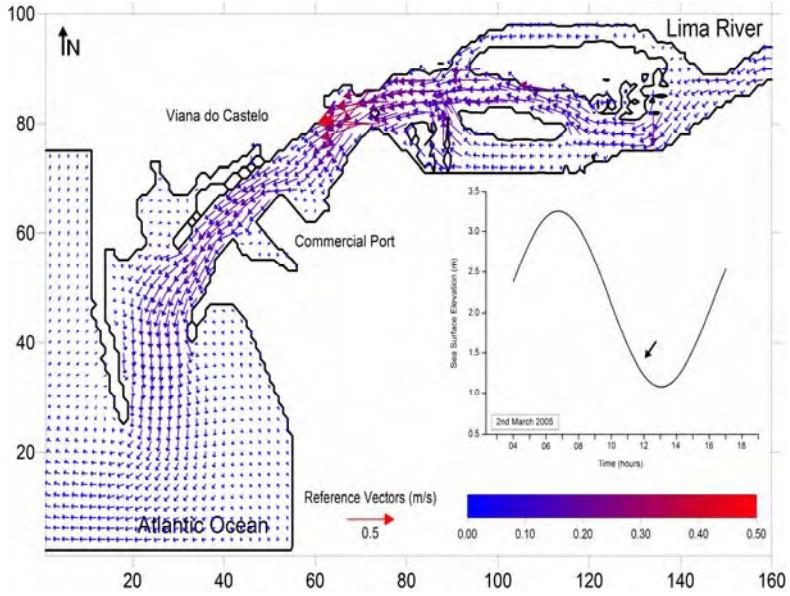

Fig 82. Currents plot for average tides, 1, 3 and 5 hours after HW

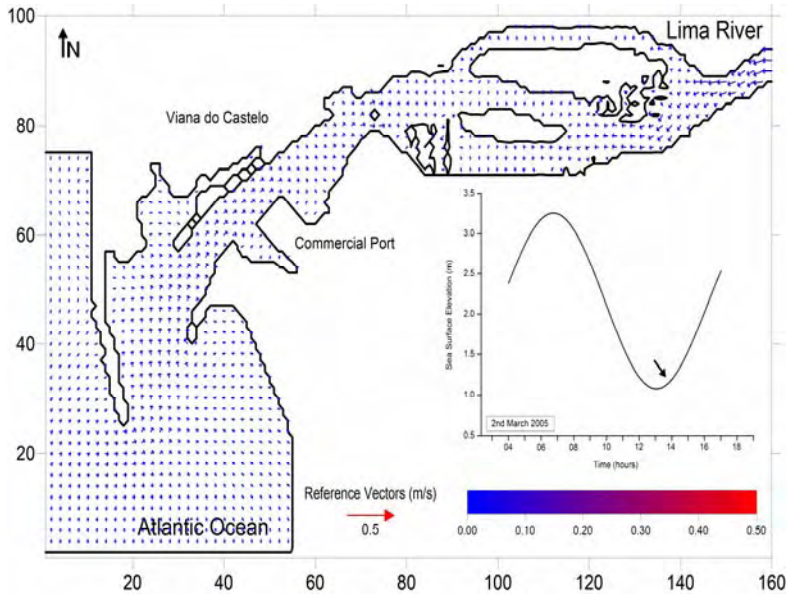

Fig 83. Currents plot for average tides, 1 hour after LW

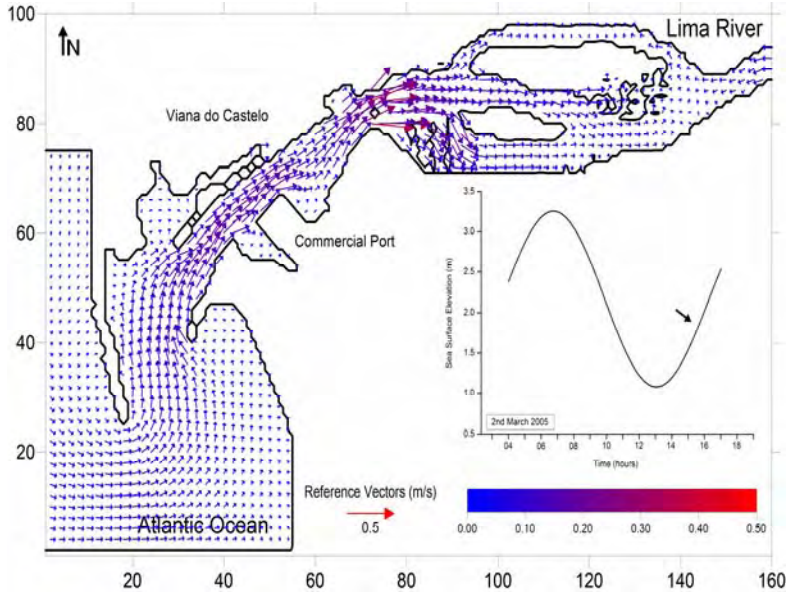

Fig 84. Currents plot for average tides, 3 hours after LW

Graphical plots for spring tide condition (11th March 2005):

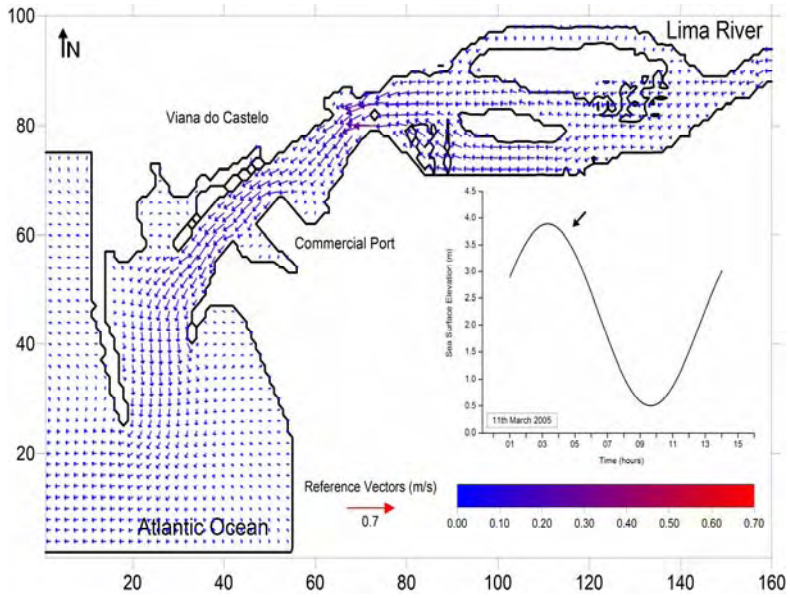

Fig 85. Currents plot for spring tides, 1 hour after HW

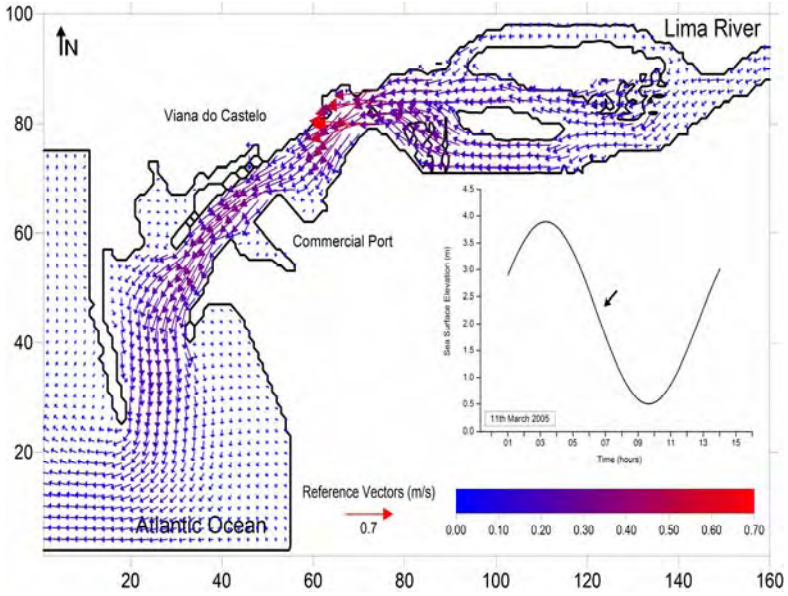

Fig 86. Currents plot for spring tides, 3 hours after HW

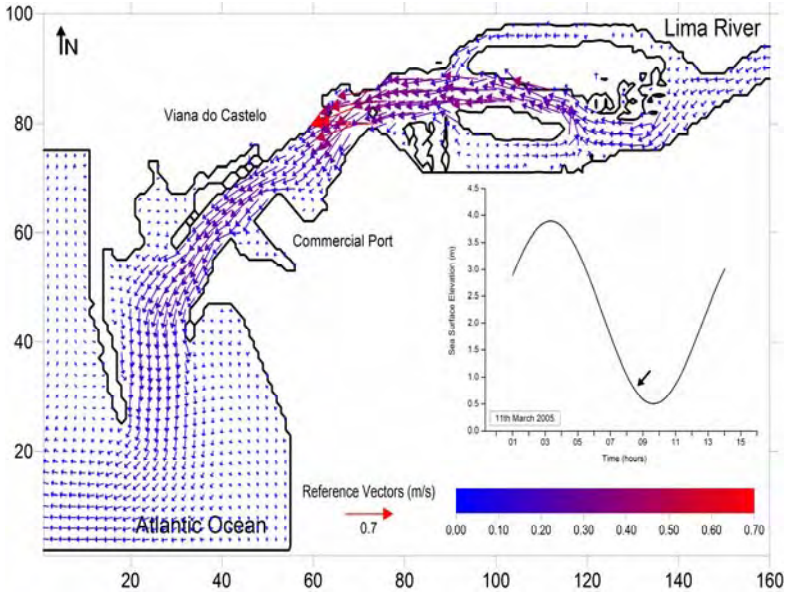

Fig 87. Currents plot for spring tides, 5 hours after HW

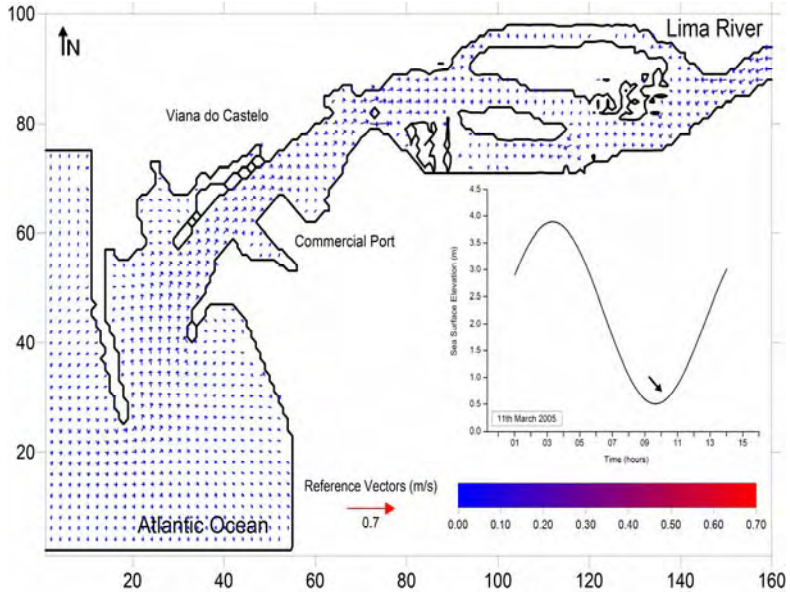

Fig 88. Currents plot for spring tides, 1 hour after LW

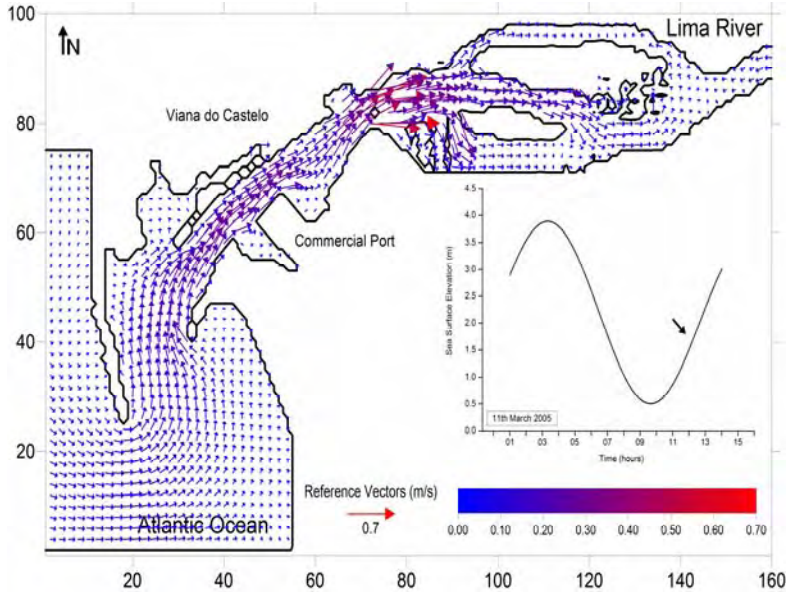

Fig 89. Currents plot for spring tides, 3 hours after LW

From the above displayed plots (Fig. 75 through Fig. 89) it is evident that the estuary hydrodynamics is greatly influenced by the tidal regime, with large differences in the current velocity between neap tides and spring tides condition, as it was anticipated. Also relevant to note the stronger current along the

main navigation channel and the maximum values observed close to the transition from the port area to the upper estuary, where a constriction in the layout occurs, enhanced by the presence of the bridge pillars.

5.3. Comparison and quantification of currents for different stations.

Although extremely important for an overall observation of the study area hydrodynamics, the graphical plots lack the proper spot quantification of the depth averaged *u* and *v* currents components. It is therefore essential to place virtual stations on the exact locations where the data is important in order to make a correct assessment of the situation.

It was decided to place three virtual stations on the model domain (Fig. 90) with the purpose of collecting current and tidal data.

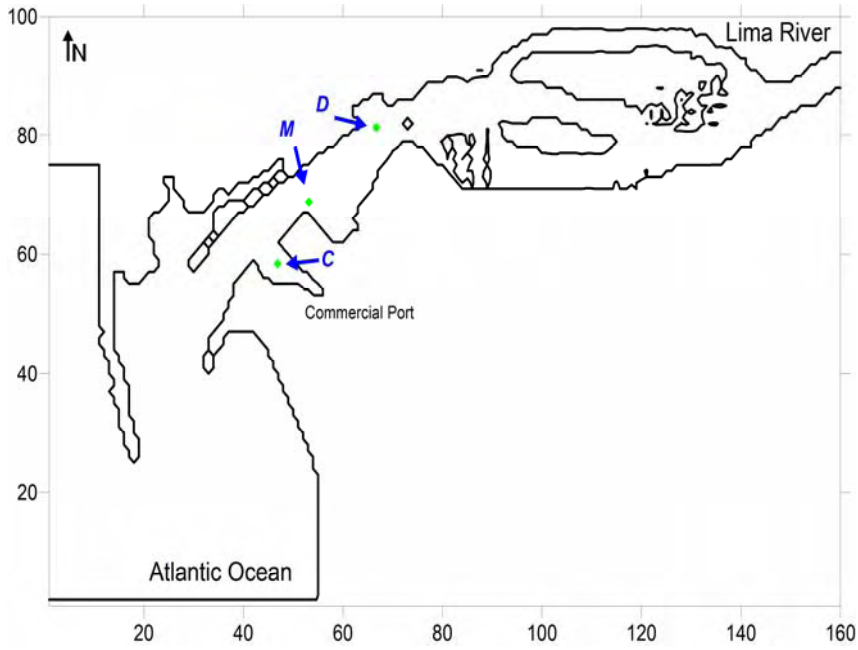

Fig. 90. Location of stations for current analysis.

Station M was chosen due to its critical position in terms of navigation. Being located on the corner of the commercial harbour berthing structure, it becomes important to quantify the depth averaged current processes occurring on this spot, from the navigation point of view.

Station C is located on a part of the estuary where little or none information is available, even by local knowledge. It is also one of the future expansion areas of the port facilities, hence its study necessity.

Station D was selected as a reference station, due to the existence of currentmeter data as well as for being close to the estuary area where maximum velocities are attained.

The model was re-run with a 50 m^3s^{-1} river flow at the East boundary and forced with a full month (March 2005) tidal data at the West boundary. Data periods pertaining to neap, spring and average tides were collected with the model set to a 10 minute temporal resolution.

The obtained data for station C (Fig. 91) shows a negligible influence of the currents in this local. As it was already presumed by the previous graphical plots, the main current flow is kept in the channel axis with little incursion inside the embayment.

From neap tide condition to an average tide condition there is a significant increase to the double of both *u* and *v* components, although still very small. The difference from average tide condition to spring tide is not so important.

The *u* component follows the main channel flow, with a westward (negative) movement at the ebbing stage, with maximum intensity at mid-tide, while at flooding the movement is the opposite. The *v* component has northward (positive) movement while ebbing, with the water inside the embayment exiting to the main channel, and a southward movement while flooding.

There are no remarkable differences of behaviour (other than current intensity) between the different tide scenarios simulated.

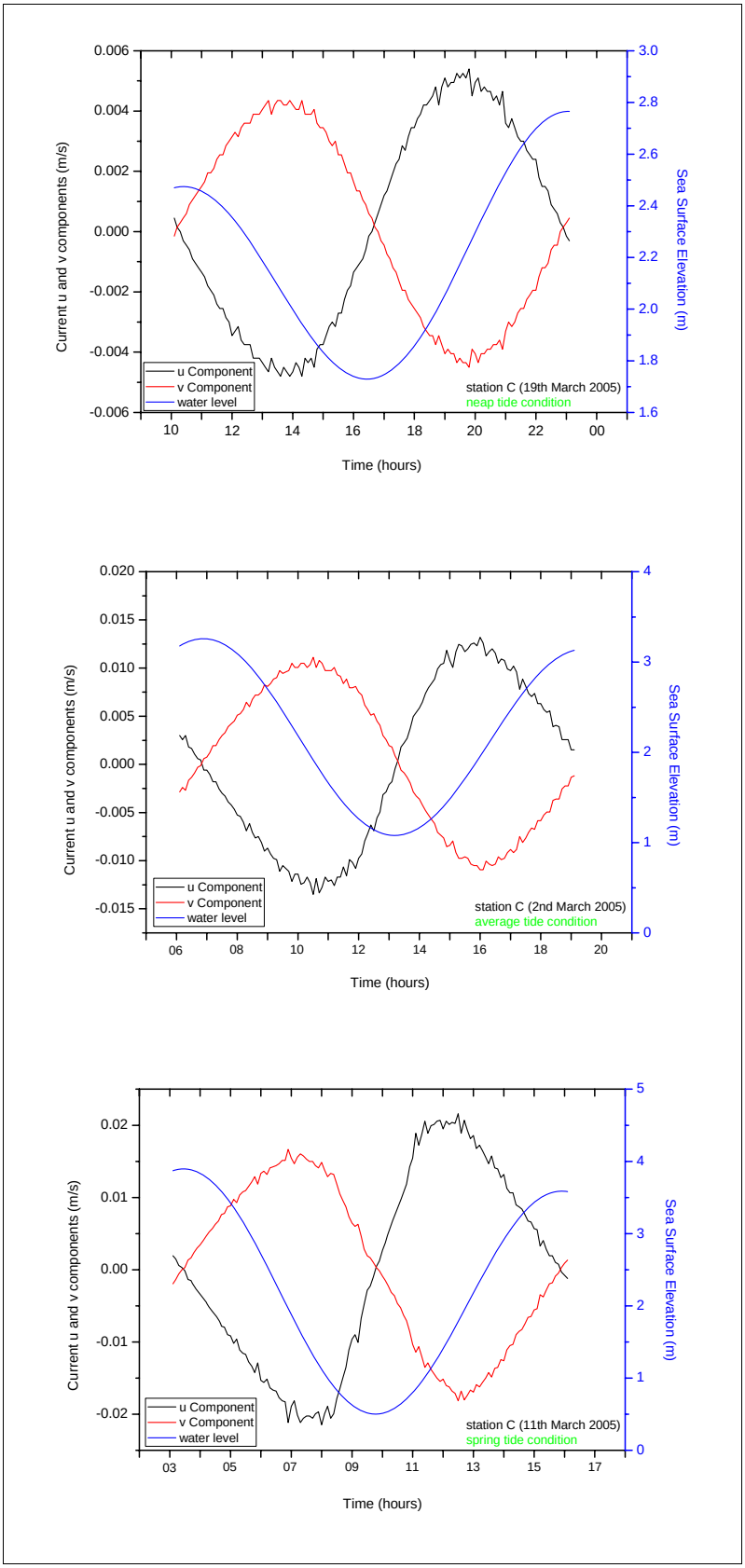

Fig. 91. *u* and *v* current components for station C

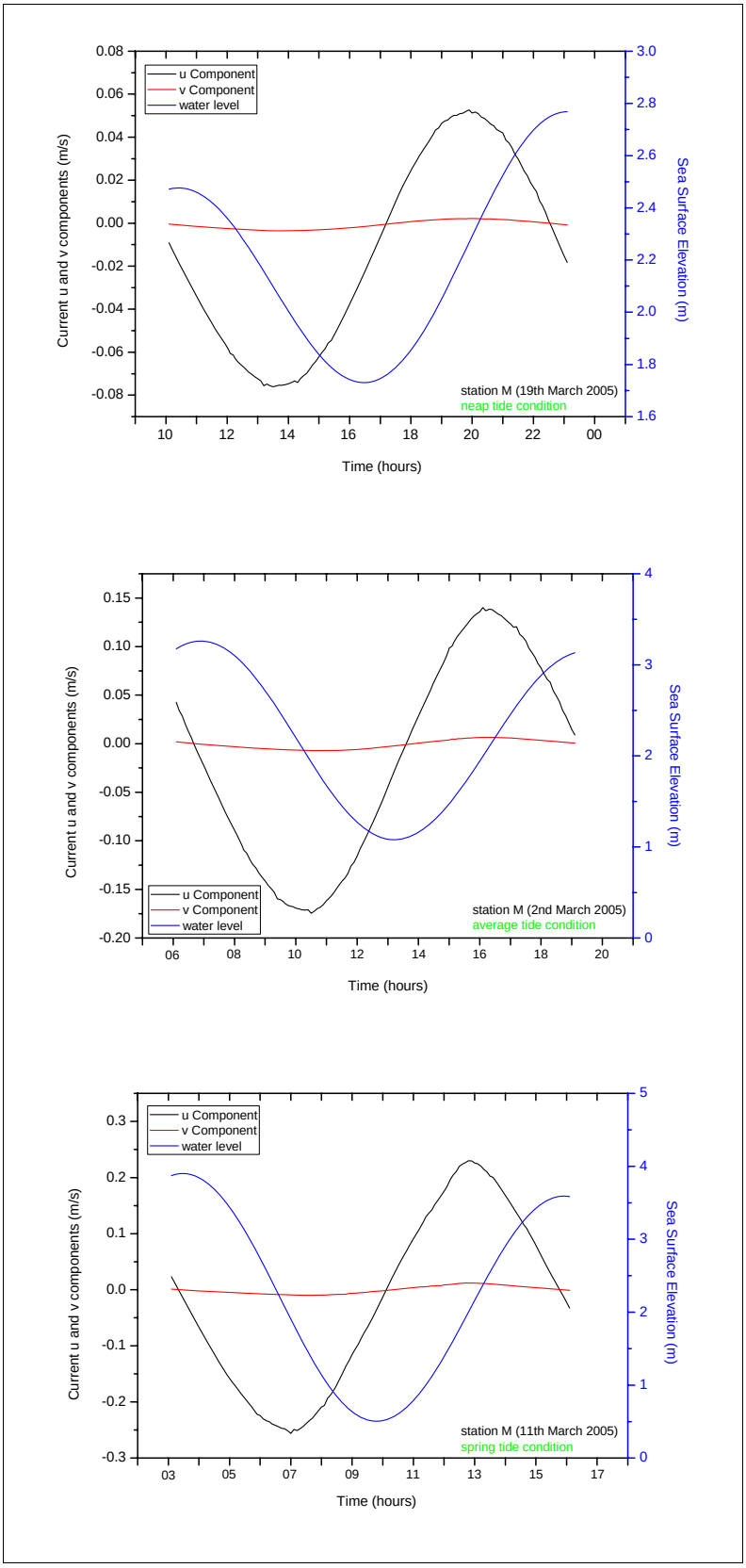

Fig. 92. *u* and *v* current components for station M

The obtained data for station M (Fig. 92) shows a more gradual increase on the velocities, from neap to spring tide conditions.

One significant aspect is the almost negligible importance of the *v* component at any tide condition, even if the station is located adjacent to the main flow, with a northeast-southwest flow when ebbing and southwest-northeast while flooding that would suggest a more important *v* component. This behaviour is probably due to the influence of the nearby berth infrastructure that deflects the current.

The maximum values of the *u* component are reached at mid-tide, whether ebbing or flooding, with the negative movement (ebbing) slightly greater than the eastward movement, revealing the influence of the river flow at this station, except for spring tide condition, when ebb and flood *u* components are almost the same.

At station D, both *u* and *v* components follow the expected northeast-southwest flow while ebbing and southwest-northeast while flooding, resulting in very similar *u* and *v* patterns and magnitudes.

The maximum values of both *u* and *v* components are reached at mid-tide, whether ebbing or flooding, with the flow reversing at the approximate times of LW and HW.

These simulations represent a powerful tool for the study of the hydrodynamic behaviour at a given location, allowing for proper comparison between stations as well as permitting the adjustment of certain parameters and the response of local hydrodynamics to those changes.

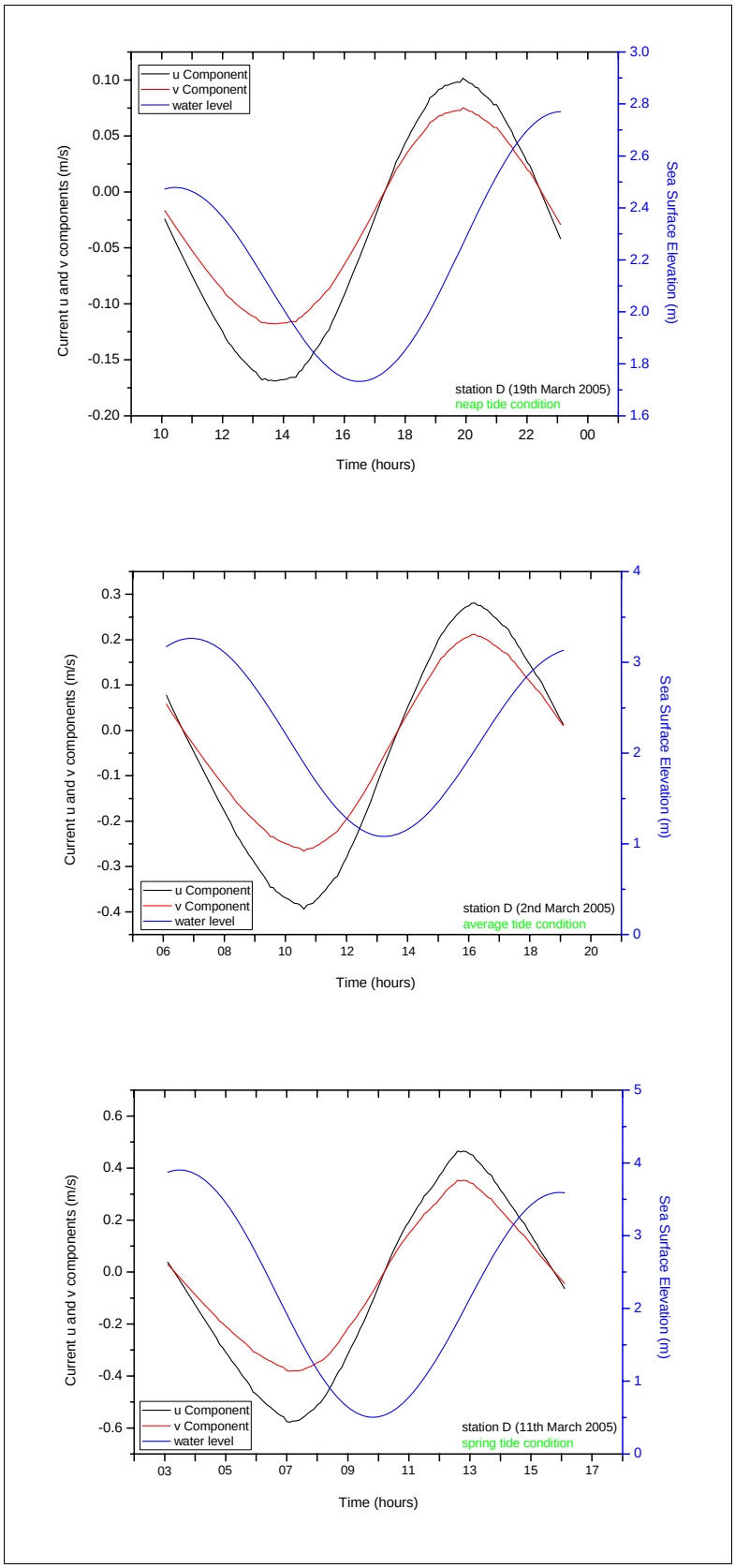

Fig. 93. *u* and *v* current components for station D

5.4. Varying the river flow for different stations.

One of the most difficult parameters to accurately define at the set up process of the model is the river flow. Not only because there is a lack of updated information regarding this subject but also due to the varying nature of the fresh water input to an estuary even at short time scales, which is usually consequence of several unpredictable and indeterminate factors

Nevertheless it was considered useful to employ four different values for different scenarios as an input to the model and try to understand whether these different flows would introduce significant changes to the study area hydrodynamics. The model was forced with a constant river flow of 4 m^3s^{-1}, 50 m^3s^{-1}, 100 m^3s^{-1} and 200 m^3s^{-1}, as defined in a previous section of this work. The chosen period remained the same, comprising an average tide. Stations C, M and D were assessed.

For station C, the changes introduced by different values of river flow are negligible (Fig. 94). As previously stated, this station was placed inside an embayment outside the main channel flow, thus not being affected by its magnitude changes.

Stations M and D show a similar response pattern to the increasing river flow (Figs. 95 and 96), although different in magnitude, because the *v* component of station M is very low, as previously observed.

Both stations exhibit a common characteristic which is an increase in the negative part of both components (meaning an increase towards Southwest) with the river flow increased, and a decrease on the positive part of both components, *i.e.*, a decrease towards Northeast. This means that with increased river flow the ebbing stream is enhanced while the flooding stream is diminished.

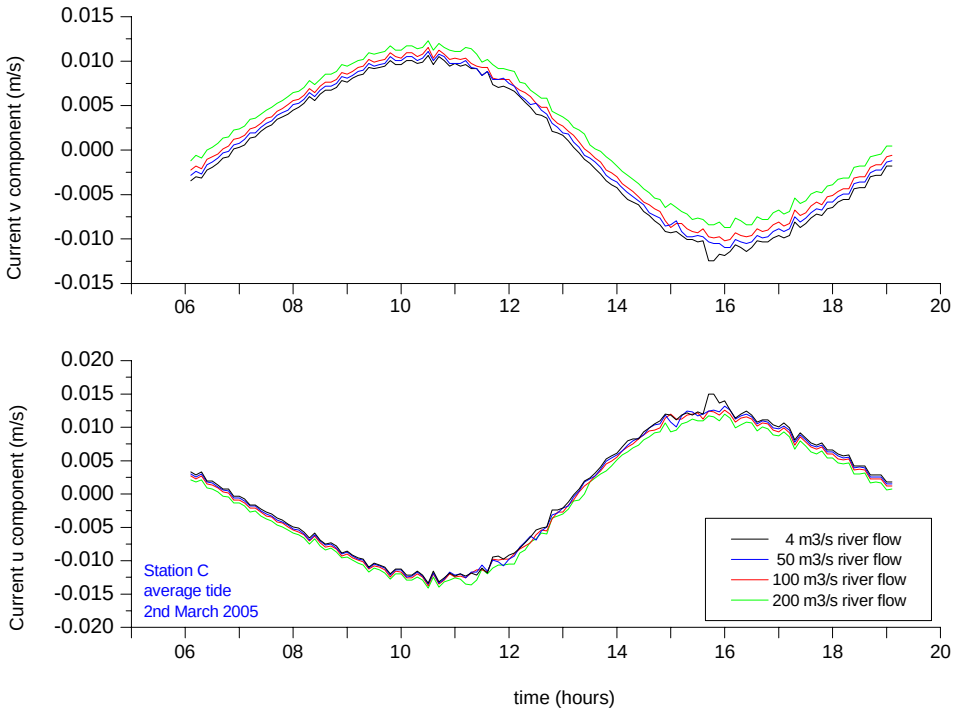

Fig. 94. Current u and v components variation with different river flows for station C

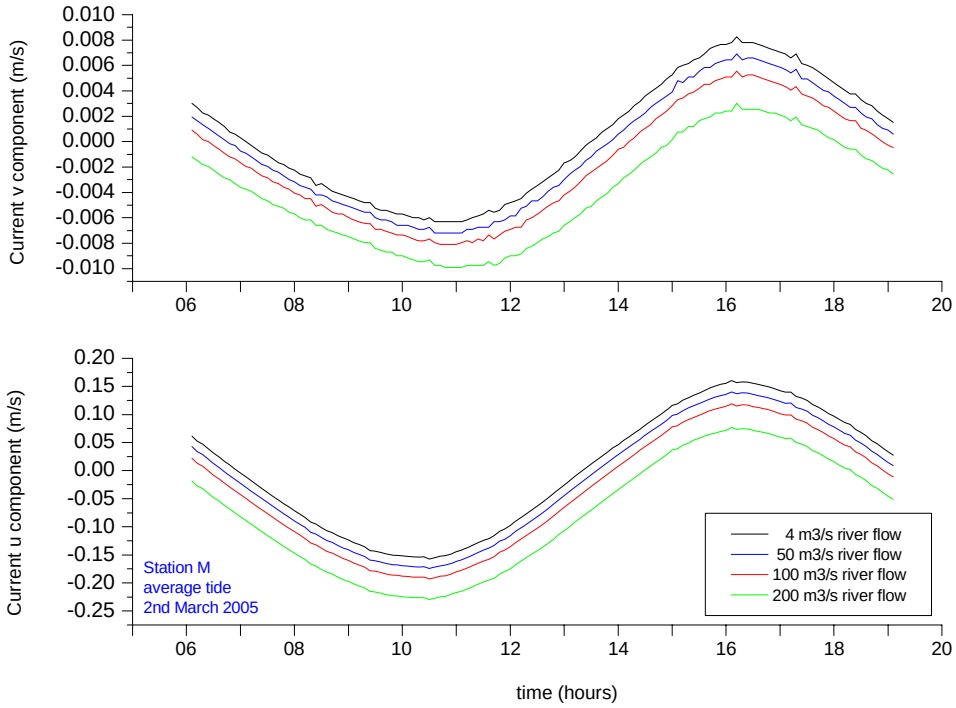

Fig. 95. Current u and v components variation with different river flows for station M

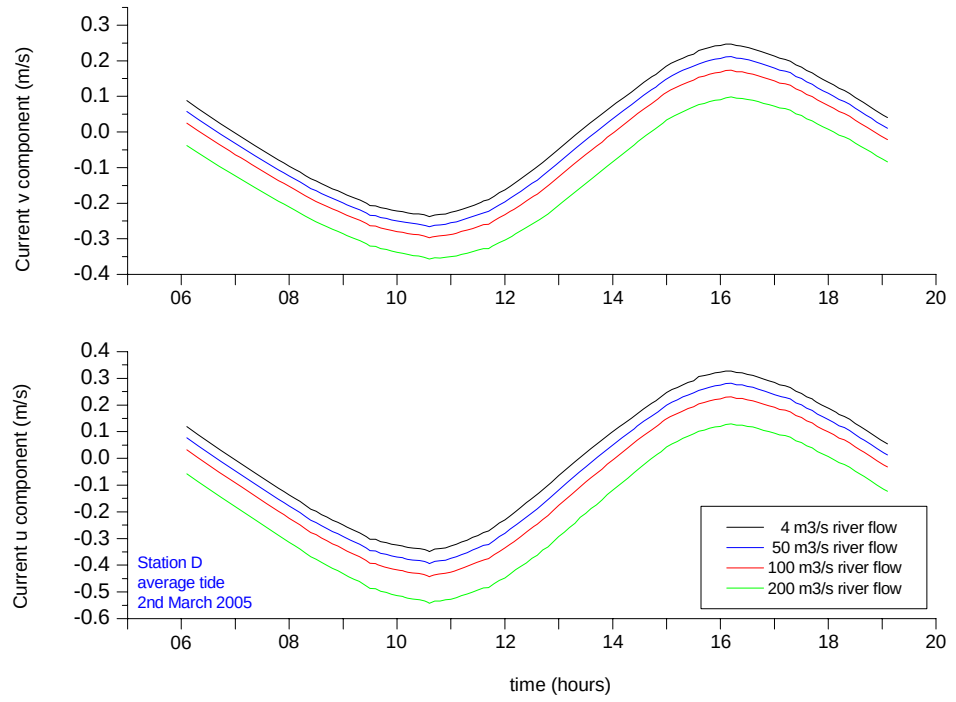

Fig. 96. Current u and v components variation with different river flows for station D

5.5. Hydrodynamic changes introduced by alterations to the bathymetry

The effects of harbour engineering works on an estuary are diverse and include the modifying of hydrodynamic behaviour.

The estuary study area comprises the commercial harbour waters downstream of Eiffel Bridge. This section of the work focus on the new expansion area layout, aiming the determination of possible changes to the hydrodynamics due to bathymetry and port configuration changes.

Three virtual stations were placed in the domain (Fig.90). One is located on the most sensitive area from the navigation point of view (station M), another (station C) was placed where major changes to bathymetry are expected due to port expansion and the other was placed in a position where data from a moored currentmeter was available (for comparison purposes).

Two grids were constructed, one representing the present situation of the port, which was used throughout this work, and the other with a slight different berth layout as well as different bathymetry (Fig. 97), consequence of the expected dredging works to deepen and widen the manoeuvring basins.

The model was then run for average tides and spring tides conditions as well as 50 m^3s^{-1} and 100 m^3s^{-1} river flows.

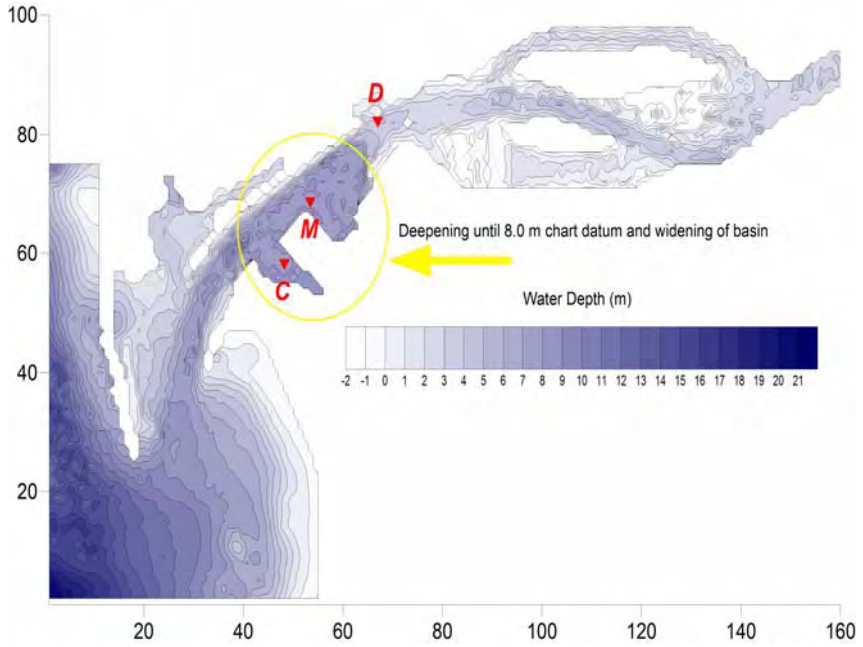

Fig. 97. Model grid with bathymetry changes.

To better assess the changes introduced on the new grid, consequence of the dredging works, it was found suitable to build a grid where only the modified area would show. For this purpose the second matrix was subtracted from the original one, resulting in a new grid where the changes are quantified (Fig. 98).

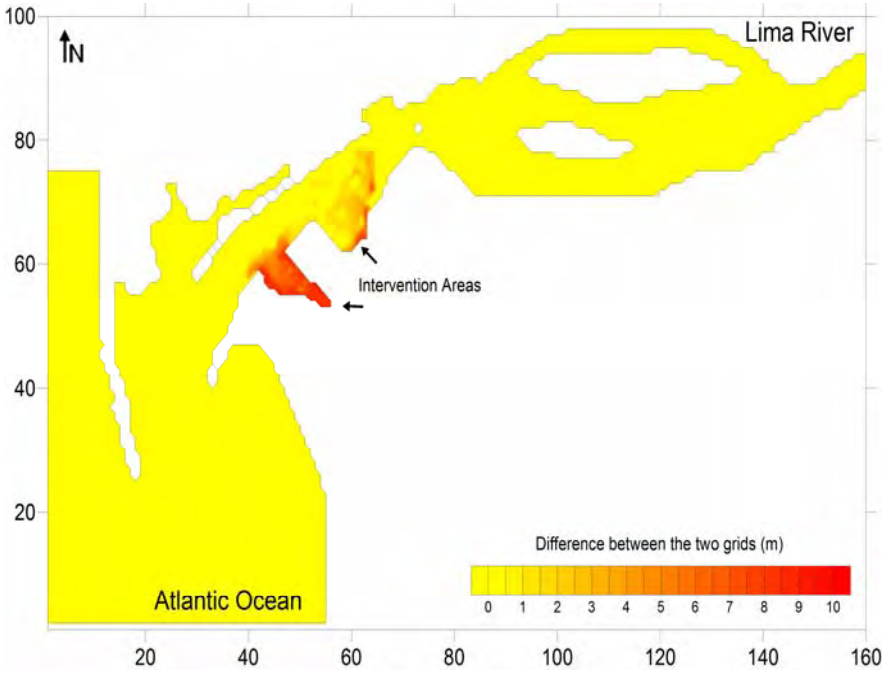

Fig. 98. Changes introduced to the bathymetry

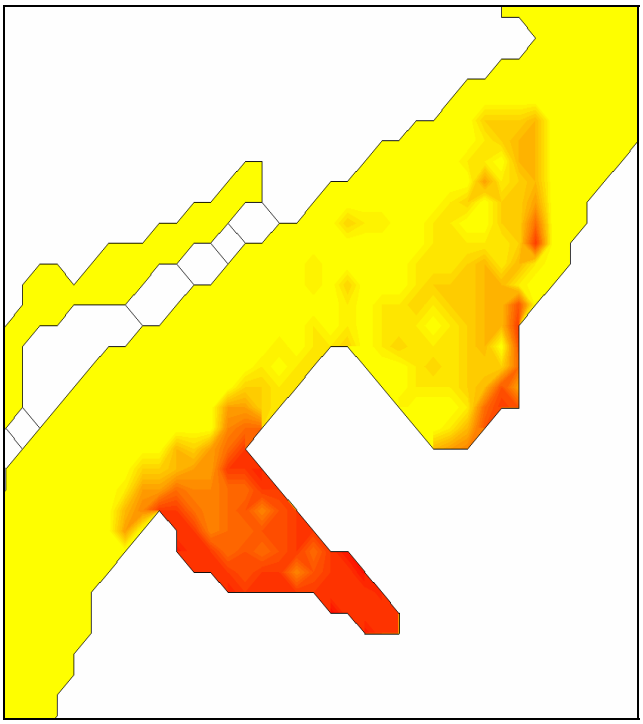

Fig. 99. Close up of the affected area

After running the model with the different boundary conditions and both grids, the results show that there is no significant impact to the estuary hydrodynamics resulting from the proposed dredging works and berth construction. Plots of the model-predicted sea surface elevation time series were compared for the two different model grids with no remarkable discrepancies.

Tidal currents were assessed for *u* and *v* components, being almost coincident for both grids with the exception of station C, where the most significant changes to the bathymetry occur (Fig. 98). Nevertheless these differences must take into account the fact that the model results are related to the mean value over the vertical and over a horizontal spatial domain corresponding to the grid size (40mX40m in this case). Station D is shown for control purposes since no bathymetric changes were introduced on this area.

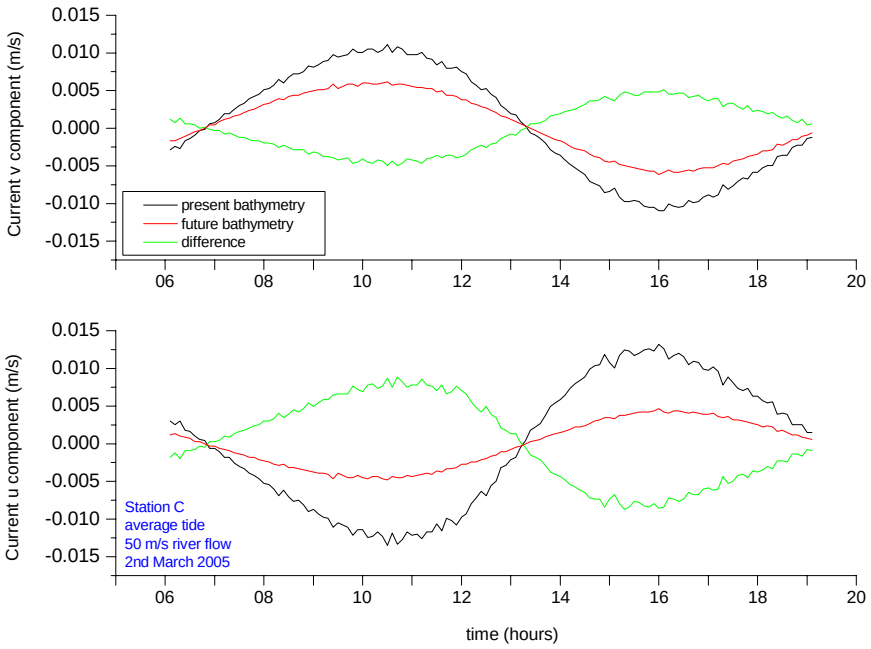

Fig. 100. Current u and v components comparison between present and future bathymetry for station C, forced with average tide and 50 m^3s^{-1} river flow.

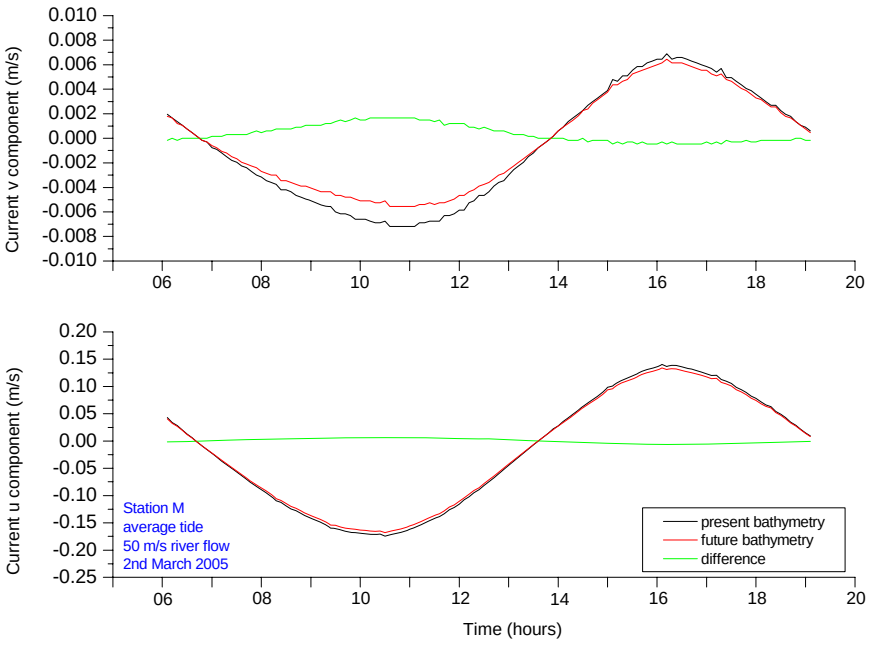

Fig. 101. Current u and v components comparison between present and future bathymetry for station M forced with average tide and 50 m^3s^{-1} river flow.

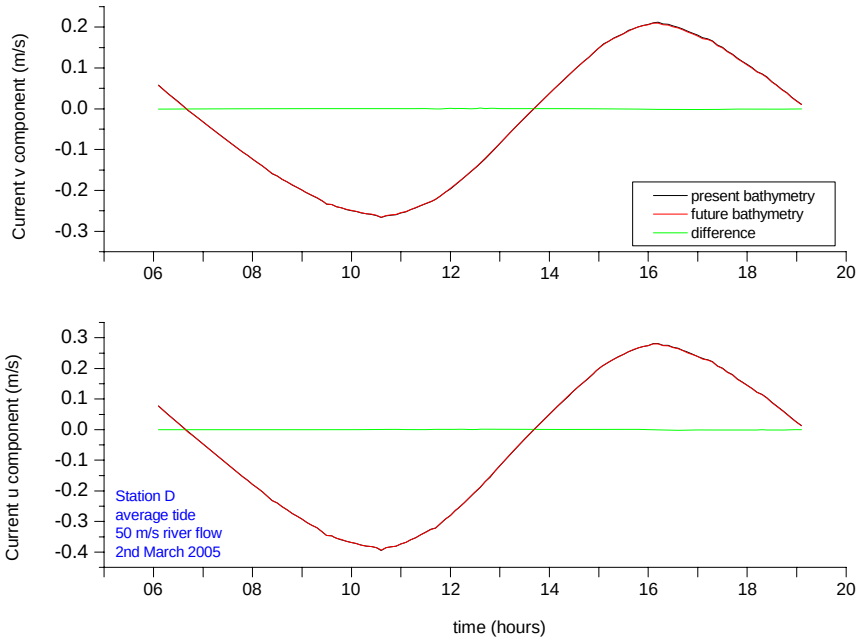

Fig. 102. Current u and v components comparison between present and future bathymetry for stations D forced with average tide and 50 m^3s^{-1} river flow.

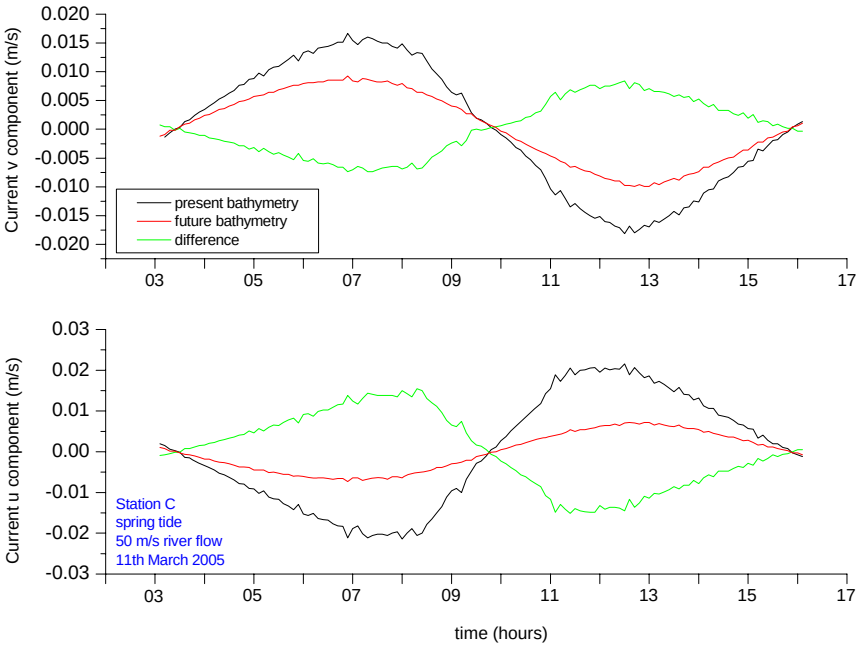

Fig. 103. Current u and v components comparison between present and future bathymetry for station C, forced with spring tide and 50 m^3s^{-1} river flow.

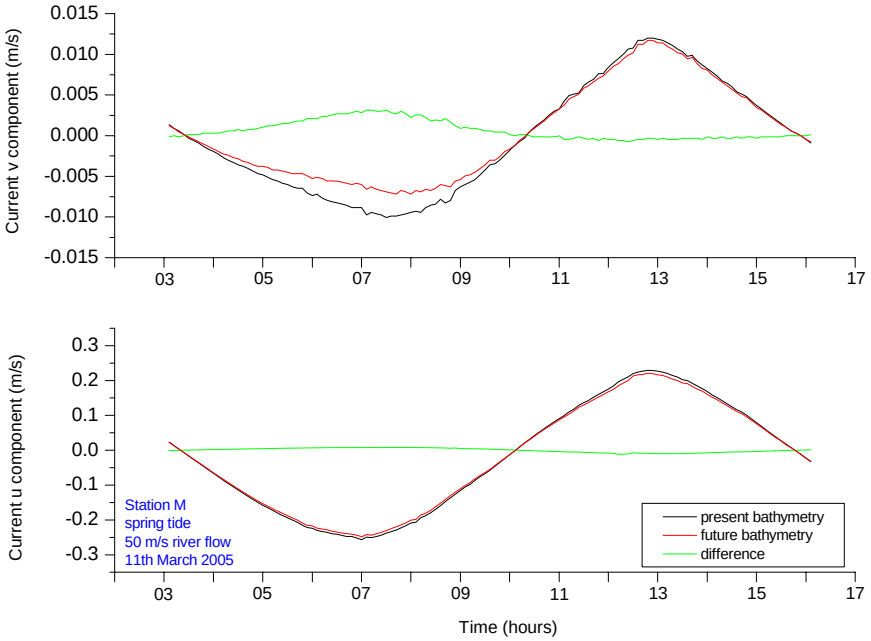

Fig. 104. Current u and v components comparison between present and future bathymetry for station M forced with spring tide and 50 m^3s^{-1} river flow.

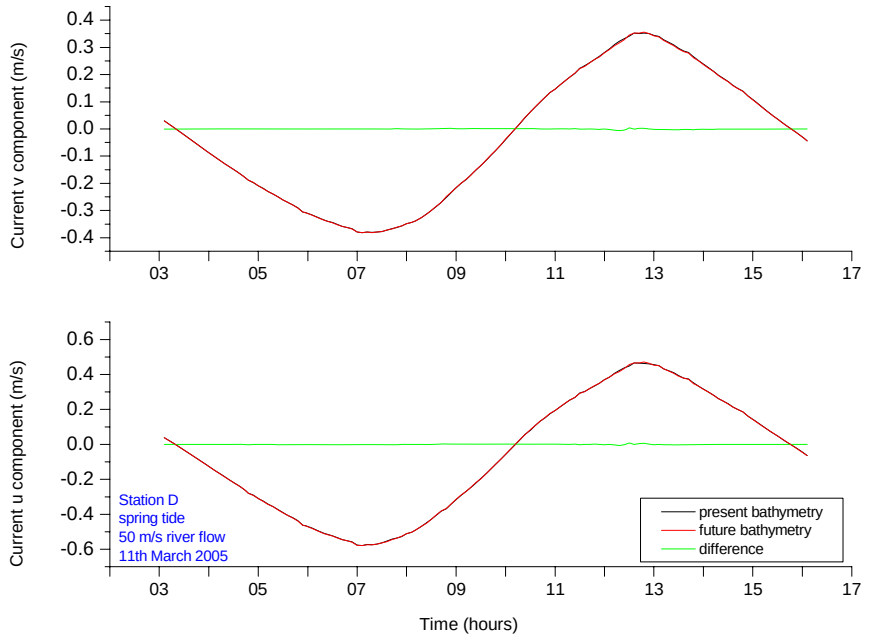

Fig. 105. Current u and v components comparison between present and future bathymetry for stations D forced with spring tide and 50 m^3s^{-1} river flow.

5.6. Using the hydrodynamic model to establish the relationship between river flow and tidal prism

Since the salinity field data collected is limited and restricted to a certain period of river flow and tidal regime, it was found useful to use the hydrodynamic model to compute the tidal prism at the mouth of the estuary and then compare to diverse river flows in order to ascertain the inherent ratio.

The tidal prism is often referred to as the volume of water exchanged between a lagoon or estuary and the open sea in the course of a complete tidal cycle, or as the volume of water between high tide and low tide. Within the scope of this work, and since the purpose was to establish the river flow/tidal input ratio, the tidal prism referred to hereinafter relates to the volume of sea water entering the estuary during a flood tide.

The cross sectional area considered for the study was the port entrance, between breakwaters. All grid cells contained in this alignment were used to calculate the tidal prism (Fig. 106 and Table 17).

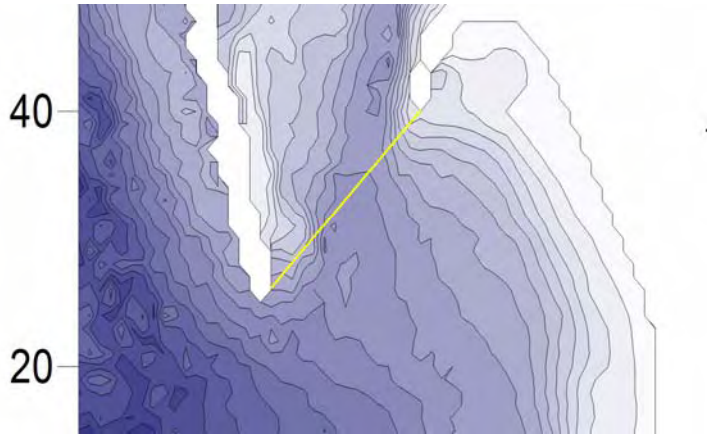

Fig. 106. Alignment used for tidal prism calculation

	st1	st2	st3	st4	st5	st6	st7	st8	st9	st10	st11	st12	st13	st14	st15
x	19	20	21	22	23	24	25	26	27	28	29	30	31	32	33
y	29	30	31	32	32	33	34	35	36	37	38	39	40	41	42
z_0	4.21	2.99	2.87	4.34	6.72	7.68	7.99	7.97	7.70	7.55	7.74	6.80	3.40	1.72	1.50

Table 17. Virtual stations between breakwaters (grid coordinates and depth)

The model was set to run with a 3 minutes temporal resolution and was forced at the West open boundary with a neap, average and spring tide as well as the previous used river flows at the East boundary (4 m^3s^{-1}, 50 m^3s^{-1}, 100 m^3s^{-1} and 200 m^3s^{-1}.).

Depth averaged velocities were computed for every single cell, for every 3 minutes period, as well as the sea surface elevations, for the flood periods.

For the neap flood tide the period between 16h45m and 22h36m of the 19th March 2005 was used, for the average tide the 2nd of March 2005 between 00h45m and 06h39m and for the spring tide the period between 09h51m and 15h42m of the 11th March 2005 was used.

The salt water input from the tide into the estuary was found to be varying between 3.7 X 10^6 m^3 for a neap tide with a tidal range of about 1.07 m and 12.6 X10^6 m^3 for a spring tide with a tidal range of about 3.07 m. An average flood volume of 8.9 X 10^6 m^3 was found for a tidal range of about 2.20 m, *i.e.*, an average tide.

Given that the river flow is continuously shifting, thus affecting the ability to establish its contribution to the stratification, only the extreme values of river discharge and tide input to the estuary were considered. It is important to note that the obtained classifications are merely stages on a continuous sequence that will be dominated by the river flow which causes an inflow of buoyancy that tends to maintain stratification, and the tidal flow, which, because of the friction, causes mixing [Dyer, 1997].

Simmons [1955], cited by Dyer [1997], found that when the flow ratio (the ratio of river flow per tidal cycle to the tidal prism) is 1.0 or greater, the estuary is highly stratified. When the flow ratio is about 0.25 the estuary is partially mixed and when it is less than 0.1 it is well mixed.

The model obtained values (Table 18) show, as it would be expected, a range of diverse classifications, dependent on the river discharge and tidal regime. Thus, considering the extreme situations, for a low river discharge (4 m^3s^{-1}) and a spring tide the estuary can be considered well mixed (0.007 ratio). For a high river discharge (100 m^3s^{-1}) and a neap tide the estuary can't still be classified as highly stratified although the values are above the partially mixed scenario (0.58 ratio).

The average tide and the average river discharge (50 m^3s^{-1}) results in a ratio of 0.12, which although within the partially mixed classification, is close to the well mixed range.

For maximum river discharge of 200 m^3s^{-1} and neap tides conditions, the ratio falls within the highly stratified classification, with a ratio of 1.05, although it must be considered that these river flows are anthropogenic in its origin, being only experienced with high turbinated dam flow.

	river flow			
tide	4 m^3s^{-1}	50 m^3s^{-1}	100 m^3s^{-1}	200 m^3s^{-1}
neap	0.023	0.291	0.582	1.048
average	0.010	0.122	0.243	0.438
spring	0.007	0.086	0.171	0.308

Table 18. Summary of river flow/tide input ratios.

The aim of this section was not to definitely categorize the estuary on its salinity structure as this would entail a

comprehensive field campaign data collection. Also, it is a known fact that estuary classification can change even at very short time scales. The purpose was to compute the tidal prism and relate it to diverse river discharge regimes, showing the usefulness of the numerical hydrodynamic model for different purposes.

5.7. Lagrangian transport of particles

Once the hydrodynamic model is fully operational it can provide the basis for the coupling with other models such as water quality and transport of particles.

One of the aims of this work was to study the dispersion of particles released at specific stations, chosen by its relevance.

Lagrangian modelling constitutes an appropriate and extremely useful tool for the study of dispersion processes in coastal waters, estuaries and lagoons. It allows the analysis of dispersion of water masses, represented as passive particles, and estimation of residence times at a low computational cost compared to Eulerian models [Dias, 2001].

The main advantage of a fully Lagrangian formulation over Eulerian transport models is its higher accuracy in describing localized emission spots thus becoming well suited to problems in which high concentration gradients are involved, since numerical diffusion is not introduced.

Lagrangian models, thus, are very useful predictive tools for the assessment of contaminated areas after accidental releases of pollution, for studying the transport of estuarine dependent planktonic species, for the calculation of residence times and overall study of transport properties.

This has led to a wide employment of these models on the study of the transport of passive particles in coastal areas, with such different purposes as the pollution dispersion in A Coruña and Vigo Rias [Gomez-Gesteira *et al.*, 1999], transport of particles in Ria de Aveiro Lagoon [Dias *et al.*, 2001], tidal transport and dispersal of marine toxic microalgae [Cerejo and Dias, 2006], residence time for suspended particulate matter in Ria de Aveiro

[Dias and Rocha, 2007] and numerical modelling of fish eggs dispersion at the Patos Lagoon estuary [Martins *et al.*, 2007].

The particle tracking model used throughout all simulations within this work and presented below, was developed by Dias [2001] and is coupled to the previously calibrated and validated hydrodynamic model.

A Lagrangian approach was chosen for computing the two-dimensional trajectories of the simulated particles, solving the equation at each time step:

$$X_i(x_0, y_0)^{n+1} = X_i(x_0, y_0)^n + \int_{t_0+n\Delta t}^{t_0+(n+1)\Delta t} u_i(x, y, t)dt \qquad (9)$$

$X_i(x_0, y_0)^{n+1}$ is the position at the instant *n+1* of the particle released at the point $X_i(x_0, y_0)^0$. The time integral is computed using a fourth-order Runge-Kutta scheme:

$$K_{1i} = \Delta t \ \text{x} \ u_i[t, X_i(x_0, y_0)^n] \qquad (10)$$

$$K_{2i} = \Delta t \ \text{x} \ u_i[t + \frac{\Delta t}{2}, X_i(x_0, y_0)^n + \frac{K_{1i}}{2} \qquad (11)$$

$$K_{3i} = \Delta t \ \text{x} \ u_i[t + \frac{\Delta t}{2}, X_i(x_0, y_0)^n + \frac{K_{2i}}{2} \qquad (12)$$

$$K_4 = \Delta t \ \text{x} \ u_i[t + \Delta t, X_i(x_0, y_0)^n + K_{3i} \qquad (13)$$

$$X_i(x_0, y_0)^{n+1} = X_i(x_0, y_0)^n + \frac{K_{1i}}{6} + \frac{K_{2i}}{3} + \frac{K_{3i}}{3} + \frac{K_{4i}}{6} \qquad (14)$$

where $X_i(x_0, y_0)^{n+1}$ represents the new location of a particle that is advected from its previous position $X_i(x_0, y_0)^n$ by the velocity $u_i = (u_i, v_i)$ in a time interval Δt, and K_{ji} represents the Runge-Kutta coefficients.

The implementation of the above model is straightforward, provided that a velocity field, as the one simulated by the two-dimensional hydrodynamic model, is available [Dias *et al.*, 2001].

The implicit assumption made in this section of the work is that particles distribution is dictated primarily by passive advection within the 2D flow field [Dias *et al.*, 2003], although in reality particles may move in response to additional processes such as diffusion, dissolution or aggregation and deposition.

This model was not validated specifically to the Lima estuary although its accuracy was tested by advecting a particle in a well-known velocity field typical of Ria de Aveiro [Dias *et al.*, 2001], with the computed particle trajectory being compared with the trajectory determined by solving the analytical equations. Within that domain the model results showed a good accuracy, clearly reproducing the expected particle trajectory.

Given that the lagrangian simulations in this study are related to dimensionless passive particles whose distribution is forced by the transport induced by the currents, and that the coupled hydrodynamic model for the Lima estuary was thoroughly tested, it was assumed that the Lagrangian model would be representing the particles tracks with acceptable accuracy.

For this study two main simulations were carried out. The first is related to a single particle tracking released on two different stations and the second is related to continuous emission spots localized at four different stations, placed at critical areas to simulate pollution events.

5.7.1. Particle tracking

An average tide with a tidal range of about 2.00 m and a steady river flow of 50 m^3s^{-1} were the chosen conditions for all simulations, with the particles being released at High Water (beginning of the ebb tide) and Low Water (beginning of the flood tide). A one day spin up period of the hydrodynamic model was taken into account before the release.

For the particle tracking were chosen stations D and S, the areas where, according to the hydrodynamic model, the maximum and minimum current speeds are attained, respectively (Fig. 107).

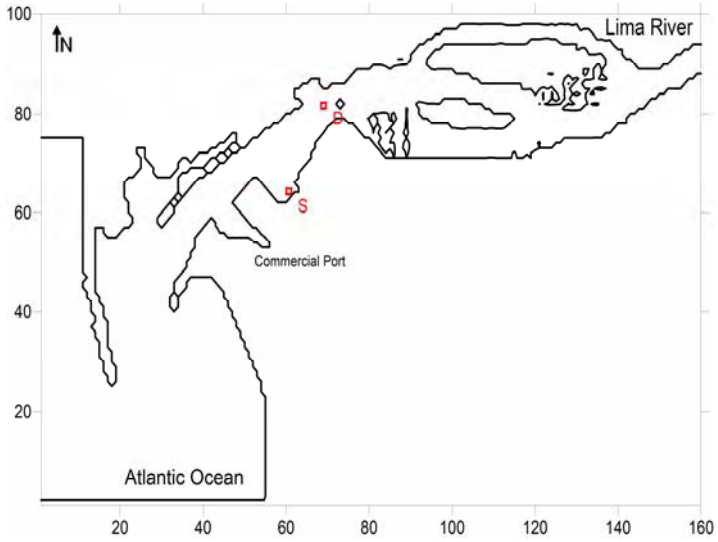

Fig. 107. Location of D and S stations.

The first release was performed at 06h45m of the 2nd of March 2005, time of High Water, on both stations (Fig 108).

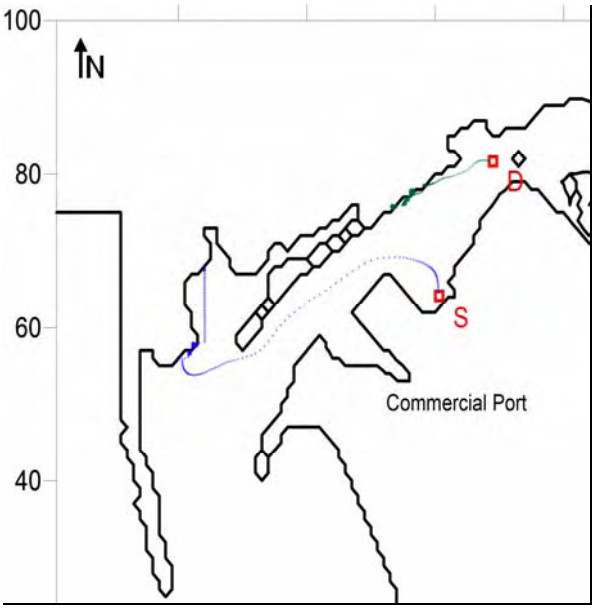

Fig. 108. Particle tracking after release at HW.

Against what was firstly anticipated, the particle released at station S (in blue), where the current is almost negligible, took a longer path than the particle released at station D (in green) where the higher currents are observed. This is because the particle released at station D very soon ran against the solid land boundary while the particle released at station S, although for the first hours didn't move much (see the closeness of the track symbol), after reaching the main channel axis the speed dramatically increased, taking the particle up to the shipyard basin.

The particles were then released from the same stations at the beginning of the flood tide, at 00h30m of the 2nd march 2005 (Fig. 109).

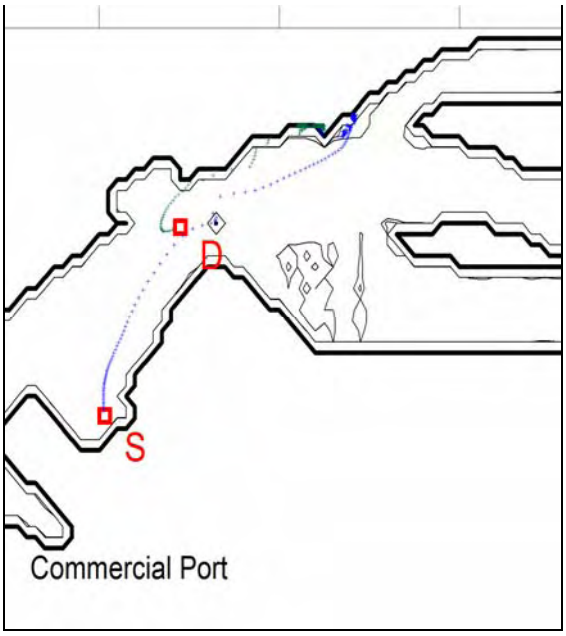

Fig. 109. Particle tracking after release at LW.

In this scenario the particle released at station D (in green) is again rapidly pushed towards the land boundary while the particle released at station S (in blue) manages to pass the bridge area and through the first reaches of the upper estuary.

5.7.2. Localized emission spots

In order to simulate the continuous emission of pollutants in certain areas of the commercial port, four stations (*W*, *X*, *Y* and *Z*) were defined considering the probability of a pollution event (Fig 110).

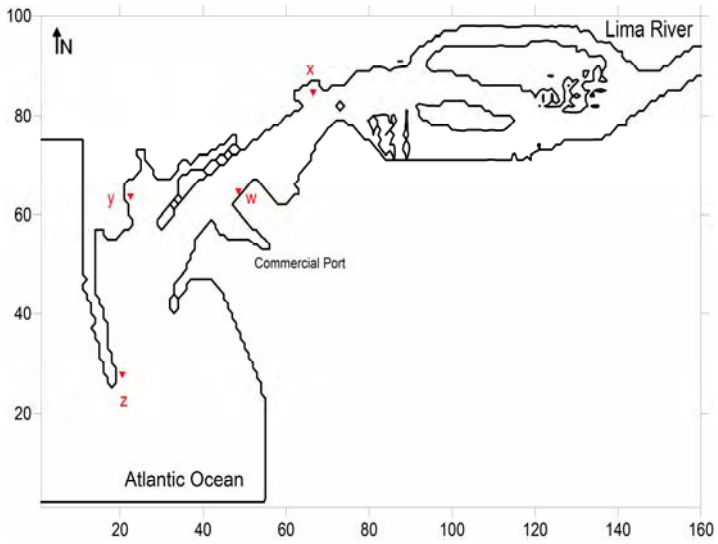

Fig. 110. Localization of stations for continuous emissions.

Station *X* is located inside the harbour marina, where a gasoline pump supplies the recreational craft. Station *W* is the oil terminal of the commercial harbour, where tankers regularly discharge. Station *Y* is located at the shipyard basin, at the berth where repairs and tests to ships are performed. Station *Z* is adjacent to the West breakwater, where the probability of a ship running aground with subsequent leakage is higher than the rest of the domain.

The chosen conditions were the same as for the particle tracking section, *i.e.*, an average tide and a steady river flow of 50 m^3s^{-1}, with the emissions starting at HW and LW and a one day spin up period allowed on the hydrodynamic model.

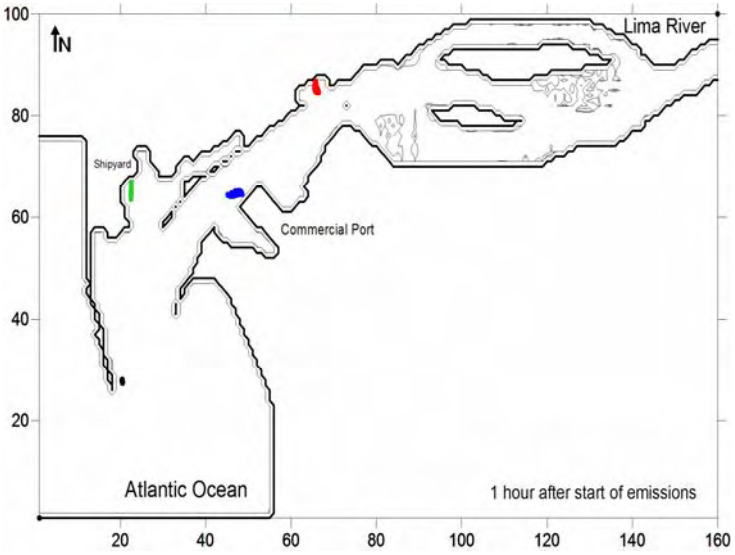

Fig. 111. Continuous emission 1 hour since release on HW.

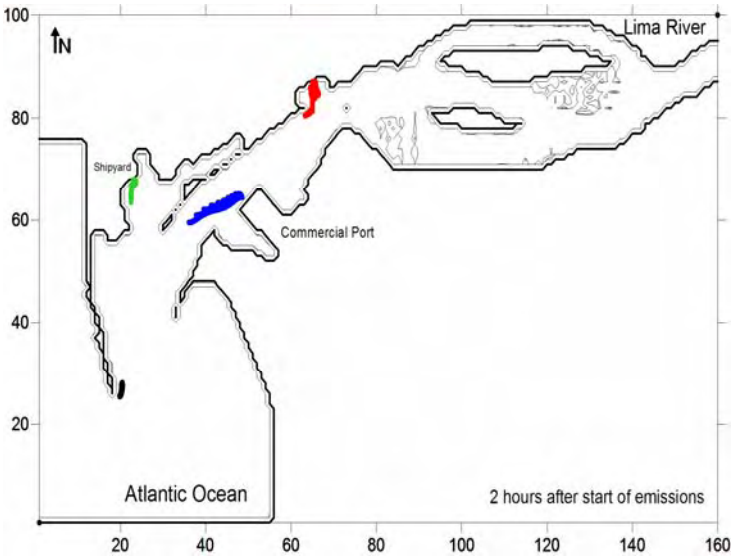

Fig. 112. Continuous emission 2 hours since release on HW.

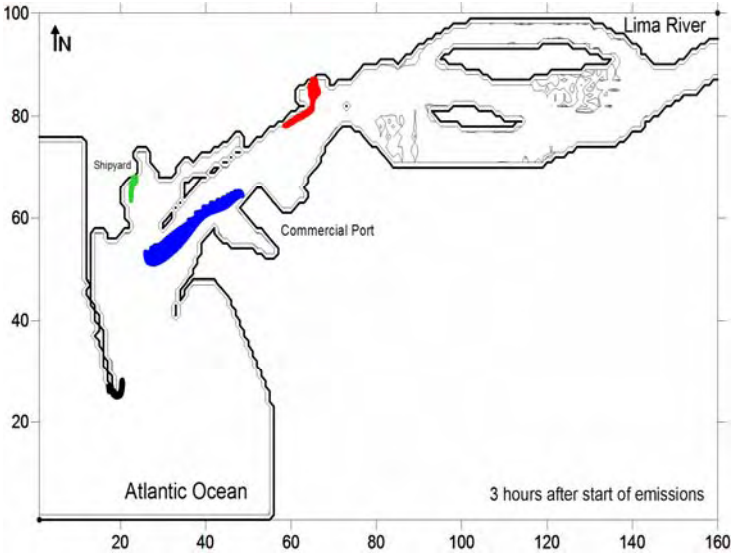

Fig. 113. Continuous emission 3 hours since release on HW.

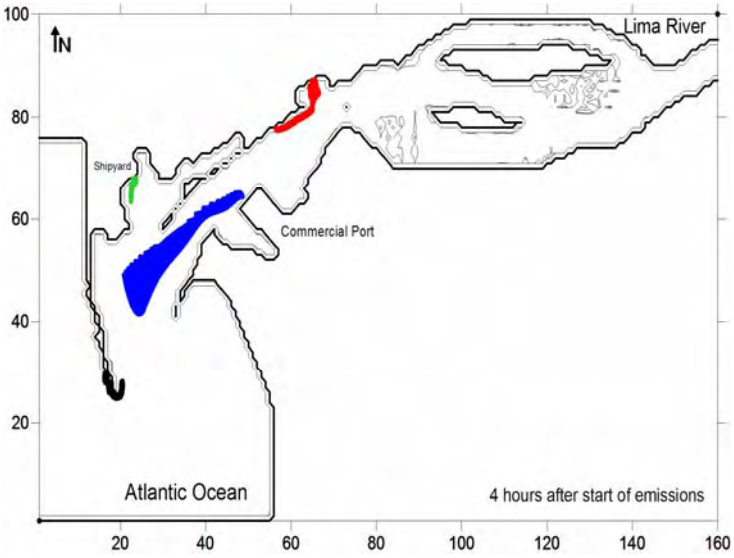

Fig. 114. Continuous emission 4 hours since release on HW.

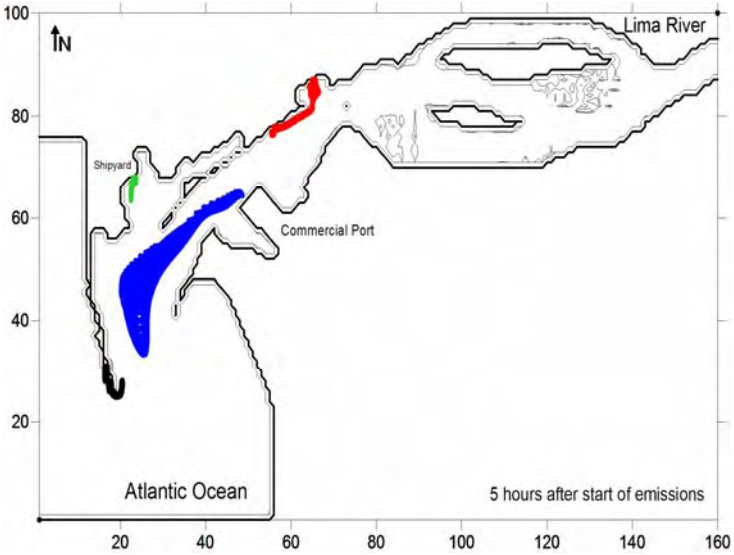

Fig. 115. Continuous emission 5 hours since release on HW.

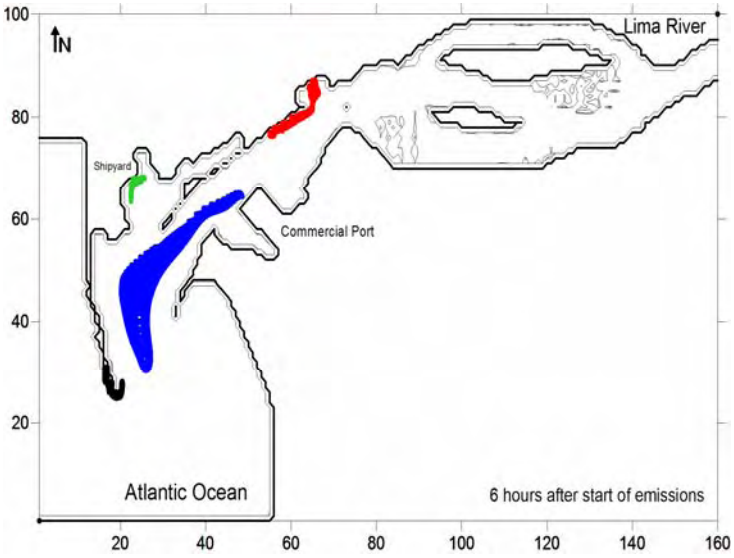

Fig. 116. Continuous emission 6 hours since release on HW.

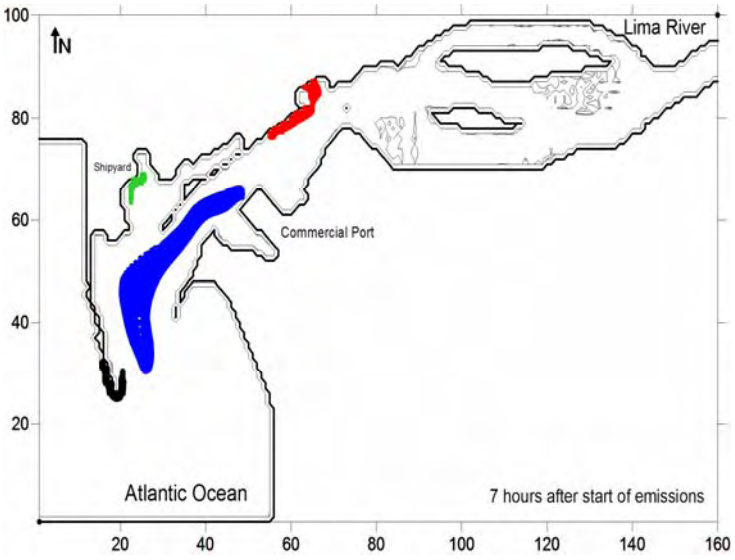

Fig. 117. Continuous emission 6 hours since release on HW.

From the graphical plots (Fig. 111 through Fig. 117) of the areas affected by the continuous emission of particles is quite clear the influence of the tidal currents on the path followed. Since station *W* is positioned closer to the channel axis, the emitted particles are flushed downstream up to the port entrance. 7 hours after the emission started there are particles from station *W* close to station *z*. The particles emitted by station *Y* remained inside the basin as the currents here are very weak. At station *Z* the particles are sent outside the port and remain against the breakwater. The emission of particles from the station *X* will affect the entire marina as well as the North margin of the channel, downstream of the marina.

These plots show that a pollution incidence would have a more severe consequence (from the total affected area point of view) if happening at the oil terminal, thus emphasizing the importance of rapid containment of an eventual leakage.

The model was then re-run with all same parameters remaining the same except for the time of the start of the emissions which was changed to the time of LW, the beginning of the flood tide.

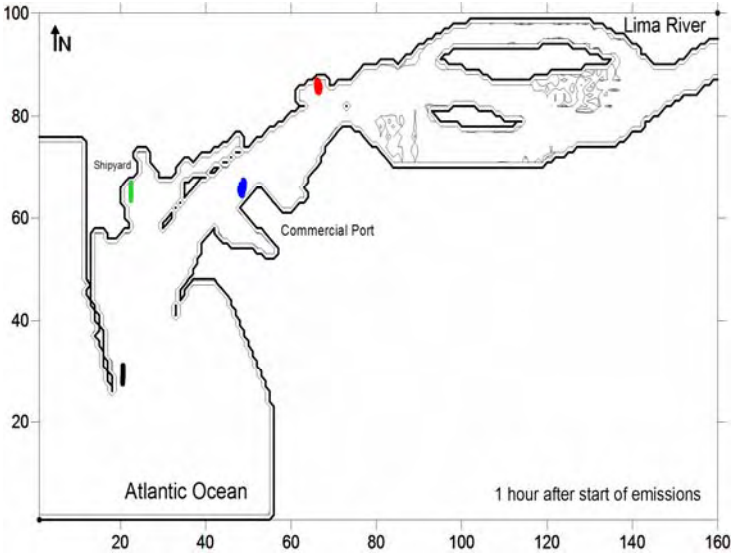

Fig. 118. Continuous emission 1 hour since release on LW.

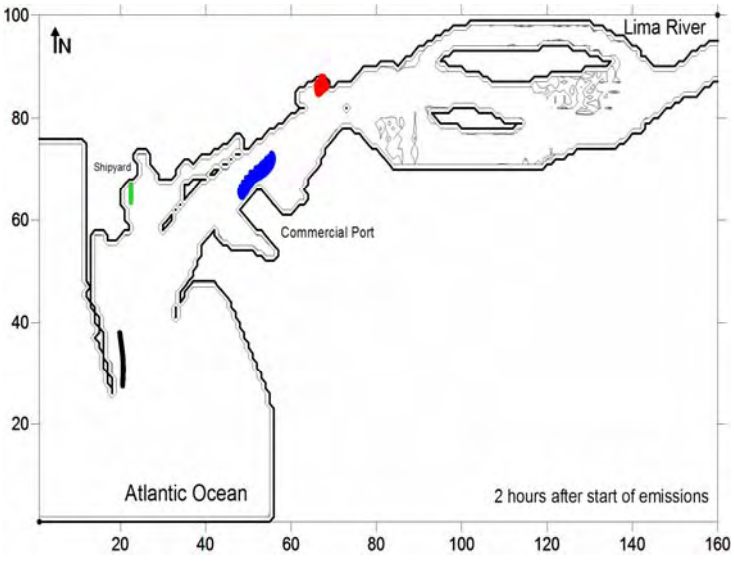

Fig. 119. Continuous emission 2 hours since release on LW.

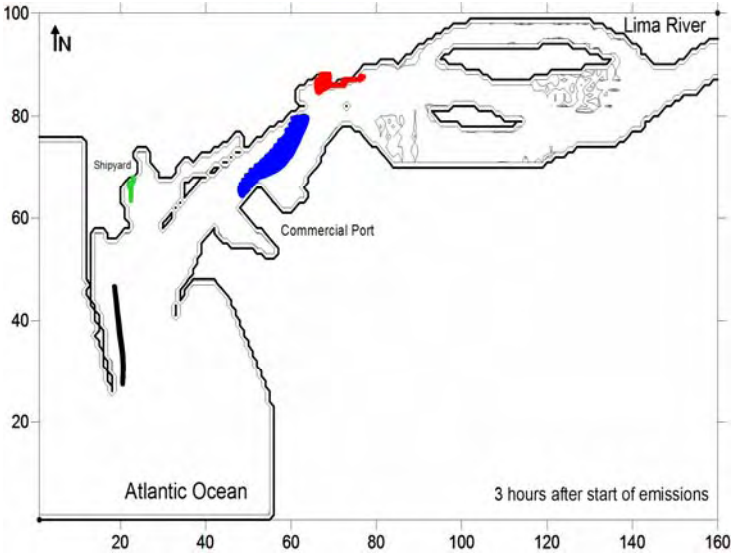

Fig. 120. Continuous emission 3 hours since release on LW.

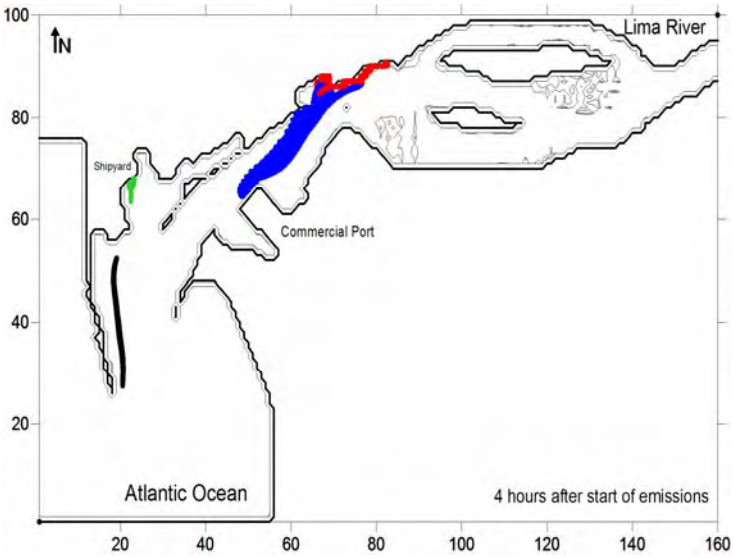

Fig. 121. Continuous emission 4 hours since release on LW.

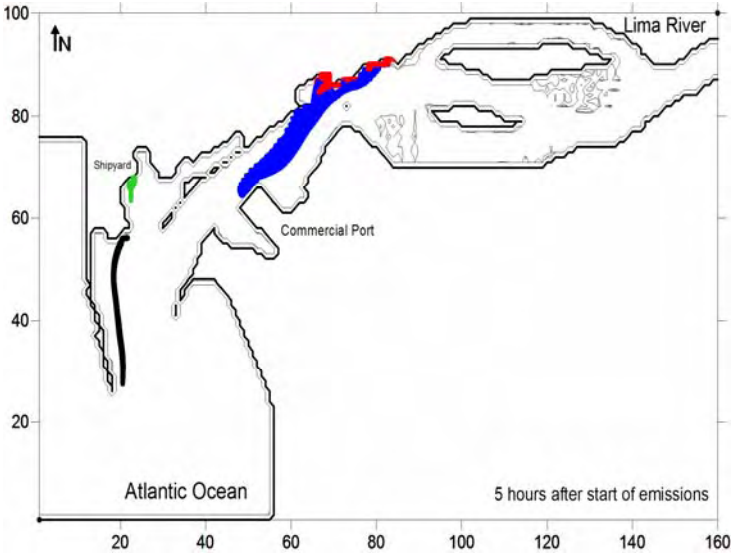

Fig. 122. Continuous emission 5 hours since release on LW.

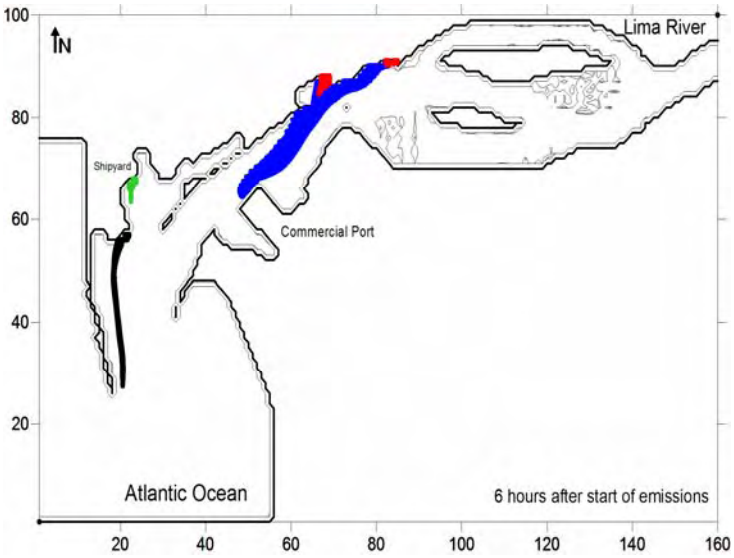

Fig. 123. Continuous emission 6 hours since release on LW.

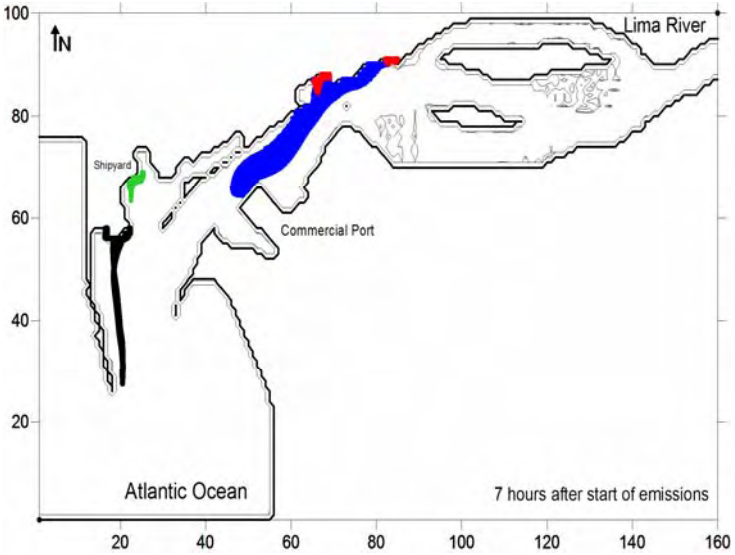

Fig. 124. Continuous emission 7 hours since release on LW.

The graphical comparison of the affected areas for the situation when the emission starts at LW (Fig. 118 through Fig. 124) shows again the preponderance of the station *W* whose emission sweeps all the commercial harbour area up to the beginning of the upper reaches of the estuary. A common feature to the scenario where the emission starts at HW is that the South margin is not affected even though the emission has there its origin. Station *X* keeps the emission in the marina area until 2 hours after the release and then the particles spread through the North margin. The particles emitted by the station located at the shipyard berth (station *Y*) are kept within the yard basin and the station located at the port entrance is heavily affected by the tidal stream, with the particles being pushed North, inside the port, while the tide is flooding, until they reach the Bugio Breakwater.

Again, taking into account these results, it is important to emphasize the significant impact that a continuous emission of a certain pollutant can have in the estuary, even if only advective transport is being considered.

This section of this study demonstrates that, once the hydrodynamic model is fully operational, it is worth exploring all

its potentialities, in this case by coupling a Lagrangian model. The results of the particle tracking model may constitute an interesting tool on the study of pollution events within a port area and assist on the prevention and containment decision process (for example, where to store the pollution barriers inside the port).

5.8. Propagation of Harmonic Constituents within the estuary

Even though it has been previously determined that no appreciable distortion to the tide was observed on its propagation upstream, no information about the tidal harmonic constituents independent behaviour was available, with the exception of the tidal gauge station.

The model allows for a graphical comparison of the HC propagation within the estuary, by coupling a sub-routine that performs harmonic analysis at every single grid cell of the domain, thus enabling the visualization of the amplitude and phase variation of a particular constituent.

For the harmonic analysis, the sea surface elevation time series of March 2005 was forced at the west boundary condition.

Although any harmonic constituent could be represented, depending only on the length of the sea surface elevation time series of the harmonic analysis, within the scope of this work, and taking into account the relatively small variations observed, it was decided to plot only the semidiurnal M_2, S_2 and N_2, the diurnal K_1, the shallow water lunar M_4 and the fortnightly lunisolar *MSF* (Figs. 125 to 134).

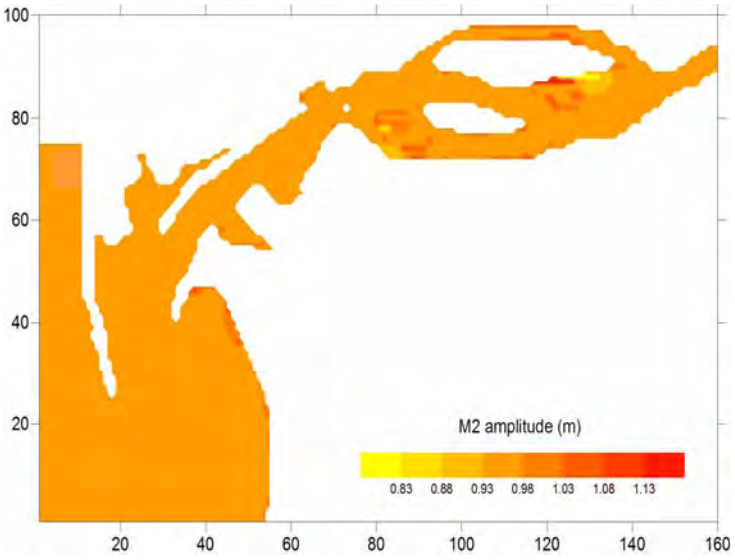

Fig. 125. M_2 amplitude.

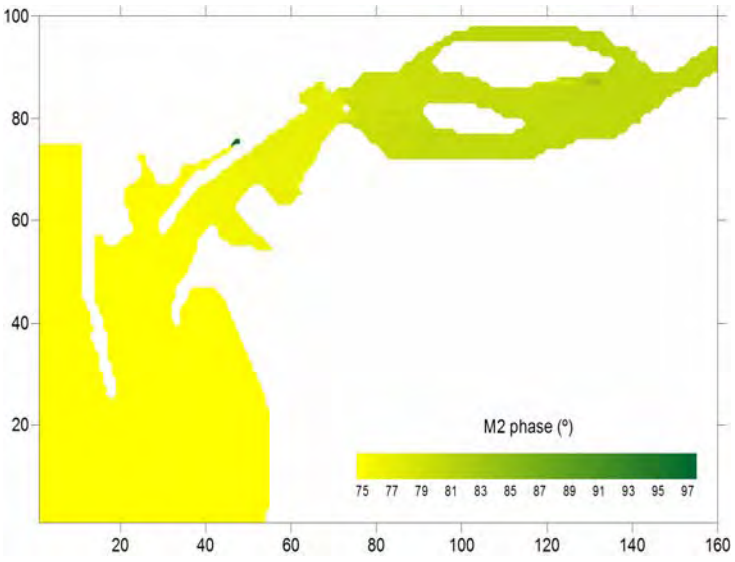

Fig. 126. M_2 phase.

The M_2 amplitude is almost constant throughout the estuary with minor variations only where the bathymetry is irregular or shallow (Fig. 125). The phase of this HC varies with progression upstream, showing about 5º increase on the upper reaches, comparing to the boundary condition, which represents about 10 minutes difference (Fig. 126).

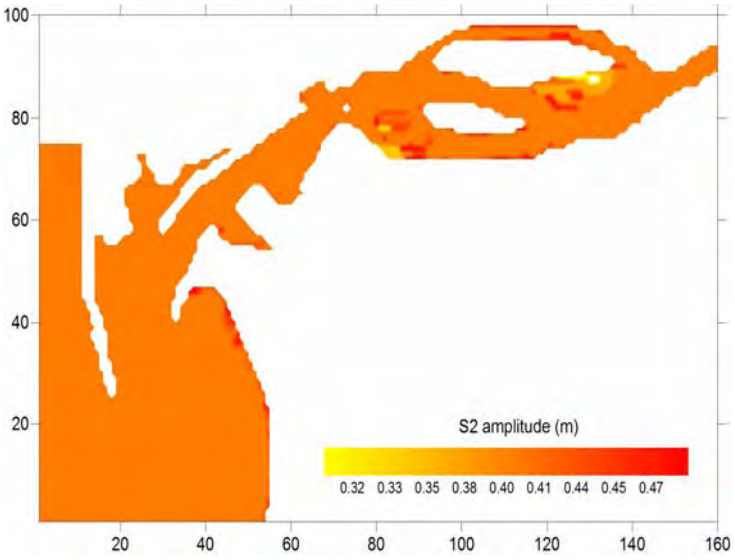

Fig. 127. S_2 amplitude.

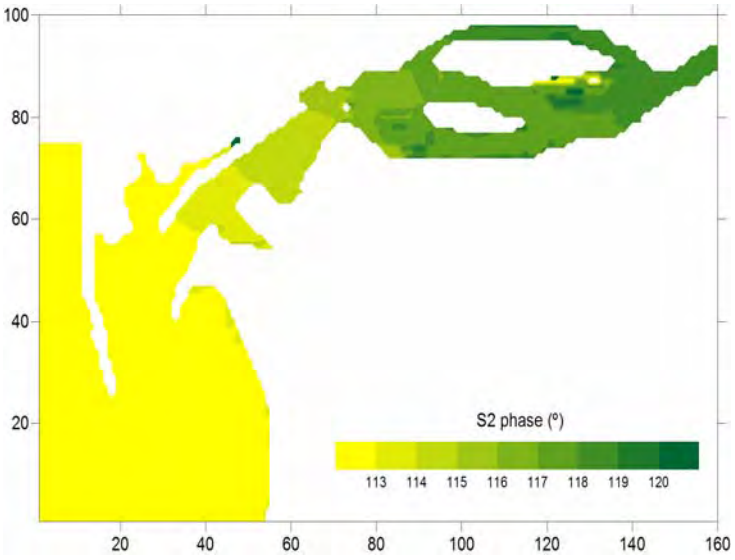

Fig. 128. S_2 phase.

The behaviour of the S_2 constituent is very similar to the M_2, both in amplitude and phase, with minor variations on the former and a progressive increase upstream on the latter (Figs. 127 and 128).

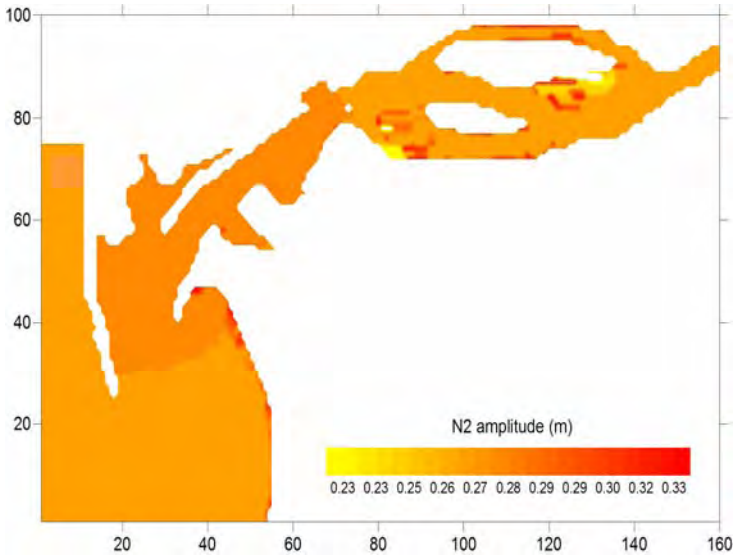

Fig. 129. N_2 amplitude.

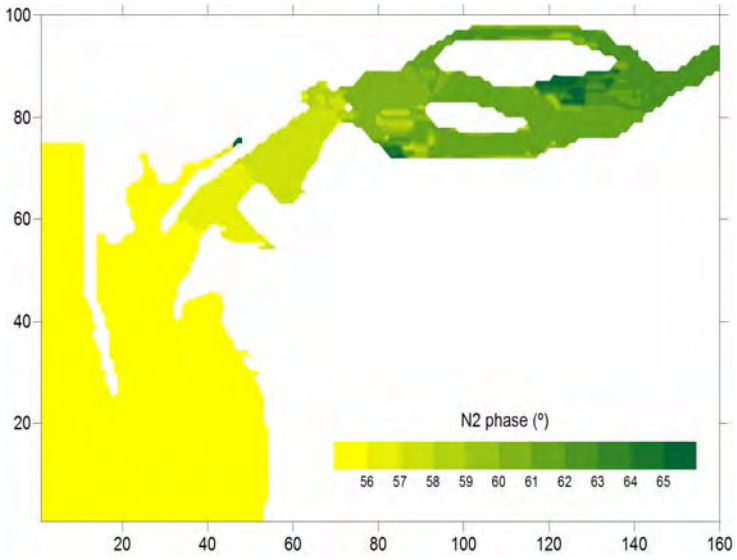

Fig. 130. N_2 phase.

The third most important HC, the semidiurnal N_2 has an analogous variation with M_2 and S_2, although the amplitude seems to increase slightly from the entrance to the port area, between breakwaters.

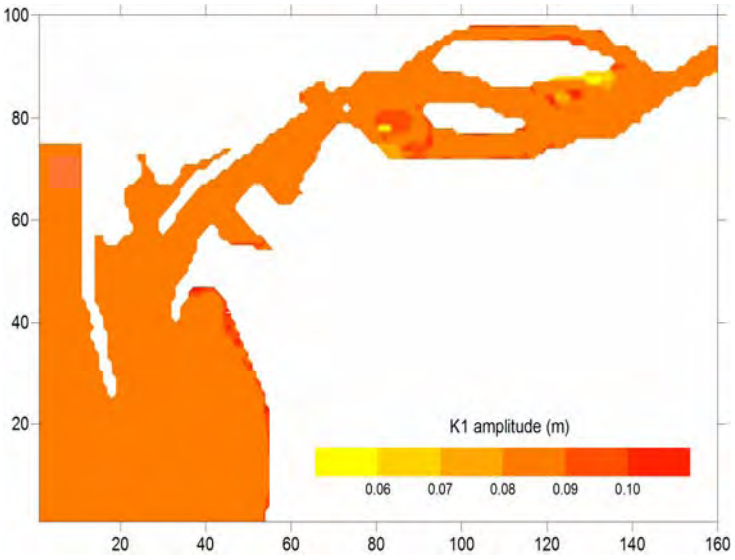

Fig. 131. K_1 amplitude.

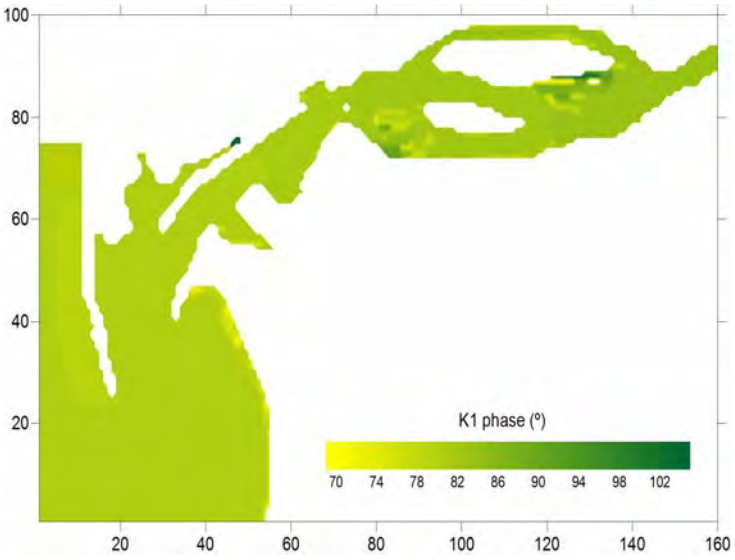

Fig. 132. K_1 phase.

The main diurnal component, K_1, has little or no variation throughout the grid, both in amplitude and in phase, with the exception of quite localized areas of extreme shallow water or irregularity of the bathymetry.

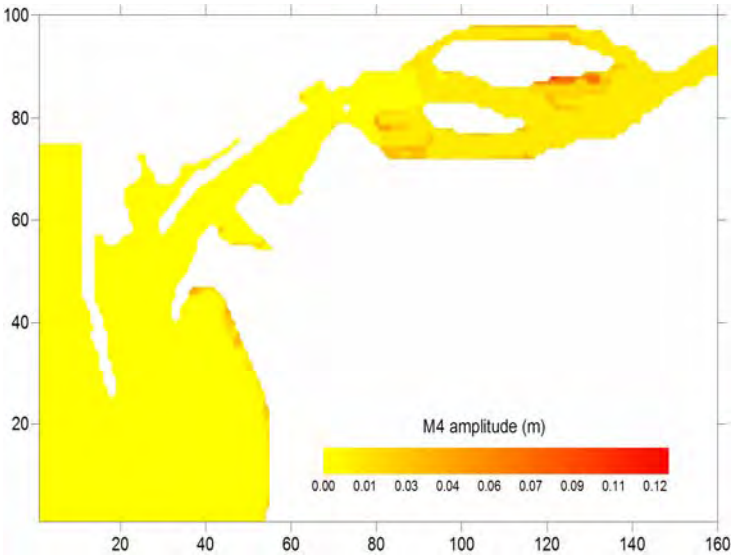

Fig. 133. M_4 amplitude.

The shallow water constituent M_4 is generated inside the domain thus the zero values at the West boundary. On the upper reaches of the estuary is noticeable a 2 to 3 cm overtide, as it would be expected, being this area the shallowest of the study area. The phase of the M_4 constituent has irrelevant variation with values within the error range of the harmonic analysis.

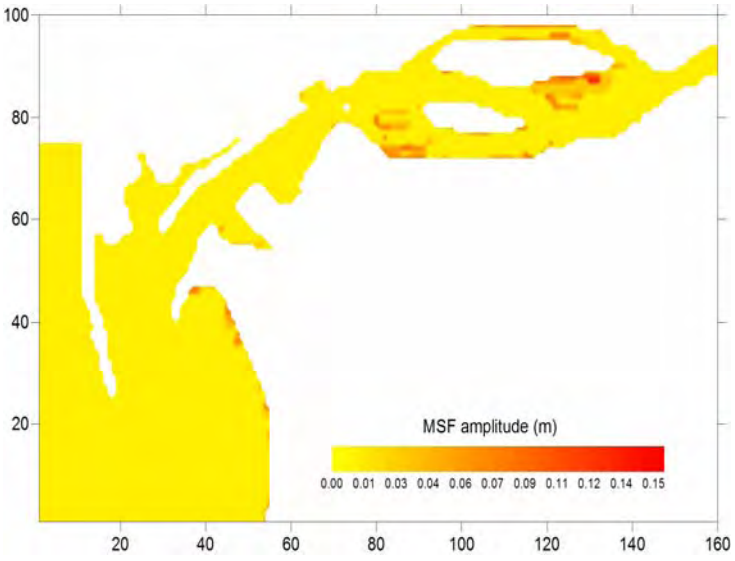

Fig. 134. *MSF* amplitude.

The lunisolar fortnightly constituent also has little variation except where shallow water or irregular bathymetry is found.

Even though both grids were used, *i.e.,* the grid representing the present situation of the bathymetry and the grid with alterations introduced by the forecasted dredging activities, the graphical plots of the observed differences in amplitude and phase showed negligible values within the range of the harmonic analysis error.

This behaviour corroborates the previous findings that the proposed alterations to the bathymetry have little or no influence on the tide behaviour and are only perceptible when the currents are analyzed on a spot station.

6. Conclusions

The general purpose of this work was to characterize and better understand the hydrodynamics of the lower reaches of the Lima estuary, namely within the commercial port area.

Although an empirical knowledge existed prior to the beginning of this study, inherent to a daily professional operation, several features were unknown due to the inexistence of proper data.

One of the main difficulties met was the lack of field data concerning the study area. This problem was partially solved by taking full advantage and exploring the most of the scarce available data and by conducting limited yet successful field campaigns at judiciously chosen spots.

The field work may be considered succeeded although limited by logistic difficulties. Future methodical and careful field campaign will be of the utmost importance to corroborate many of the achieved results in this study.

The numerical modelling studies were undertaken with great care, always bearing in mind the inherent limitations of model results. The calibration and validation of the hydrodynamic model was successful and its use, together with the field data collected, helped in contributing to an increase of the knowledge about this system.

The analysis of the occurrence of a storm surge event was performed by making a thorough meteorological assessment together with the tidal analysis, showing that these are inextricably linked and the consequences of the surge are dependent on both. This work showed that the magnitude of the surge can be about 0.70 m above forecasted tidal levels and the consequences are

dependent on the probability of this occurring at low water or high water of neap or spring tides.

An in-depth analysis to the flow regime of the Lima River was performed as this was considered essential towards the proper estuary classification as well as being one of the boundary conditions of the numerical model. This study shows that the river discharge is highly variable with flows ranging between 4 m^3s^{-1} and about 200 m^3s^{-1}, depending on the station of the year and, more important, on the Touvedo and Alto Lindoso power generating dams.

The estuary vertical structure was studied with field campaigns collecting data from vertical profiles at chosen spots of selected transects. Salinity and temperature data were processed with the results of the 4 transects showing that the estuary classification, from the salinity point of view, varies with the varying river flow and with the tidal spring-neaps cycle, ranging between a well mixed water column to a slight stratified condition, with a partially mixed condition most of the time.

Tidal currents were evaluated by processing data from moored currentmeters at two different locations, showing that the current magnitude is primarily dependent on the tidal neap-spring cycle and on the locations within the estuary. At certain areas, current speed can be twice the speed of other area at the same time. Maximum recorded currents were attained at a spring ebbing tide with 1.04 ms^{-1}.

A meticulous tidal harmonic analysis and spectral analysis was performed using a one year long sea surface elevation time series from the tidal gauge. This showed the clear dominance of the semidiurnal constituents, namely the $M_{2,}$ which is the most important for the port of Viana do Castelo with 1.04 m in amplitude and 77º.2 in phase. The relative importance of the shallow water and fortnightly constituents was also examined but these are not relevant.

A depth integrated 2D hydrodynamic model SIMSYS2D was successfully implemented. The numerical solution was presented and explained. The implementation stage implied a demanding work on the construction of the model grid, namely the bathymetry. Data was taken from port surveys and nautical charts. Interpolation techniques such as Kriging and Monte Carlo cubature method were used to achieve the final grid consisting in 160 cells in the *x*-direction and 100 cells in the *y*-direction, with each square cell measuring 40 m on the side.

The model was qualitatively calibrated using sea surface elevations for three stations within the study area and a quantitative assessment was performed using RMAE, RMS and Skill methods. Harmonic analysis was also completed for both observed and modelled results. The results show a good agreement between observed and modelled results.

The model was validated using a different set of sea surface elevation time series as well as with available current data for two stations and two different time periods. After the good results of the validation procedures the model was considered able to satisfactorily simulate the hydrodynamic processes occurring within Viana do Castelo port area, given the scope of this work.

The model was then set to run several simulations, namely tidal propagation upstream, study area horizontal structure of currents, comparison and quantification of currents for different stations, behaviour of the hydrodynamics with varying river flow, hydrodynamic changes introduced by alterations to the bathymetry, the computation of the river flow/tidal input ratio and the graphical plot of the harmonic constituents variation throughout the estuary.

Several interesting results were obtained from these simulations. There is a slight phase shift for two stations on the upper

reaches of the estuary, located on constricted channels. Differences can attain up to 0.12 m difference for the port entrance.

The horizontal structure of currents plots give an extremely valuable insight of the overall behaviour of the port hydrodynamics, allowing for an easy recognition of critical zones. Several different simulations were plotted, varying the tidal regime from extreme neap tides to extreme spring tides and also adjusting the river flows for 4 m^3s^{-1}, 50 m^3s^{-1}, 100 m^3s^{-1} and 200 m^3s^{-1}. The currents were then quantified and obtained values compared for different stations, whose location is important from the navigational point of view.

A different model grid was constructed taking into account the expected changes introduced by port expansion works and the model was run. Results were compared for different stations, showing that there are only minor changes to the study area hydrodynamics and these are confined to the area where the most dramatic changes occur.

The river flow/tidal prism ratio was computed in order to assist in the estuary classification, from the salinity structure point of view. Calculations were made for neap, average and spring tides as well as for the previously mentioned river flows. The results indicate a salt water input into the estuary on a flooding tide ranging between 3.7×10^6 m^3 for a neap tide and 12.6×10^6 m^3 for a spring tide. The results were compared with the rive input for the same period and show that the estuary entails a wide range of classification, being well mixed for spring tides and low river flows, partially mixed on most of the time and slightly stratified when high river discharge and neap tided occur.

A Lagrangian particle tracking model was also successfully coupled to the hydrodynamic model, allowing for the following of the path of individual particles released at certain stations within the

domain as well the simulation of continuous spot emissions and related affected areas.

It was found that once the hydrodynamic model is fully operational it is worth exploring all its potentialities. Care should be taken on the analysis of the coherence of the results and for this is extremely valuable an in-depth knowledge of the study are by the modeller.

All the aims established at the beginning of the work were fulfilled and even surpassed. Future research must put an emphasis on the collection of additional field data, namely longer SSE time series for a wider range of stations within the domain and salinity and temperature sampling for different stations, different tidal and river conditions and different seasons of the year.

7. References

Aanderaa Instruments Data Sheet D 328, May 2000. RCM9 MkII Recording Current Meter.

Canhanga, S., Dias, J. M., 2005. Tidal characteristics of Maputo Bay, Mozambique. Journal of Marine Systems 58, 83-97

Cerejo, M., Dias, J. M., 2007. Tidal transport and dispersal of marine toxic microalgae in a shallow, temperate coastal lagoon. Marine Environmental Research, 63, 313-340.

Cheng, R.T., Burau, J.R., Gartner, J.W., 1991. Interfacing data analysis and numerical modelling for tidal hydrodynamic phenomena. In: Parker, B.B. (Ed.), Tidal Hydrodynamics. John Wiley & Sons, New York, USA, 201-219.

Cressie, N., 1990. The Origins of Kriging. Mathematical Geology, 22, 239-252.

Debernard, J., Saetra, O., Roed, L.P., 2002. Future wind, wave and storm surge climate in the northern North Atlantic. Climate Research 23, 39-49.

Dias, J. M., 2001. Contribution to the study of the Ria de Aveiro hydrodynamics. PhD Thesis, University of Aveiro, Portugal. 288 pp.

Dias, J. M., Abrantes, I., Rocha F., 2007. Suspended particulate matter sources and residence time in a mesotidal lagoon. Journal of Coastal Research, 1034-1039

Dias, J.M., Fernandes, E.H., 2006. Tidal and subtidal propagation in two Atlantic estuaries: Patos lagoon (Brazil) and Ria de Aveiro lagoon (Portugal). Journal of Coastal Research SI39, 1423-1427.

Dias, J.M., Lopes, J.F., 2006. Implementation and assessment of hydrodynamic, salt and heat transport models: The case of Ria de Aveiro Lagoon (Portugal). Environmental Modelling & Software 21, 1-15.

Dias, J. M., Lopes, J. F., Dekeyser, I., 2001. Lagrangian Transport of Particles in Ria de Aveiro Lagoon, Portugal. Physics and Chemistry of the Earth, Part B, 26, Nº9, 721-727.

Dias, J. M., Lopes, J. F., Dekeyser, I., 2003. A numerical system to study the transport properties in the Ria de Aveiro lagoon. Ocean Dynamics 53, 220-231.

Dyer, K. R., 1997. Estuaries, a physical introduction. 2nd Edition. John Wiley & Sons Ltd. 195 pp.

Donnell, B.P., Letter, J.V., Teeter, A.M., 1991. The Atchfalaya River Delta; Report 11, Two Dimensional Modeling, Technical Report HL-82-15, US Army Engineer Waterways Experiment Station, Vicksburg, MS, 87 pp.

Fernandes, E.H.L., Dyer, K.R., Moller, O.O., Niencheski, L.F.H., 2002. The Patos Lagoon hydrodynamics during an El Niño event (1998). Continental Shelf Research 22, 1699-1713.

French, J.R., Clifford, N.J., 2000. Hydrodynamic modelling as a basis for explaining estuarine environmental dynamics: some computational and methodological issues. Hydrological Processes 14, 2089-2108.

Giszas, H., 1984. Mathematishe Simulation des Verhaltens von Grobschiffen als Planungshilfe im Hafenbau. HANSA, Vol. 14.

Gomez-Gesteira, M., Montero, P., Prego, R., Taboada, J. J., Leitão, P., Ruiz-Villareal, M., Neves, R. and Perez-Villar, V, 1999. A two-dimensional particle-tracking model for pollution dispersion in A Coruña and Vigo Rias (NW Spain). Oceanologica Acta, 22, 2, 167-177.

Guibas, L., and J. Stolfi, 1985. Primitives for the Manipulation of General Subdivisions and the Computation of Voronoi Diagrams, ACM *Transactions on Graphics*, 4.2, 74-123.

Hsu, M.H., Kuo, A.Y., Kuo, J.T., Liu, W.C., 1999. Procedure to calibrate and verify numerical models of estuarine hydrodynamics. Journal of Hydraulic Engineering 125 (2), 166-182.

IPCC, 2001. Climate Change 2001: The Scientific Basis. Contribution of Working Group I to the Third Assessment Report of the Intergovernmental Panel on Climate Change [Houghton, J.T.,Y. Ding, D.J. Griggs, M. Noguer, P.J. van der Linden, X. Dai, K. Maskell, and C.A. Johnson (eds.)]. Cambridge University Press, Cambridge, United Kingdom and New York, NY, USA, 881 pp.

Leendertse, J.J., 1987. Aspects of SIMSYS2D. A System for Two-Dimensional Flow Computation. R-3572-USGS, Rand Corporation. 80 pp.

Leendertse, J.J., Gritton, E.C., 1971. A water quality simulation model for well mixed estuaries and coastal seas. Computation Procedures, R-708-NYC, vol II. The Rand Corporation, Santa Monica, California, 53 pp.

Lehfeldt, R., Milbradt P., Zyserman J., Barthel V., 2002. Proceedings of the 28th International Conference on Coastal Engineering 3, 3357-3369

Lin, B., Chandler-Wilde S., 1996. A depth-integrated 2D coastal and estuarine model with conformal boundary-fitted mesh generation. International Journal for Numerical Methods in Fluids, 23, 819-846.

LNEC, Laboratório Nacional de Engenharia Civil, 1969. Estudo em modelo reduzido das obras de melhoramento do porto de Viana do Castelo. Análise dos elementos de campo, construção e equipamento do modelo reduzido, 1º Relatório. Proc. 64/1/850. 85 pp.

Lopes, L.F.G., Cortes, R.M.V., Antunes do Carmo, J.S., Ferreira, T., 2001. Environmental Instream Flow Computation Downstream of Touvedo Dam – River Lima.

Lowe, J.A., Gregory, J.M., Flather, R.A., 2001. Changes in the occurrence of storm surges around the United Kingdom under a future climate scenario using a dynamic storm surge model driven by the Hadley Centre climate models. Climate Dynamics 18, 179-188.

Marta-Almeida, M., Dubert, J., 2006. The structure of tides in the Western Iberian region. Continental Shelf Research 26, 385-400.

Martin, J.L. and McCutcheon S.C., 1999. Hydrodynamics and Transport for Water Quality Modeling. Lewis Publishers. 794 pp.

Martins, I.M., Dias, J.M., Fernandes, E.H., Muelbert, J.H., 2007. Numerical modelling of fish eggs dispersion at the Patos Lagoon estuary – Brazil. Journal of Marine Systems, 68, 537-555

Martins, L., Reis, J.M., 2007. Nível Médio, Maré e Análise Harmónica. 5ªs Jornadas Portuguesas de Engenharia Costeira e Portuária, Lisboa, 11 e 12 de Outubro de 2007.

Martins, L., Serpa, M., Reis, J.M., 2004. Renovação de constantes harmónicas: Critérios e procedimentos utilizados no Instituto Hidrográfico. Anais do Instituto Hidrográfico nº17, 59-66.

McInnes, K., Hubbert, G., Abbs, J., Oliver S., 2002. A numerical modelling study of coastal flooding. Meteorology and Atmospheric Physics 80, 217-232

Moreira, S. M., Moreira-Santos, M., Ribeiro, R., Guilhermino, L., 2004. The “Coral Bulker” fuel oil spill on the North Coast of Portugal: Spatial and temporal biomarker responses in *Mytilus galloprovincialis.* Ecotoxicology, 13, 619-630

Park, D., Inoue, M., Wiseman, W.J., Justic, D., Stone, G., 2004. High Resolution Integrated Hydrology-Hydrodynamic Model: Development and Application to Barataria Basin, Louisiana. Coastal Marine Institute. U.S. Department of the Interior, 73 pp.

Pawlowicz, R., B. Beardsley, and S. Lentz, 2002. "Classical Tidal Harmonic Analysis Including Error Estimates in MATLAB using T_TIDE". Computers and Geosciences 28, 929-937.

Pinho, J.L.S. and Vieira, J.M.P., 2007. Mathematical Modelling of Salt Water Intrusion in a Northern Portuguese Estuary. IAHS Publication, 310, 277-290

Pugh, D., 1987. Tides, Surges and Mean Sea Level: A Handbook for Engineers and Scientists. John Wiley & Sons, Chichester, 472 pp.

Ramos, S., Cowen, R. K., Ré, P., Bordalo, A. A., 2006. Temporal and spatial distributions of larval fish assemblages in the Lima estuary (Portugal). Estuarine, Coastal and Shelf Science, 66, 303-314

Simmons, H. B., 1955. Some effects of upland discharge on estuarine hydraulics. Proceedings of The American Society of Civil Engineers, 792.

Sousa, M.C., Dias, J.M., 2007. Hydrodynamic model calibration for a mesotidal lagoon: the case of Ria de Aveiro (Portugal). Journal of Coastal Research, SI 50 (Proceedings of the 9th International Coastal Symposium). Gold Coast, Australia, ISBN

Sousa, R., Dias, S., Antunes, J. C., 2005. Spatial subtidal macrobenthic distribution in relation to abiotic conditions in the Lima estuary, NW of Portugal. Hydrobiologia, 559, 135-148

Stewart, Robert H., 2005. Introduction to Physical Oceanography. Department of Oceanography, Texas A&M University. 356 pp.

STOWA/RIZA, 1999. Good Modelling Practice Handbook. STOWA report 99-05, Dutch Department of Public Works, Institute for Inland Water Management and Waste Treatment report 99.036, ISBN 90-5773-056-1, 87 pp.

Vaz, N., Dias, J.M., Leitão, P.C., Nolasco, R., 2007. Application of the Mohid-2D model to a mesotidal temperate coastal lagoon. Computers and Geosciences 33, 1204-1209.

Walstra, D.J.R., Van Rinj, L.C., Blogg, H., Van Ormondt, M., 2001. Evaluation of a hydrodynamic area model based on the Coast3D Data at Teignmouth 1999. Proceedings of coastal dynamics 2001 conference, Lund, D4.1-D4.4.

Warner, J.C., Geyer, W.R., Lerczak, J.A., 2005. Numerical Modelling of an estuary: A comprehensive skill assessment. Journal of Geophysical Research, 110, 1-13

Zimmermann, C., Matheja A., Stoschek O., 2000. Reduction of harbour sedimentation at a tidal river. 2nd International Conference on Port Development and Coastal Environment, 5, Varna, Bulgária